Karlsruhe Institute of Technology

Particle in Cell Simulations of the KATRIN Source Plasma

Zur Erlangung des akademischen Grades eines
DOKTORS DERS NATURWISSENSCHAFTEN (Dr. rer. nat.)

von der KIT-Fakultät für Physik des
Karlsruher Instituts für Technologie (KIT)
angenommene

DISSERTATION
von

M. Sc., Kellerer, Jonas

Tag der mündlichen Prüfung: 31.6.2012
1. Referent: Prof. Dr. G. Drexlin
2. Referent: Priv. Doz. Dr. F. Spanier

Eidesstattliche Versicherung gemäß §13 Absatz 2 Ziffer 3 der Promotionsordnung des Karlsruher Instituts für Technologie (KIT) für die KIT-Fakultät für Physik:

1. Bei der eingereichten Dissertation zu dem Thema
   Particle in Cell Simulations of the KATRIN Source Plasma
   handelt es sich um meine eigenständige erbrachte Leistung.
2. Ich habe nur die angegebenen Quellen und Hilfsmittel benutzt und mich keiner unzulässigen Hilfe Dritter bedient. Insbesondere habe ich wörtlich oder sinngemäß aus anderen Werken übernommene Inhalte als solche kenntlich gemacht.
3. Die Arbeit oder Teile davon habe ich bislang nicht an einer Hochschule des In- oder Auslands als Bestandteil einer Prüfungs- oder Qualifikationsleistung vorgelegt.
4. Die Richtigkeit der vorstehenden Erklärungen bestätige ich.
5. Die Bedeutung der eidesstattlichen Versicherung und die strafrechtlichen Folgen einer unrichtigen oder unvollständigen eidesstattlichen Versicherung sind mir bekannt.

Ich versichere an Eides statt, dass ich nach bestem Wissen die reine Wahrheit erklärt und nichts verschwiegen habe.

Karlsruhe, den 1.6.2021, _____

Jonas Kellerer

Contents

1. Introduction **1**

2. The KATRIN Experiment and its Source Plasma **3**
2.1. Neutrino Mass and Tritium Beta Decay 4
2.2. KATRIN Experiment - An Overview 6
2.2.1. Windowless Gaseous Tritium Source 6
2.2.2. Differential Pumping Section 8
2.2.3. Cryogenic Pumping Section 9
2.2.4. Pre- and Main-Spectrometer 9
2.2.5. Detector 11
2.2.6. Rear Section 12
2.3. Source Parameters 13
2.3.1. Neutral Gas Flow 13
2.3.1.1. Density Distribution 13
2.3.1.2. Temperature Profile 15
2.3.1.3. Velocity Distribution 17
2.3.2. Electric Background Fields 18
2.3.3. Magnetic Background Fields 23
2.4. Particle Interactions in the KATRIN Source 23
2.4.1. Energy dependence of the Cross Section 24
2.4.2. Electron-Interactions 25
2.4.3. Ion-Interactions 30
2.4.3.1. Interactions of H^+ Ions 30
2.4.3.2. Interactions of $H_2{}^+$ Ions 33
2.4.3.3. Interactions of $H_3{}^+$ Ions 34
2.4.3.4. Interactions of Higher Order Cluster Ions 36
2.5. Measurements on the Source Plasma 41
2.5.1. Krypton Line Measurements 41
2.5.2. Particle Current Measurements 42
2.5.3. Pro-KATRIN Measurements 43

3. Classification of the KATRIN Plasma **47**
3.1. Introduction to Plasmas 47
3.2. Characteristic Length Scales 48
3.2.1. Debye-Length 48
3.2.2. Landau Length 50
3.2.3. Mean Free Path 50
3.2.4. Gyro Radius and Classical Diffusion 52
3.2.5. Inertial Length 53
3.2.6. Summary 54
3.3. Characteristic Frequencies 56
3.3.1. Plasma Frequency 56

3.3.2. Gyro Frequency and Synchrotron radiation . . . 57
3.3.3. Collision Rate . . . 57
3.3.4. Summary . . . 58
3.4. KATRIN Plasma Models . . . 60
3.4.1. Drift-Diffusion Model . . . 61
3.4.2. Partly Collisional Vlasov Model - Scope of this Thesis . . . 62

4. Simulation of Particle Distributions with KARL **65**
4.1. Simulation Method . . . 65
4.1.1. Virtual Current Borders . . . 66
4.1.2. Density Fields . . . 66
4.1.3. Particle Movement . . . 67
4.1.4. Particle Interactions . . . 68
4.1.4.1. Elastic Scattering . . . 69
4.1.4.2. Electron Impact Ionization . . . 71
4.1.4.3. Electron Impact Excitation . . . 71
4.1.4.4. Recombination . . . 71
4.1.4.5. Ion Cluster Formation . . . 72
4.1.4.6. Ion Charge Transfer . . . 72
4.2. Electromagnetic Field-Free Simulation . . . 73
4.3. Conclusion . . . 74

5. Particle in Cell Simulations with ACRONYM **77**
5.1. The Particle in Cell Method . . . 77
5.1.1. Grids for Currents and Fields . . . 78
5.1.2. Macro Particles . . . 78
5.1.3. Particle Movement . . . 79
5.1.4. Current Deposition . . . 80
5.1.5. Maxwell Solver . . . 81
5.2. Boundary Conditions . . . 81
5.2.1. Perfect Electrical Conductor . . . 81
5.2.2. Periodic Boundary Condition . . . 81
5.2.3. Perfectly Matched Layer . . . 81
5.3. Background Fields and Currents . . . 81
5.4. Particle Injection . . . 82
5.4.1. Injection Methods . . . 82
5.4.1.1. Constant Density . . . 82
5.4.1.2. Constant Current . . . 82
5.4.1.3. Constant Decay Rate . . . 82
5.4.2. Injection at PML boundary . . . 82
5.5. Electrostatic Potential from Poisson Equation . . . 83
5.5.1. Finite Differences Method . . . 83
5.6. Validation of ACRONYM Simulations . . . 84
5.6.1. Ion Current Approximation . . . 84
5.6.2. Background Electric Field . . . 85
5.6.3. Cavity Mode Excitation . . . 86
5.6.4. Debye-Sheath Development . . . 90
5.7. Conclusion . . . 93

6. Particle in Cell Simulation of KATRIN Source **95**
6.1. Rearwall Section . . . 95
6.1.1. Thermal electron distribution . . . 96

6.1.2. Thermal and Beta electron distribution 98
6.1.3. KATRIN Spectrum 102
6.2. Central Section 103
6.3. Complete Source Section 106
6.4. Conclusion 113

Appendix **115**
A. First Appendix Section 115

Bibliography **117**

Chapter 1
Introduction

Chapter 2
The KATRIN Experiment and its Source Plasma

The existence of neutrino oscillations has shown that neutrinos have a mass eigenstate with non zero mass. The absolute mass of these eigenstates is still unknown. There are various different methods to determine the mass of the eigenstates. These methods include the precise measurement of the beta decay spectrum. A comparison of the methods will be presented in section 2.1 with a focus on the beta decay method. The latter is employed at the KATRIN experiment, aiming to determine the electron neutrino mass m_{ν_e} with a precision down to 0.2 eV [30].

At the experiment the mass is inferred from the shape of the beta decay spectrum of tritium. The contribution of the mass on the shape is most dominant in the endpoint region. Thus the KATRIN experiment is designed to provide a high energy resolution, as well as a high event rate in this region of interest. These conditions are met by using a high luminous tritium source and a high precision spectrometer, see section 2.2.

The construction of the KATRIN experiment started in 2004 and is fully operational since 2019. Since then many science and calibration runs were performed. In 2020 the KATRIN collaboration could set a first limit on the electron neutrino mass at 1.1 eV(90% confidence level) [5]. Currently this limit is the world best limit on the neutrino mass in a direct approach, using only one month of data acquisition. The precision of this limit was manly determined by statistical uncertainties. Future results will include more data reducing the statistical uncertainties. Systematic uncertainties will then be the determining factor of the precision of the experiment. Hence a good understanding of the systematic uncertainties is necessary.

One of the contributions to the systematic uncertainties are effects, where electrons gain or loose energy. One of these effects is caused by starting potential differences inside the beta electron source. At the KATRIN experiment a windowless gaseous tritium source is used to generate beta electrons. These beta electrons partly ionize the surrounding neutral gas in the source and thus creating a plasma. This plasma mediates then the starting potential of the beta electrons through its own potential.

The properties of the plasma are directly dependent on the source conditions like neutral gas density, temperature and background fields. Thus they are investigated in detail in section 2.3. Additionally the properties of particle interactions play a vital role in the description of the plasma. They are discussed in section 2.4.

The plasma potential can not be measured directly, partly because of the self shielding mechanism inside a plasma and partly because of the intricate experimental setup. The plasma can therefore only be experimentally studied indirectly through its influence on charged

particles leaving the source. The measurement techniques employed at the experiment are presented in section 2.5.

2.1. Neutrino Mass and Tritium Beta Decay

Neutrinos are charge neutral fermions. They are created by weak interaction in one of the three different leptonic eigenstates ν_e, ν_μ, and ν_τ. The experiments of the Sudbury Neutrino Observatory [2] and Super-Kamiokande [43] could show that the neutrino flavor changes during propagation. This effect is called neutrino oscillation. The oscillations indicate that neutrinos have additional three mass eigenstates with non zero mass-squared differences. Thus the experiments showed that neutrinos have non zero masses. The absolute mass scale is still undetermined.

Neutrino mass experiments can be classified into two conceptually different categories: indirect and direct approaches. In the indirect search the neutrino mass is inferred from a model, where the model itself is not fully proven. The indirect approaches include cosmological studies, supernova neutrino measurements and measurements of the neutrinoless double beta decay. In the direct search the neutrino mass is determined directly from well tested models. The direct approaches include the spectroscopy of electron capture products and the spectroscopy of beta decay electrons. The different methods are described in short in the following. Their results are summarized in table 2.1.

Table 2.1.: Methods of neutrino mass measurements. The approach describes the method employed to determine the neutrino mass, the observable describes the variable on which the limit is determined

Approach	Observable	Current limit (in eV/c^2)	
Cosmology	$m_{\cos} = \sum_i m_i$	< 0.12	[1]
Super Nova	$m_{\bar{\nu_e}}$	< 5.7	[40]
$0\nu\beta\beta$	$m_{\beta\beta} = \lvert\sum_i U_{ei}^2 m_i\rvert$	$< 0.06 \ldots 0.17$	[21]
β and EC	$m_\beta = \sqrt{\sum_i \lvert U_{ei}\rvert^2 m_i^2}$	< 1.1	[3]

Cosmological Studies

Cosmological studies infer the sum of all neutrino masses from its influence on the large scale structure formation in the universe. Neutrinos play a vital role in the description of small scale structures. They can carry away mass from gravitational centers and thus reducing the amount of small scale structures. The efficiency of this process is dependent on the mass of the neutrinos. Larger neutrino masses will reduce the formation of small scale structures more than smaller neutrino masses. Thus observations of the structure size can provide an insight on the neutrino mass. One of these measurements is performed by the observation of the temperature anisotropies in the cosmic microwave background. In 2018 the Planck collaboration derived that the sum of all neutrino masses must be lower than 0.12 eV [1].

Supernova Neutrinos

Large numbers of neutrinos with high energies are emitted in a core-collapse supernova within a short period of time. The time difference of the arrival of the neutrinos at the earth is dependent on the initial energy of the neutrinos, the emission time difference and the neutrino mass. The emission time difference can be constrained by a suitable collapse model. Thus the neutrino mass can be inferred from a measurement of the neutrino flux. In 1987 a supernova occurred in close enough proximity of earth that the neutrino flux was measurable with the detectors at that time. An reanalysis of the measurement data showed that the anti neutrino mass could be constrained to values below 5.7 eV [40].

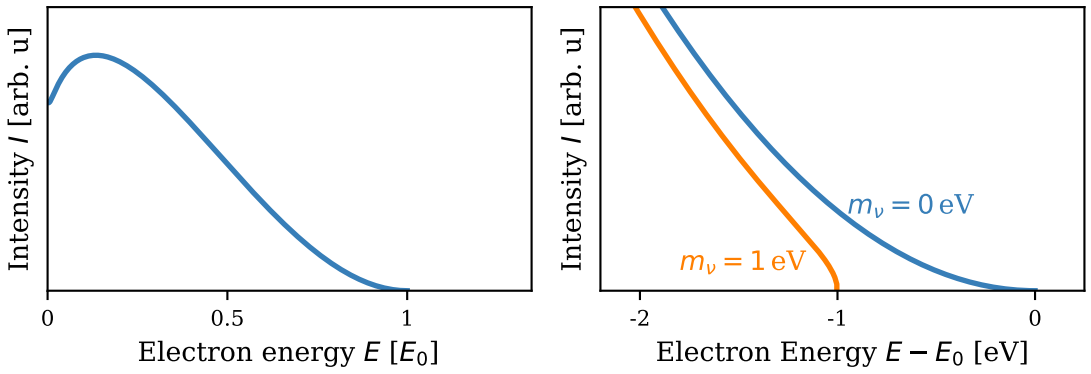

Figure 2.1.: Tritium beta decay spectrum. The left side shows the full spectrum up to the endpoint energy E_0. The right side shows a close up of the endpoint region for two different neutrion mass cases.

Neutrinoless Double Beta Decay

The neutrinoless double beta studies postulate that the neutrino is a Majorana particle and thus can act as its own antiparticle. Therefore some isotopes can undergo a double beta decay without emitting neutrinos. The measurement of the half life of such an interaction would provide a limit on the sum of Majorana masses. The current best limit on the sum of the Majorana masses is provided by the KamLAND-Zen collaboration with values below 0.06 eV [21].

Electron Capture and Beta Decay

Electron capture and beta decay experiments work on a similar principle. Both investigate the missing energy, which will be carried away by the neutrino, in either the electron capture process or the beta decay process. The calculations are based on energy and momentum conservation. No assumption is made on the specific nature of neutrinos. Thus these methods can be considered as model independent. In the following only the beta decay measurement principle will be described because both methods are so fundamentally similar. Please refer to [22] for more information on electron capture process.

The beta decay spectrum can be described by the well tested Fermi model of beta decay [16]. In the Fermi model the transition probability per time unit can be calculated by the use of Fermi's golden rule. From this the differential energy can be derived as

$$\begin{aligned}\frac{\mathrm{d}\Gamma}{\mathrm{d}E} =& \frac{G_\mathrm{F}^2 \cdot \cos\theta_\mathrm{C} \cdot |M|^2}{2\pi^3} \cdot F(Z+1,E) \cdot p \cdot (E+m_e) \\ & \cdot \sqrt{(E_0-E)^2 - m_{\bar{\nu}_e}^2} \cdot \Theta(E_0 - E - m_{\bar{\nu}_e}),\end{aligned} \tag{2.1}$$

with Fermi's coupling constant G_F, Cabibbo angle θ_C, the nuclear matrix element M, Fermi function $F(Z+1,E)$, kinetic energy, momentum and mass of the electron E, p, m_e, endpoint of the beta decay spectrum $E_0 = Q - m_e$ and the decay energy Q [45]. An exemplary depiction of this spectrum can be seen in figure 2.1. Following from 2.1 it can be deduced for small neutrino masses that the spectrum is influenced the most close to the endpoint E_0. This manifests in a distortion of the spectrum as well as a lower endpoint of the spectrum.

The distortion as well as the endpoint shift can be detected, given a high enough event rate in the endpoint region as well as a high enough energy resolution of the experiment. Thus the choice beta decaying isotopes relies on a low half-life and a low endpoint energy.

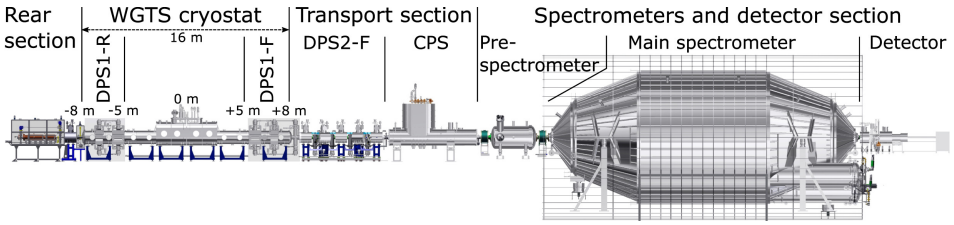

Figure 2.2.: KATRIN beam line and its components. Neutral tritium gas is injected in the WGTS and pumped out in the DPS and the CPS. The beta electrons are guided adiabatically by strong magnetic fields to the spectrometers, where they are sorted by their energy. The detector counts the incoming electrons. The rear section closes of the setup and is equiped with additional monitoring devices. Figure from [27]

The low half-life guarantees that there is enough statistics in the endpoint region with a comparably small amount of source material [45]. The low endpoint energy ensures that the influence on the spectrum is comparably large.

Tritium is an ideal candidate for neutrino mass measurements. It has a short half life of $T_{1/2} = 12.3\,\mathrm{yr}$ [41] and has a low endpoint energy of $E_0 = 18.6\,\mathrm{keV}$[45]. Additionally the beta decay of tritium is super-allowed. Hence the Matrix element M is energy independent. Because of these properties tritium is used in many beta decay experiments [35, 11] and most recently at the KATRIN experiment. The KATRIN collaboration could show that the neutrino mass is below 1.1 eV (90% confidence level)[4].

2.2. KATRIN Experiment - An Overview

The KArlsruhe TRItium Neutrino (KATRIN) Experiment aims to measure the electron antineutrino mass down to a precisions of 0.2 eV [30]. This will be an improvement of the results of Troizk and Mainz by a factor of 10[35, 11]. Currently the KATRIN experiment has set the world best limit of the neutrino mass in a direct approach of $m_{\bar{\nu_e}} = 1.1\,\mathrm{eV}$ (90% confidence level)[5] using only one month of measurement data. The experiment is still running to reduce the statistical uncertainty of this result.

The KATRIN experiment is 70 m long and can be divided into two parts: the Source and Transport Section (STS) and the Spectrometer and Detector Section (SDS), see figure 2.2. Neutral tritium gas is injected into the center of the Windowless Gaeous Tritium Source (WGTS) and is pumped out at both sides of the source. The Differential Pumping Section (DPS) and the Cryogenic Pumping Section (CPS) are connected to the source and reduce the tritium density to a bare minimum. Thus the amount of tritium entering the detector section is negligible. The electrons from the beta decay of tritium are are guided adiabatically by a strong magnetic field to the SDS. There both the Pre-Spectrometer (PS) and the Main Spectrometer (MS) filter the electrons according to their energy. The electrons are then counted by the detector providing an integral spectrum. All the different components will be discussed in the following.

2.2.1. Windowless Gaseous Tritium Source

The windowless gaseous tritium source provides beta electrons for the measurement with an activity of up to 10^{11} Bq at highly stable conditions [5]. The source consists of a 10 m long stainless steel tube that is connected at both sides to turbo-molecular pumps, see figure 2.3. Tritium gas is injected into the center of the tube through a specially designed injection chamber. The gas then streams to both sides, where it is removed by the turbo-molecular pumps. It is then processed, filtered and rejected in the center of the source. In this cycle approximately 40 g of tritium is used to maintain a constant flow of gas in the source. The

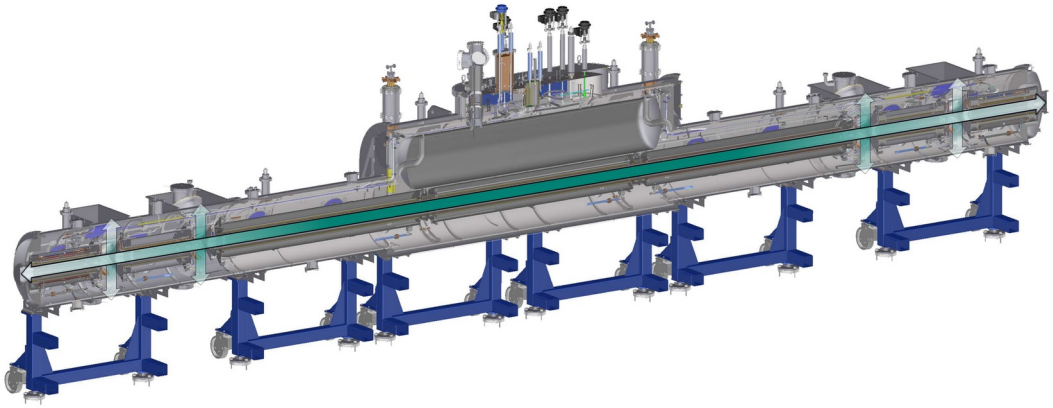

Figure 2.3.: Windowless Gaseous Tritium Source Tritium is injected in the center and diffuses to both sides and is pumped out by turbomolecular pumps. A density gradient is build up, depicted in turquoise. The surronding cryostat ensures stable temperatures and houses superconducting magnets. Figure adapted from [27]

actual amount of tritium inside the source can quantified by the column density. It is equal to the integral of the particle density along the source tube. At nominal source conditions the column density is $5 \times 10^{17}\,\mathrm{mol/cm^2}$ [5].

The WGTS beam tube is surrounded by a two-phase cryostat, ensuring a constant temperature inside the cavity. The temperature can be adjusted at low temperatures from 28 K to 37 K and at higher temperatures from 80 K to 115 K. Commissioning measurement show, that the temperature stays constant over a long period of time, exceeding the design value of 0.1 %/h. Also the temperature variation along the beam tube exceeds the design value of 0.1 % [5]. For more information of the temperature profile along the complete source see section 2.3.1.2.

The cryostat also houses superconducting magnets. These magnets provide the field necessary to guide the beta electrons to the source. They can provide a field of up to 3.6 T with a low drift $< 0.03\,\%$ per month [8] and fluctuations below 0.2 % per data acquisition run [5].

Injection Chamber

Tritium gas is injected in the center of the WGTS through a special designed injection chamber, see figure 2.4. The gas is streaming through 415 orifices, which are designed to "guarantee a shock-wave free injection without turbulence" [27]. A pressure-controlled buffer vessel ensures a constant injection pressure. Commissioning measurement showed that the pressure is stable at a level of 0.038 %. This value exceeds the design value of 0.1 % significantly [5].

The pressure of the vessel is adjusted corresponding to the target density in the source. The inlet pressure p_{in} directly corresponds to the density right in front of the inlet n_{c} and is calculated through the ideal gas law

$$n_{\mathrm{in}} = \frac{p_{\mathrm{in}}}{k_b T}\,, \tag{2.2}$$

where T denotes the temperature and k_b Boltzmann's constant. The inlet pressure can be adjusted to produce the needed density inside the source. The pressure for a column density of $5 \times 10^{17}\,\mathrm{mol/cm^2}$ at 30 K is calculated to be 0.337 Pa. This value changes for lower column densities or higher temperatures. If for example the desired column density is 75 % of the nominal value at a temperature of 80 K the pressure nedds to be changed to a value of 0.7 Pa. For more information on the density along the whole source tube see section 2.3.1.1.

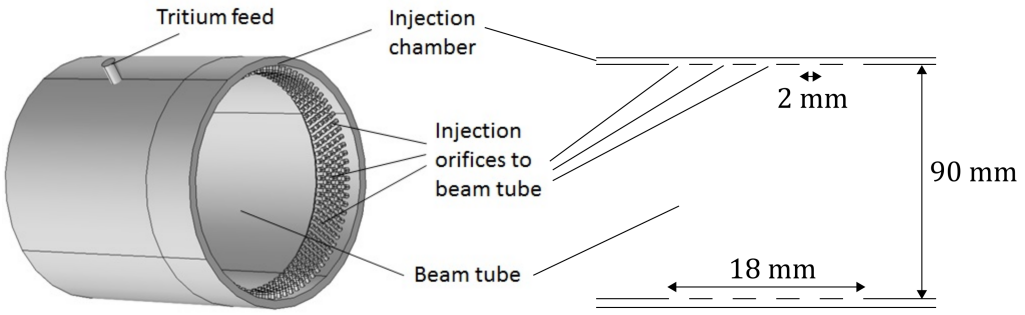

Figure 2.4.: Injection Chamber Tritium is fed through 415 orifices and streams to both sides of the WGTS. Figure from [27]

Source Plasma

Some of the beta electrons hit the surrounding neutral tritium gas and thus partly ionizing the gas. Hence more electrons and ions reside inside the WGTS than from beta decay alone. The total density of these charged particles is closely linked to the cross section of the interactions and the density of the neutral tritium gas. Calculations from Kuckert [37] show that the density is approximately $10^6/\mathrm{cm}^3$. This density is high enough that the charged particles can not be described as non interacting particles but as a plasma. The source plasma can have a direct influence on the neutrino mass measurement, because it can de- or accelerate electrons. This plasma is investigated in detail in the following chapters.

2.2.2. Differential Pumping Section

The differential pumping section connects the WGTS to the cryogenic pumping system, see figure 2.2. It acts as an additional pumping stage to reduce the neutral particle flux in the direction of the detectors. Commissioning measurements have shown that the tritium density is reduced in the DPS by a factor of $(9.6 \pm 1.0) \times 10^7$ at nominal column density [5]. This large reduction in tritium flow is achieved by the usage of five beam elements, attached to turbo-molecular pumps. These beam tube elements are arranged in a chicane to increase the number of wall collisions of molecules. Thus this special arrangement increases the pumping probability.

The beam tube elements are surrounded by superconducting magnets. So electrons are guided through the chicane without collisions with the tube walls. This magnetic field would in principle enable ions to traverse to the detector section. These ions would act as an additional background to the neutrino mass measurement. Thus additional dipole electrodes were installed at the beam tube elements. They are used in tandem with a single electrode at the end of the DPS to prevent the movement of ions to the detector section and remove the ions from the source.

The dipole electrodes provide an electric field which is perpendicular to the magnetic field. This configuration induces a $E \times B$ drift in the charged particle movement. The drift distance is dependent on the time spend in the cross field. Beta electrons spend only a short time in the DPS. Thus they leave the DPS almost unhindered. The ions in turn are much slower. Hence they are drifted to the beam tube walls, where they neutralize. The additional electrode at the end of the DPS is set on positive potential. Thus any surviving ions are reflected back to the WGTS, which increases the time spend in the cross field even further.

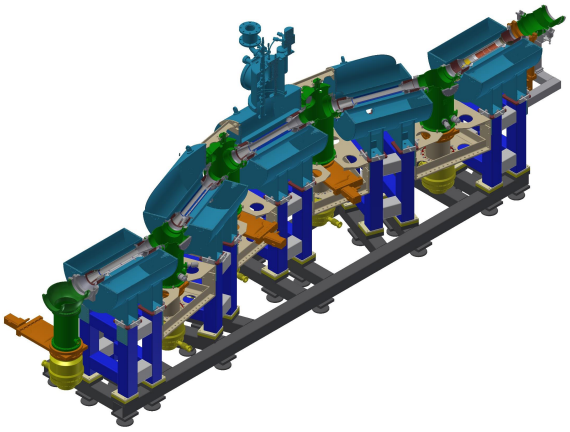

Figure 2.5.: Differential Pumping Section. Residual gas from the source is pumped out through turbomolecular pumps (yellow). The beam tube is bend in a chicane to maximize wall collisions of neutral gas. The beam tube is surrounded by superconducting magnets (light blue) to transport the beta electrons to the spectrometer section. Ions are removed by dipole electrodes. Figure adapted from [27]

2.2.3. Cryogenic Pumping Section

The cryogenic pumping section concludes the source and transport section and eliminates almost all tritium gas leaving the DPS. At this stage mechanical pumping becomes ineffective because of back-diffusion in the pumps. In the CPS the pumping is achieved by cryosorption. The tube walls are cooled down to 3 K. This low temperature builds a cold trap for the tritium gas. The sticking coefficient is increased by the usage of an argon frost coating on a gold plated surface. After 60 d the coating must be regenerated to eliminate the excess tritium. Similar to the DPS the CPS beam tube elements are arranged in a chicane to increase the probability that a tritium molecule hits the tube walls. Likewise superconducting magnets are used to guide the electrons through the setup. See figure 2.6 for a graphical representation of the CPS.

Commissioning measurements have shown that the tritium flow rate is reduced at least by a factor of 10^8. The sensitivity of this measurement was limited by the sensitivity of the residual gas analyzer. The true reduction factor can even be lower than this value [5]. In combination with the DPS the total reduction factor of the transport section is at least 10^{14}.

The CPS is houses two additional calibration systems, the forward beam monitor FBM and a condensed krypton source. Both can be inserted in the flux tube between the last two beam tube elements, see figure 2.6.The FBM can measure the relative electron flux originating from the source. Two independent motion systems can move the detector throughout the cross section of the flux tube. Thus the FBM can be used either for activity monitoring of the source, as well as monitoring of the magnetic flux tube. The condensed krypton source emits conversion electrons with a small line width. These electrons are then measured by the detector. The condensed krypton source can be used to calibrate the detector section. It can provide “precise values for the magnetic fields and electric potentials in the analyzing plane, which can be used to cross-check values obtained by simulation”[5].

2.2.4. Pre- and Main-Spectrometer

The pre- and main-spectrometer are used to filter the incoming electron flux corresponding to their energy. The spectrometers are used in tandem, where the pre-spectrometer filters

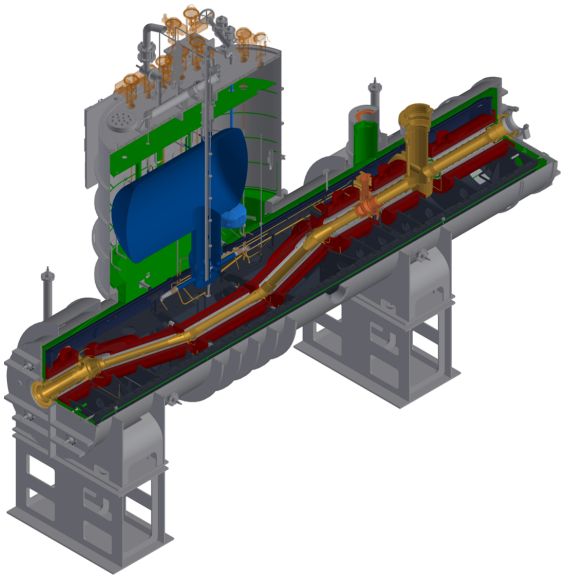

Figure 2.6.: Cryogenic Pumping Section. Residual gas from the DPS is cryosopred to the 3 K cold glod plated beam tube. Additional argon frost enlarges the sticking coefficient. The beam tube is bend in a chicane to maximize wall collisions of neutral gas. The beam tube is surrounded by superconducting magnets (dark red) to transport the beta electrons to the spectrometer section. Figure from [27].

out the main portion of low-energy electrons and the main spectrometer is used for the high precision filtering. Both spectrometers work with the same principle: magnetic adiabatic collimation with electrostatic retardation (MAC-E). A schematic representation of this principle shown in figure 2.7 and is discussed in the following.

The strong magnetic field of the KATRIN beam line guides electrons to the spectrometers. The movement of the electrons can be described by a circular motion around a guiding center, which traverses in longitudinal direction. The total kinetic energy is therefore shared by the kinetic energy of the guiding center $E_{\parallel}$ and by the kinetic energy of the gyro motion $E_{\perp}$. Beta electrons are emitted isotropically in the source. Thus the distribution of energy is divided evenly between the two kinetic energy contributions. The relation between the two kinetic energies can be changed by reducing the magnetic field adiabatically.

The magnetic moment μ is conserved in adiabatic changes of the magnetic field. The magnetic moment calculates to [3]

$$\mu = \frac{E_{\perp}}{B} = \text{const.}\,, \tag{2.3}$$

where B the magnetic field strength. Hence a reduction of the magnetic field strength reduces the energy of the cyclotron motion. The energy is transferred to the kinetic energy of the guiding center due to energy conservation this energy. So at the plane of lowest magnetic field strength the perpendicular kinetic energy is the lowest. By applying an electrostatic potential U_{max} at this plane position only electrons with a parallel kinetic energy greater than the retarding potential can pass. Hence this plane is also called analyzing plane.

The relation between maximal and minimal magnetic field strength B_{max},B_{min} defines the minimal energy ΔE which could not be converted into parallel direction

$$\frac{\Delta E}{E} = \frac{B_{\text{min}}}{B_{\text{max}}}\,. \tag{2.4}$$

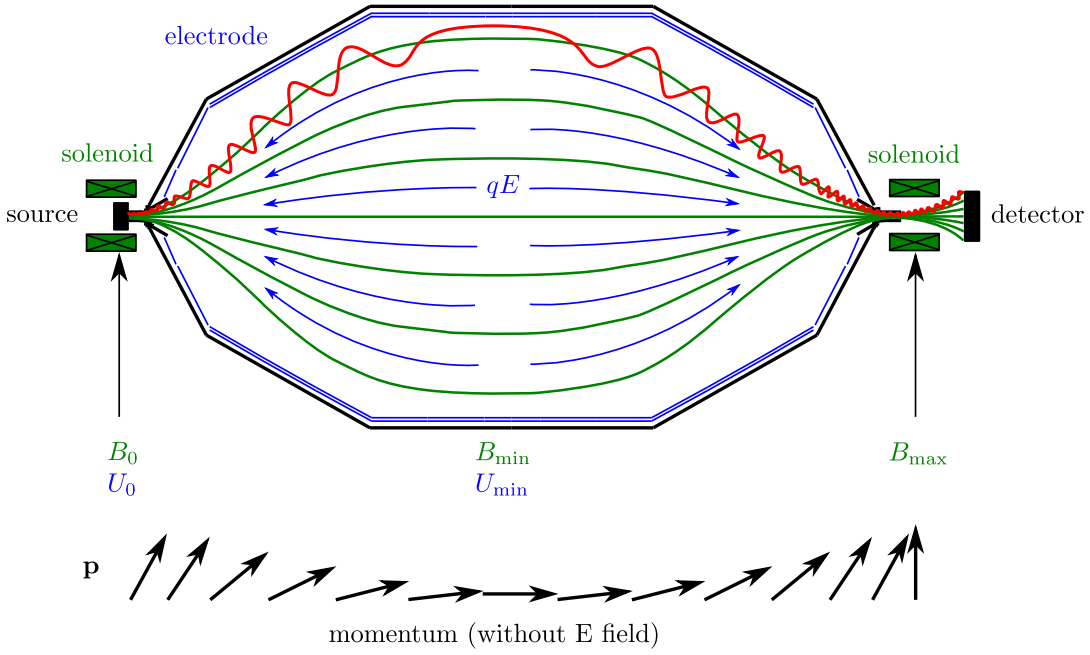

Figure 2.7.: MAC-E filter principle. Beta electrons gyrate around the magentic field lines, shown in red. The adiabatic reduction of the magnetic field strength converts the perpendicular kinetic energy to parallel kinetic energy. Thus the momentum vector is oriented in the direction of movement. The electrodes of the spectrometer produce an oposing electric field. Only electrons with an higher energy than qE can pass and are collected at the detector. Figure adapted from [58]

The design minimum magnetic field strength of the MS is $B_{\min} = 0.3\,\mathrm{mT}$ and the design maximal magnetic field strength is $B_{\max} = 6\,\mathrm{T}$. With a maximal electron energy of the beta decay $E_{max} = 18.6\,\mathrm{keV}$ the energy resolution of the KATRIN spectrometer calculates to $\Delta E = 0.93\,\mathrm{eV}$.

The reduction of the magnetic field strength also induces an expansion of the magnetic flux tube. To prevent electrons from hitting the walls of the experiment the flux Φ needs to be conserved. For an area A perpendicular to the magnetic field B it calculates to

$$\Phi = A \cdot B\,. \tag{2.5}$$

In the source section the design field strength has a value of $B_{\mathrm{S}} = 3.6\,\mathrm{T}$. The radius of the source tube is $R = 4.5\,\mathrm{cm}$. Combining this with the minimal magnetic field at the analyzing plane $B_{\min}$ results in a flux tube diameter in the MS of approximately 10 m.

2.2.5. Detector

The electron beam passing the analysis plane is collimated by a strong magnet at the end of the MS. The individual electrons are then detected by a 148 pixel silicon detector. The electrons are accelerated before detection by an additional electrode, which is kept at 10 keV. This procedure reduces backscattering effects and shifts "the signal peak into a region of lower intrinsic background" [3]. Overall the detector has an detection efficiency greater than $\epsilon_{\mathrm{det},i} \geq 90\%$ for each individual pixel i [7].

The count rate at the detector is measured for each retarding potential of the MS. This integral spectrum of the electron flux of the source is then used to determine the neutrino

mass. The count rate $\dot{N}_j$ for each pixel is calculated by

$$\dot{N}_j(U) = \frac{1}{2}\epsilon_{\mathrm{det},i} \cdot \sum_i \cdot \int_{eU}^{\infty} \left(\frac{\mathrm{d}\Gamma}{\mathrm{d}E}\right)(m_\nu^2, E_0) \cdot R_i(\mathbf{x}, E, U)\mathrm{d}E\,, \tag{2.6}$$

where U is the potential at the analyzing plane, R_i is the response function, E_0 is the endpoint energy of the tritium beta spectrum and m_ν is the neutrino mass. The response function evaluates all effects where electrons have gained or lost energy inside the KATRIN setup depending on their start position x and weights them with the probability of transmission at the spectrometers. The response function also includes additional corrections of the Doppler effect or start potential differences of the electrons. The neutrino mass is then determined by an evaluation of the difference between the measured rate and the simulated rate.

Naturally the sensitivity of the neutrino mass measurement is dependent on statistical and systematic uncertainties. The statistical uncertainties decrease as more beta electrons are detected. The systematic uncertainty stays constant over time and thus provides a natural limit to the sensitivity. Ultimately the KATRIN experiments aims to reach a sensitivity down to 0.2 meV at a 90 % confidence level [30].

2.2.6. Rear Section

The rear section RS is directly connected to the WGTS, see figure 2.2. It closes the beam line in the opposite direction of the detector. All beta electrons, which were reflected by the potential of the analyzing plane are terminated here at the so called rear wall. Additionally the rear section is equipped with various diagnostic systems. These systems include a high resolution angular-selective electron gun and a beta a beta-induced X-ray spectroscopy system (BIXS).

Rear Wall

The rear wall is a a gold-coated stainless-steel disk with a radius of 7.62 cm [37]. It is positioned at the end of the beam tube, see figure 2.8. It is surrounded by a superconducting magnet. This magnet ensures that the magnetic flux tube of the WGTS is mapped completely to the rear wall. So in general all charged particles leaving the WGTS in rear direction will hit the rear wall at some point. The induced current can be measured by an amperemeter.

The rear wall naturally exerts an contact potential due to workfunction differences between the rear wall and the surrounding stainless steel of the beam tube. The potential of the rear wall can be adjusted by an additional power supply. This potential is an important boundary condition for the source plasma. Thus the adjustment of the potential can be used to investigate the plasma.

The rear wall can be illuminated by a high luminous UV light [18]. The UV light produces photo electrons, which move into the source. These electrons can either be used for commissioning measurements of the empty source or they can be used as an additional source of negative charges in the source plasma, see 2.5.

Electron gun

The Electron Gun (egun) is situated behind the rear wall. It produces high energy electrons up to 30 keV with an intrinsic energy spread of approximately 0.2 eV [12]. These electrons are feed through a hole with a diameter of 5 mm inside the rear wall. The electron beam can be directed through magnetic and electric dipoles to cover the full beam tube cross section.

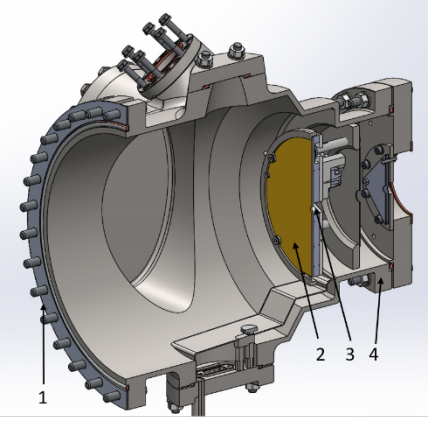

Figure 2.8.: Rear wall chamber. (1),(4) Mounting flanges, (2) rear wall, (3) central hole for egun beam transmission. Figure taken from [5]

"The e-gun allows studying electromagnetic characteristics along the main beam line and has been used in the commissioning of various beam line sections. It is also suited to investigate and monitor source characteristics, such as electron scattering and the column density stability" [5].

BIXS

The BIXS system is used to measure the activity of the source during neutrino mass measurement runs. It is located at one of the access pumps of the rear wall chamber. The BIXS system consists of a silicon drift detector, which measures the bremsstrahlung of beta electrons hitting the rear wall. The count rate directly corresponds to the activity of the source. Thus the BIXS system can also be used to monitor the column density. In commissioning measurements it was shown that the system allows for a "stability monitoring on the 0.1 % level in measurement cycles of duration 100 s" [5].

2.3. Source Parameters

The tritium source is an integral part of the KATRIN experiment. It provides a high luminous source of beta electrons at highly stable conditions. These conditions include the stability of the neutral particle flow, the gas temperature and the electromagnetic fields inside the source. Each of these parameters influence the development of the source plasma. Hence they will be discussed in detail in this section. First the neutral gas flow including density distribution, temperature distribution and velocity distribution will be discussed. Secondly the electric background fields will be analyzed. Thirdly the magnetic background fields will be described.

2.3.1. Neutral Gas Flow

The neutral tritium gas is both source of high energy electrons as well as interacting partner for both electrons and ions. The interaction probability is directly related to the density, temperature and velocity distribution of the neutral tritium gas. Hence a thorough investigation of these parameters along the length of the source is presented in the following.

2.3.1.1. Density Distribution

The density distribution inside the source is generated by the injection of neutral gas in the center and subsequent pumping of the gas at the pump ports. Thus the density distribution is shaped by the underlying geometry of the setup, the injection pressure and

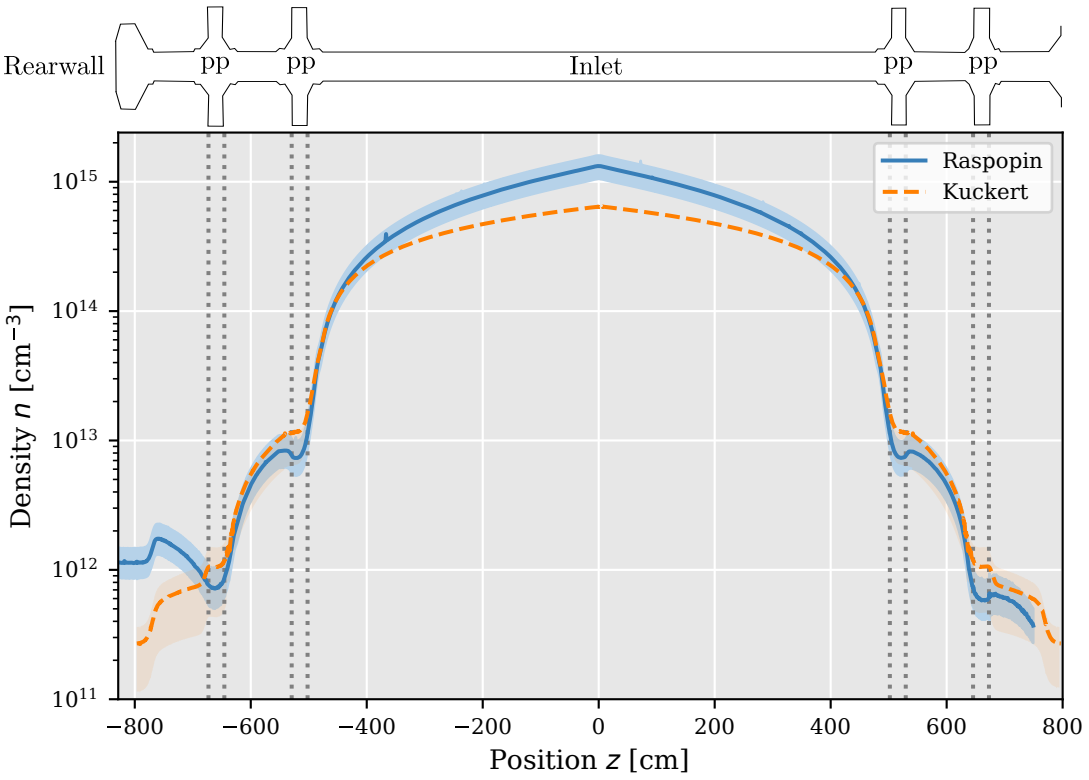

Figure 2.9.: Neutral gas density. Data from free molecular simulations by Raspopin [51] and scaled density from Kuckert *et al.* [38]. Data of Kuckert mirrored at inlet to negative positions. Errorband of Raspopin corresponds to different normalizations to the data of Kuckert.

the pumping probability. The description of the gas density depends on the mean free path of the gas particles, which is inversely proportional to the gas density. The mean free path ranges from approximately 1 mm in the center to values of 1 m. This means that the gas transitions from a viscous regime to a free-molecular regime. A corresponding model was developed by Kuckert *et al.* [36]. In this model the source was divided into three different sections. The first section included the central 10 m of the WGTS beam tube, where the gas can be described by a viscous flow. The second section included the first adjacent pump port, where a transitional flow model was used. The third section comprises the second pump port up to the beginning of the DPS, modeled as free-molecular flow. The densities of these sections were computed individually and boundary conditions were set up to join the results of each section.

The calculation of Kuckert *et al.* were performed at design conditions of the source ($T = 30\,\mathrm{K}$ and $p_{\mathrm{in}} = 0.337\,\mathrm{Pa}$). The current measurements of the KATRIN experiments are now performed at higher temperatures and lower injection density ($T = 80\,\mathrm{K}$ and $p_{\mathrm{in}} = 0.7\,\mathrm{Pa}$). It is assumed that the density profile does not change significantly and the density can be scaled accordingly to the inlet pressure. The resulting density distribution can be found in figure 2.9. It can be seen that the density drops significantly in the first 5 m from the injection to the first pump port. It is then further decreased when reaching the second pump port. The residual density is decreased by the pumping of the DPS.

The calculation of Kuckert *et al.* were only performed in direction of the detector. It can in general be assumed that the density is distributed similarly in the direction of the rear wall. The density is low in the region of the rear wall. It has almost no influence on the neutrino mass measurement directly. Thus this was not investigated further. In the context

of a description of the plasma the density of neutral particles plays a vital role. Thus a simulation was performed to determine the differences of the up- and downstream density in the Master Thesis by Raspopin [51].

For the simulation it was assumed that the results of Kuckert in the central region can be scaled by the ideal gas law. The adjacent section of the pump ports up to the rear wall was simulated using the software package MOLFLOW+ [31]. This package utilizes a Test-particle Monte Carlo method. The absolute density of the simulation is only dependent on the initial injection of particles. Thus the results of the simulation must be scaled accordingly. The scaling factor is chosen in such a way that the density of the density of the Monte Carlo simulation simulation is the same as the simulation of the central region. The results of Kuckert show an uncertainty. This uncertainty is therefore also present in the simulation results of Raspopin. A thorough description of the simulation and the scaling procedure is described in the works of Raspopin [51]. The resulting density profile is depicted in figure 2.9 alongside the scaled results of Kuckert.

It can be seen that:

- The simulation results of Raspopin do not agree with the simulation results of Kuckert in the central region. This is expected, because the free molecular model is not valid here. Thus Kuckert's results have to be used in this section. Nevertheless the simulation results of Raspopin can provide a rough estimate of the density in this region.
- The simulation results of Raspopin agree well with the results of Kuckert in direction of the detector close to the pump ports. Thus the model of Raspopin can be used here.
- There is a difference of the up- and downstream density. This difference is caused by the rear wall, which acts as a barrier for the gas. Pumps at the rear wall chamber prevent an increased accumulation of the gas.

2.3.1.2. Temperature Profile

The temperature profile of the tritium gas is directly correlated to the temperature profile of the beam tube. The WGTS temperature is controlled by a large high precision cryostat, see section 2.2.1. The cryostat is connected to the rear wall chamber, which is kept at room temperature. The resulting temperature distribution along the length of the source section for the current standard operation temperature can be found in figure 2.10.

The temperature of the beam tube and injection vessel determines the temperature of the neutral gas inside the tube. The gas is injected with the temperature of the beam tube. Each time a molecule hits the tube wall it will adopt the temperature at this point. In the central region the temperature of the walls is the same as the gas inside. At the rear wall chamber however the temperature rises from 80 K to room temperature. The density in this region is so low, see section 2.3.1.1, that a description of the gas with a Boltzmann-like distributed velocity distribution is no longer valid. Nevertheless this region is assigned a temperature as well.

The temperature of the gas is determined in the same Monte Carlo simulation as mentioned in 2.3.1.1. Single particles are tracked in the simulation and recorded at virtual facets inside the volume. The virtual facets were aligned in direction of the gas flow and perpendicular to it. The absolute velocity of the particles is collected in a histogram. A Maxwell-Boltzmann distribution fit is applied to the data. The Maxwell-Boltzmann distribution in this case reads as

$$f(v) = \left(\frac{2}{\pi}\right)^{1/2} \left(\frac{m}{k_b T}\right)^{3/2} v^2 \exp\left[-\frac{mv^2}{2k_b T}\right], \tag{2.7}$$

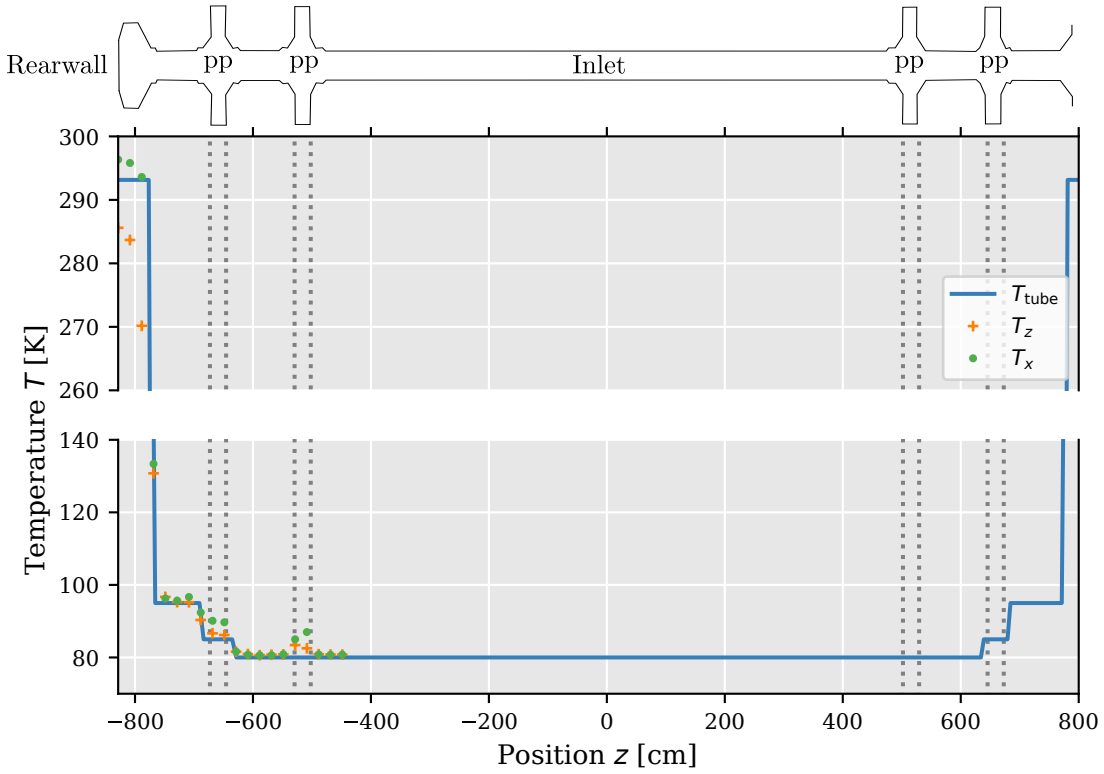

Figure 2.10.: Source tempererature. Temperatures of the beam tube from the experiment in comparison to simulated data from [51]. The temperature was derived from facets in z and x direction.

where m is the mass and v the absolute velocity of the molecule, k_b the Boltzmann constant and T the temperature. An additional drifting velocity was not considered here for simplicity. For more information on the drift velocity refer to the next section. The resulting simulated temperature distribution can be found in figure 2.10.

It can be seen that:

- The simulated temperature of the gas is similar to the temperature of the beam tube. As expected, the temperature is the closest in the region with high density.

- The simulated temperature diverges from the beam tube temperature at the pumping port positions. This can be explained by the temperature gradient in the pumping ports themself. Particles leaving the pump port will therefore show an increased temperature. The increase in temperature will not be distributed to the surrounding gas, due to the low scattering probability.

- The difference between the gas temperature and beam tube temperature is the highest at the rear wall chamber. The difference is dependent on the orientation of the facet. Facets directed in z direction show lower temperatures, while the facet in x direction show similar values to the beam tube temperature. This result hints to a beaming effect. Molecules upstream of the facet are therefore more likely to cross the z-facet as molecules from the rear chamber walls. In x direction there are no particles detected from the longitudinal direction. Thus only particles which have scattered in the rear wall chamber cross the facet. These molecules therefore have already adapted the temperature of the rear wall chamber.

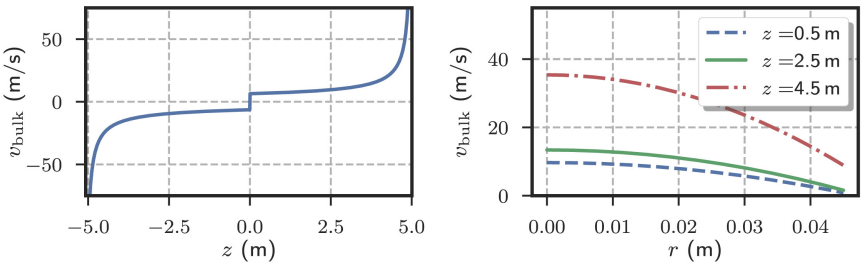

(a) Longitudinal velocity profile (1D) (b) Radial velocity profile (2D)

Figure 2.11.: Bulk velocity Simulated profile in the central beam tube element of the WGTS. Figure from [38]

2.3.1.3. Velocity Distribution

Electrons and ions can scatter off the neutral gas. These scatterings influence the movement of electrons and ions and thus the plasma. The velocity distribution of the neutral particle plays a vital role in the description of the scatterings. Thus a thorough investigation of the velocity distribution of the neutral particles is necessary.

The velocity distribution of the neutral particles is influenced by the inlet pressure and temperature, the pumping speed, and the temperature of the beam tube walls. Each contribution is weighted differently according to the density of the neutral particles. In the center for example there are many molecule-molecule interactions. Here the velocity distribution is dominated by the particle flow. In the rear wall chamber the density is reduced drastically, such that molecule-molecule interactions become negligible and collisions with the tube walls are dominant. This behavior can also described by the different flow regimes mentioned in section 2.3.1.1. In the center the gas is described by a viscous flow, while in the rear wall chamber the gas is described as free-molecular flow.

In the viscous flow regime the velocity distribution can be described by a Maxwell-Boltzmann distribution with an additional bulk velocity in longitudinal direction [37]. The Maxwell-Boltzmann distribution accounts for the large numbers of collisions of the neutral particles. The temperature of this distribution is given by the temperature of the beam tube walls. The bulk velocity describes the streaming process from the inlet in the center of the WGTS to both sides. The one dimensional distribution function of the longitudinal velocity v_z then reads as

$$f(v_z) = \left(\frac{m}{2\pi k_b T}\right)^{1/2} \exp\left(-\frac{m(v_z - v_b)^2}{2k_b T}\right), \tag{2.8}$$

where v_b denotes the bulk velocity. Simulations of Kuckert [38] show that the bulk velocity is dependent on the longitudinal as well as the radial position, see figure 2.11. The bulk velocity increases from inlet to both sides. Radially the bulk velocity is reduced at the tube walls, corresponding to wall interactions which slow down the gas movement.

At lower densities the velocity can no longer be described through a drifting Boltzmann distribution, because interparticle collisions are reduced. The velocity of each particle needs to be tracked individually to gain an insight in the velocity distribution. The velocity distribution of the gas in this region can be determined in the same Monte Carlo simulation as mentioned in 2.3.1.1. In the simulation virtual facets were set up to collect each particle that crosses the facet. In contrast to the analysis in section 2.3.1.2 the velocity contribution in each space direction was collected in a histogram. The probability that a particle will cross the virtual facet is dependent on the incident angle towards the facet. Thus the histograms were weighted accordingly. It was found by Raspopin that the velocity

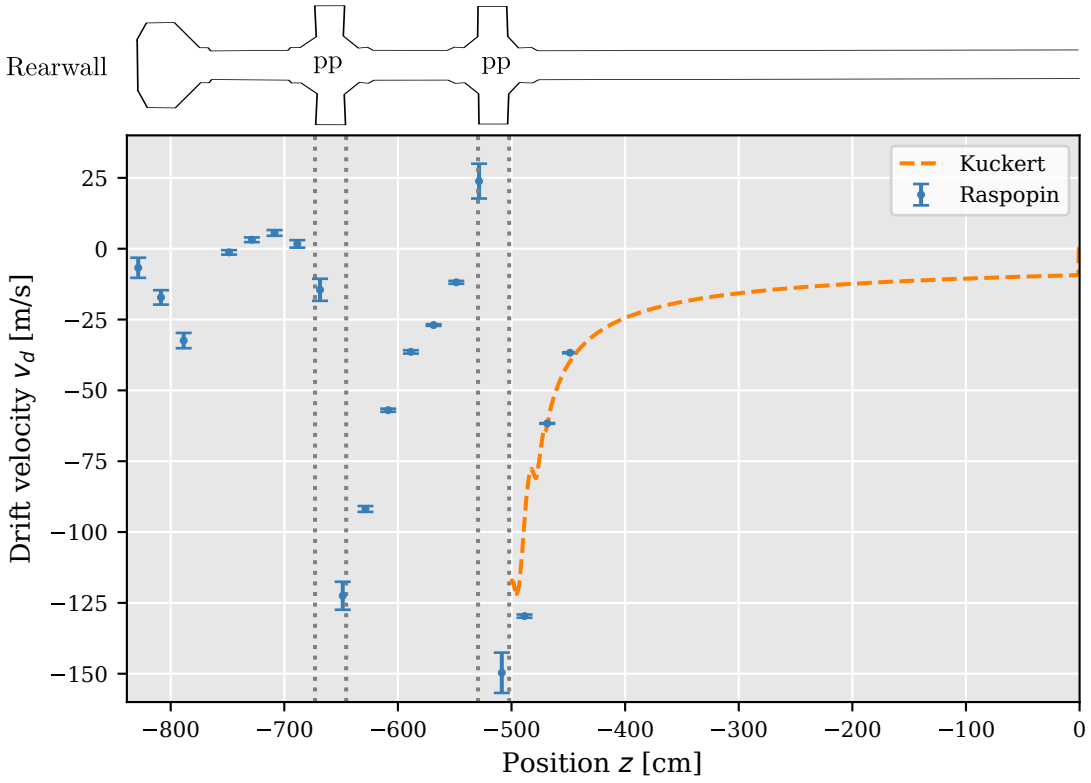

Figure 2.12.: Simulated bulk velocity in rear direction. Comparison of data from Raspopin [51] and Kuckert *et al.* [38]. Errorbar represent fit uncertainties only.

distribution is similar to a gaussian distribution. In z direction the gaussian distribution was shifted to lower values. Thus he tried to describe the velocity distribution in z direction through equation 2.8. The corresponding drift velocities can be found in figure 2.12 in comparison to the drift velocites of Kuckert.

It can be seen that:

- The bulk velocity of the simulation of Raspopin is in good agreement with the bulk velocity of Kuckert before the first pump port. It can be therefore assumed that the analysis procedure of Raspopin works correctly.
- The bulk velocity in the pump ports shows a huge spread. This can mainly be attributed to the shape difference from the Maxwell-Boltzmann distribution [51]. This means that the drifting gas model can not be used here. In the context of this thesis it is therefore assumed that the bulk velocity is zero at the pump ports.
- The bulk velocity is predominantly negative. Thus the gas streams continously in the direction of the rear wall, where additional pumps remove tritium molecules.
- The bulk velocity is has positive values in the beam tube element which is connected to the rear wall chamber. The bulk velocity values are so small, that their difference from zero can be attributed to shape differences to the Maxwell-Boltzmann distribution [51].

2.3.2. Electric Background Fields

The movement of charged particles is dominated by electric and magnetic fields through the Coulomb force. In general there is a self shielding mechanism of the plasma against

external fields, see section 3.2.1 and 3.2.5. Nevertheless the extrenal fields can penetrate the plasma up to a certain point. Therefore these fields need to be taken into account. Some of electric background fields are induced directly by a connection of a power supply to an electrode. Others are generated by workfunction differences, called contact potential.

Contact potential differences can occur when two metals are brought into electrical contact with each other. The potential difference is reliant on the workfunction differences of both metals. The workfunction meanwhile is inherit to each metal and to the surface conditions like granularity or contamination [57].

Thus there can exist a workfunction difference between rear wall and beam tube because they are manufactured from different metals, gold and stainless steel. Additionally the surface contamination can be different for both beam tube elements. Furthermore the surface contamination can be position dependent because the exposure to tritium gas is non homogeneous. The workfunction differences are currently investigated but no conclusive result was published yet. In the context of this thesis it is assumed that the position dependence of the workfunction can be neglected. Thus the total contact potential difference can be modeled by an additional power supply connected to the rear wall.

All KATRIN beam tube elements are electrically connected. Thus they all have the same surface potential, excluding surface potential differences. Only special electrodes like the rear wall and the dipole electrodes in the DPS are connected to a power supply. The induced potential U_e is measured in relation to the potential of the beam tube. The total potential exerted by the electrodes U_total can now be written as

$$U_\mathrm{total} = U_e + \Delta U_\mathrm{wf}\,, \tag{2.9}$$

where ΔU_wf is the workfunction difference between the electrode and the beam tube. Thus the potential of the electrodes can be treated as an effective potential.

Measurements

Measurements of the background fields are challenging because of the intricate and closed design of the beam line. The fields are moderated by the plasma. Thus they can not be measured while there is a plasma inside the source. In general the fields can be studied by their effect on charged particles, either by a change in the particle trajectory or by a change in the kinetic energy of the particle. For the studies electrons will be created at some point inside the source and their energy and position will be recorded at the KATRIN main detector, at the FBM or the rear wall. A comparison with the expected electron flux and energy distribution provides an insight into the electric fields in the source. The energy at which a particle will be detected depends on the initial kinetic energy and the electric field which will be traversed during flight. The value of the electric field can only be deduced if there exists a time dependent or position dependent electric field.

Time dependent electric fields accelerate the passing electrons if the time spend in the field is in the same order as the period of the oscillation. In a measurement the field then broadens an initial monoenergetic line. The broadening is then a measure for the field strength. This technique is used by egun measurements. The egun produces electrons with a small intrinsic energy spread outside of the source. The electrons then traverse the source and are collected by the detector. Results by Friedel [17] indicate the contribution of time dependent fields are negligible in an empty source. Further results, including a time of flight measurements will be published in the future [5].

Position dependent electric fields are visible at the detector if the starting potential of two separate electrons are different. Thus an initial monoenergetic energy distribution will be broadened by the field. The electrons of these measurements must originate from the source

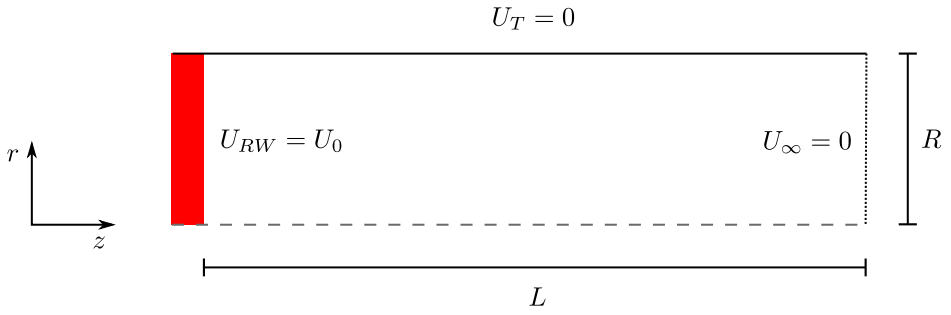

Figure 2.13.: Simplified geometry of the KATRIN source Used for the analytical calculation of the electric field in front of the rear wall

volume itself. At the KATRIN experiment the position dependent fields are investigated through a gaseous 83 mKr source, see section 2.5.1. Currently there is no conclusive result available on the broadening of the conversion line width, which is directly attributed to spatial inhomogenities of the potential in the empty source.

Numerical Simulation

The potential distribution in the source can in general be calculated by the given geometry and the potential of each surface. The field distribution in the KATRIN setup is calculated numerically using the subpackage kemfield of the software package kassiopeia [19]. In kemfield the electric field is calculated using the boundary element method. The simulation yields a field map for a given geometry and surface potential input. The simulation needs to be rerun each time a parameter changes. The field maps of the simulation can then be used in the analysis for the neutrino mass measurements.

Analytical Calculation

The proposed plasma simulation method of this thesis uses a simplified geometry of the KATRIN source, see figure 2.13. Here the source tube is approximated as an cylinder with an open and a closed end. In this special case an analytic expression can be found for the potential distribution in front of the rear wall. The analytical calculation provides a faster access to the electric background field for the plasma simulation than the numerical simulations do. Thus the analytical calculation will be presented here. The procedure is adapted from [47]

The potential in the tube $U(r, \theta, z)$ can then be calculated by solving Poisson's equation

$$\Delta U(r, \theta, z) = 0\,, \tag{2.10}$$

with the following boundary conditions: the rear wall is biased by the potential U_0, the beam tube is kept at ground potential $U_T = 0$ and the potential far away U_∞ is not influenced by the rear wall, so it is set to zero.

A solution can be obtained by the use of the separation ansatz $U(r, z) = P(r)\,Q(\theta)\,Z(z)$. Thus equation 2.10 can be written as

$$PQZ\left(\frac{1}{P}(P'' + \frac{1}{r}P') + \frac{1}{r^2}\frac{Q''}{Q} + \frac{Z''}{Z}\right) = 0\,, \tag{2.11}$$

using the notation that the primed variables are first derivatives of the variable to their arguments. Given the cylindrical geometry the z and θ component can be expressed by

choosing

$$\frac{Z''}{Z} = k^2 \tag{2.12}$$

$$-\frac{Q''}{Q} = n^2\,, \tag{2.13}$$

with n being integer and k real values. So Z and Q can be written as

$$Z(z) = \exp(kz) \tag{2.14}$$

$$Q(\theta) = \exp(\imath n z)\,. \tag{2.15}$$

Using these two solutions with the definition of $x := kr$ equation 2.11 can be transformed to Bessel's differential equation

$$\frac{\partial^2 P(x)}{\partial x^2} + \frac{1}{x}\frac{\partial P(x)}{\partial x} + \left(1 - \frac{n^2}{x^2}\right) P(x) = 0\,, \tag{2.16}$$

which is solved by Bessel functions of the first kind J_n. Thus a general solution of the Poisson equation is found. The specific solutions is calculated using the boundary conditions from above. They can be written in this context as

$$U(r, \theta, z = L) = 0 \tag{2.17}$$

$$U(r = R, \theta, z) = 0 \tag{2.18}$$

$$U(r, \theta, z = 0) = U_0 \cdot \Theta(R - r) \tag{2.19}$$

where L and R are the length and radius of the cylinder and Θ the Heaviside function. From equation 2.17 it follows that

$$Z(z) = \sinh k(L - z)\,. \tag{2.20}$$

From equation 2.18 it follows that

$$k = \frac{a_{nm}}{R} \tag{2.21}$$

with $J_n(a_{nm}) = 0$. The solution of Poisson's equation can now be written as

$$U(r, \theta, z) = \sum_{n=0}^{\infty}\sum_{m=1}^{\infty} J_n(kr) \sinh k(L - z) \left(c_{nm} \sin n\theta + d_{nm} \cos n\theta\right)\,. \tag{2.22}$$

From equation 2.19 it follows that the potential is not dependent on the angle θ. Thus all coefficients $c_{nm} = 0$ and only $d_{0m} \neq 0$. The coefficient d_{0m} will be determined using the orthogonality of the Bessel function and the boundary condition of 2.19 from the following equation

$$\int_0^R J_0\left(k_{0m}\frac{r}{R}\right) \cdot U(r, \theta, z = 0) \cdot r\mathrm{d}r = \int_0^R J_0\left(k_{0m}\frac{r}{R}\right) \cdot U_0 \cdot \Theta(R - r) \cdot r\mathrm{d}r\,. \tag{2.23}$$

It follows that

$$d_{0m} = \frac{2U_0}{k_{0m} J_1(k_{0m}) \sinh k_{0m}\frac{L}{R}}\,. \tag{2.24}$$

So the specific solution of the Poisson's equation can be written as

$$U(r, \theta, z) = 2U_0 \sum_{m=1}^{\infty} \frac{\sinh\left(k_{0m}\frac{L-z}{R}\right)}{\sinh\left(k_{0m}\frac{L}{R}\right)} \frac{J_0(k_{0m}\frac{r}{R})}{k_{0m} J_1(k_{0m})} \tag{2.25}$$

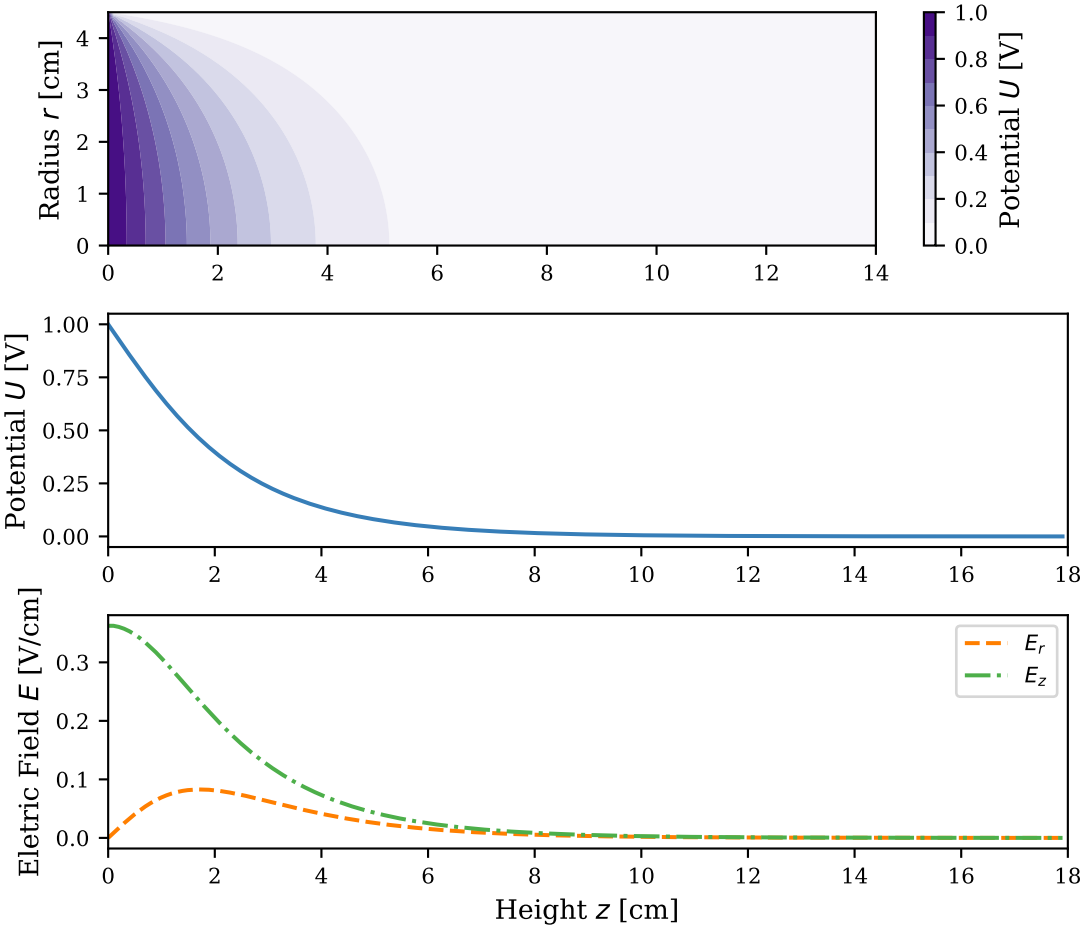

Figure 2.14.: Analytical electric background field of the rear wall chamber Computed using a rear wall potential of 1 V. The potential drops significantly on the first few centimeters and is close to zero only 20 cm away from the rear wall.

and static electric field can be directly calculated using

$$\mathbf{E} = -\nabla U \,. \tag{2.26}$$

This result is analytically correct but for a numerical calculation some adaptations need to be made

- The index m will be bound to a large number. This number is chosen in such a way that the oscillations of the Bessel function are more frequent than the radial position difference of each data point.
- If the fraction of L and R is too high the value of sinh is greater than the largest number on the computing system. Hence L is bound such that the potential value at L is numerically indistinguishable from zero.

An exemplary potential and field distribution in radial and longitudinal direction can be found in figure 2.14. It can be seen that the potential drops significantly on the first few centimeter and is close to zero at 15 cm away from the source. So the effect on single charged particles is only relevant in the rear wall chamber. In the center of the source the potential is dominated by the beam tube, so close to zero. This behavior will change significantly when there is a plasma inside the source. This claim is supported by measurement, shown in section 2.5.

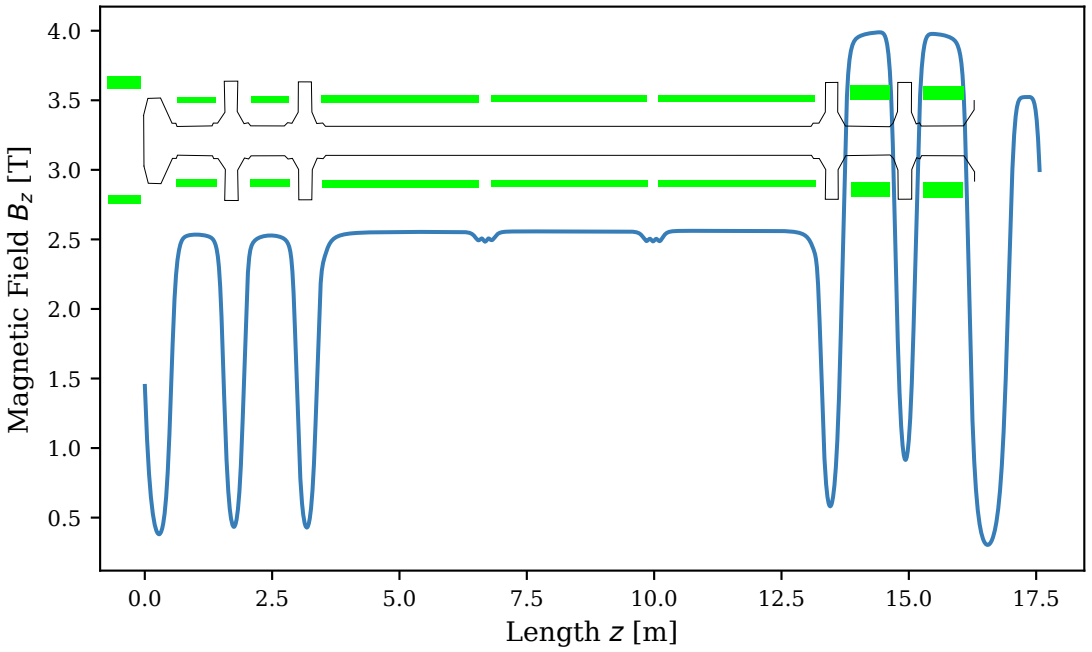

Figure 2.15.: Magnetic background field The magnetic field strength was computed using the software package kassiopeia. The green bars show the position of the super conducting magnets in relation to the beam tube (black).

2.3.3. Magnetic Background Fields

The magnetic field inside the source is generated by a multitude of super conducting magnets. These magnets surround each tube element of the source, see figure 2.15. These magnets provide a strong field up to 3.6 T with a low drift $< 0.03\,\%$ per month [9] and fluctuations below $0.2\,\%$ per data acquisition run [5]. At this high magnetic fields there exists the risk of quenching. This was investigated during commission measurements with the complete KATRIN beam line. There it was shown that a reduction down to $70\,\%$ of the design magnetic field eliminates the risk of quenching. Thus the magnetic field strength is reduced to 2.5 T [9]. The magnetic field strength is simulated with the software package kassiopeia [20]. The magnetic field value at each position in the source can be evaluated by tracking a test particle in the source with a given set of driving currents of the magnets. An exemplary field map can be found in figure 2.15.

2.4. Particle Interactions in the KATRIN Source

There exist many different types of particles in the KATRIN source: neutral particles, electrons, ions and ion clusters. Each of the particle species can interact with each other. The interplay of the collisions is the building block of the plasma. Thus a thorough investigation of the particle interactions will be presented in the following. First a short summary of cross sections and their energy dependence will be given, second all interactions of electrons will be discussed and third a summary of ion interaction will be provided.

The collision probability can be described with the cross section of the interaction and the density of each particle specie. The density of neutral particles is much higher in comparison to the density of charged particles. Thus it is not influenced by interactions with charged particles. Therefore it will not be discussed here. See section 2.3.1 for more information on the neutral density.

2.4.1. Energy dependence of the Cross Section

The interaction probability $\mathcal{P}$ of a particle flying through a cloud of other particles can be written as

$$\mathcal{P} = n\sigma \mathrm{d}x \,, \tag{2.27}$$

where n is the density of the particle cloud, $\mathrm{d}x$ the distance that is traversed and σ the cross section of the interaction. The cross section can be dependent on the energy of the interaction. In the literature there is no agreement if the cross section is given dependent on the kinetic energy or the total energy of the system. In atomic physics most of the time the kinetic energy will be given, while in high energy physics the total energy will be provided. In this thesis the notation of the kinetic energy will be used. Furthermore it is not agreed upon in which inertial frame of reference the cross section has to be provided. It can either be given in the target frame, where the cloud particles are at rest, or in the center of mass frame. A conversion of the energies in the different inertial frames will be derived in the following.

Consider two particles p_1 and p_2 in the laboratory frame with the masses m_1 and m_2 and the kinetic energy E_1 and E_2. The total energy E_{total} for each particle is calculated by

$$E_{\mathrm{total},i}^2 = m_i^2 c^4 + E_i^2 \,, \tag{2.28}$$

where i is the particle index and c the speed of light. The four energy vector of one particle can than be written as

$$p_i^\mu = \left(\frac{E_{\mathrm{total},i}}{c}, \mathbf{p}_i \right) \,, \tag{2.29}$$

where $\mathbf{p}_i$ is the momentum of the particle i. Thus the invariant mass s of the total system is calculated by

$$s = (E_{\mathrm{total},1} + E_{\mathrm{total}2})^2 - (\mathbf{p}_1 + \mathbf{p}_2)^2 \cdot c^2 \,. \tag{2.30}$$

The kinetic energy of the center of mass frame E_{cm} then calculates to

$$E_{\mathrm{cm}} = \sqrt{s} - m_1 c^2 - m_2 c^2 \,. \tag{2.31}$$

In the target frame we define that the second particle is at rest so the momentum is zero. In this case the invariant mass reads as

$$s = m_1^2 c^4 + m_2^2 c^4 + 2 m_2 c^2 E_a \,, \tag{2.32}$$

where E_a is the total energy of the first particle in the target frame. The kinetic energy $E_{\mathrm{kin},a}$ of the first particle in the rest frame of the second particles then calculates to

$$E_{\mathrm{kin},a} = \frac{s - m_1^2 c^4 - m_2^2 c^4}{2 m_2 c^2} - m_1 c^2 \,. \tag{2.33}$$

In the case that $m_1 \ll m_2$ it can be derived that

$$E_{\mathrm{kin},a} \approx E_{\mathrm{cm}} \,. \tag{2.34}$$

Equations 2.33, 2.30 and 2.31 can now be used to convert the different energies.

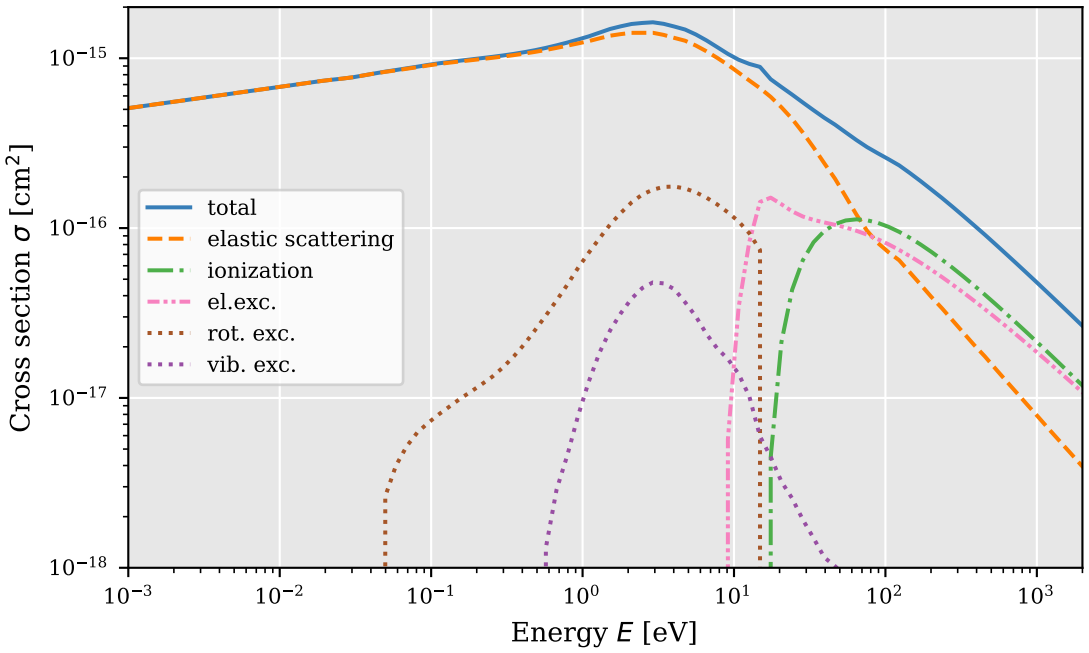

Figure 2.16.: Selection of Electron-H_2 cross sections The energy describes the kinetic energy of the electron, when the interaction partner is at rest. Rotational, vibrational and eletric excitation cross sections are given as the sum of the cross section over all excitation states. Data taken from [29, 55].

2.4.2. Electron-Interactions

Electrons of the source can interact with neutral particles, ions, ion clusters and other electrons. As mentioned before the interaction probability is dependent on the cross section of the interaction and the target density. The density of neutral particles is much higher than the density of ions and electrons. Hence this section will focus on electron interactions with neutral gas. Nevertheless the recombination with ions and dissociation of ion clusters influences the density of electrons and ions. Hence they will be discussed here as well. Electron-electron interactions will not be discussed here because of the infinite interaction range. The interaction range is reduced in a plasma. Please refer to section 3.2.3 for more information.

There is allmost no data available on interactions of electrons with tritium but with hydrogen or deuterium. In most interactions the electron only interacts with the shell electrons of tritium. Thus the mass of the core is not as relevant as its charge. Hence isotopic effect should be small on the cross section. In the context of this thesis the mass difference is only taken into account at the recoil after the interaction.

All cross sections in this section are given depending on the kinetic energy of the electron in the rest frame of the interaction partner of the electron. The energy range is adapted to enclose the highest energies of the beta decay electrons $E_{\mathrm{max}} \approx 10^4\,\mathrm{eV}$ as well as the lowest energies of thermal electrons $E_{\mathrm{min}} \approx 1\,\mathrm{meV}$.

Elastic Scattering

The elastic cross section was measured at different experiments in the energy range of $2 \times 10^{-2}\,\mathrm{eV}$ to $1 \times 10^{2}\,\mathrm{eV}$. The results of these experiments were combined by Tawara *et al.* [56] and parameterized by Yoon *et al.* [59]. Lower energies than 2×10^{-2} were not measured, but are relevant for electron interactions at the KATRIN experiment. Thus cross section

values below $2 \times 10^{-2}\,\mathrm{eV}$ were generated by a linear extrapolation of the experimental data in the range of $2 \times 10^{-2}\,\mathrm{eV}$ to $1 \times 10^{-1}\,\mathrm{eV}$. Cross sections above $1 \times 10^{2}\,\mathrm{eV}$ were derived from a simulation with the software package ELSEPA [53]. There the cross section is determined using a Dirac partial-wave calculation. The resulting elastic scattering cross section is depicted in figure 2.16.

It can be seen that elastic scattering of electrons and neutral gas is the dominant interaction channel at low energies ($< 100\,\mathrm{eV}$). Thus low energy electrons will adopt the velocity distribution of the neutral gas, given they only act as independent particles and the density of the neutrals is high enough. The excistance of a plasma might change this behavior. See section 3.2 for more information.

The elastic cross section drops for higher energies and other interactions become more dominant. Nevertheless the total cross sections drops eneugh that the mean free path of the interactions is comparable to the scale of the beam tube, secc section 3.2.3. Thus high energy electrons will scatter only scarcely.

Ionization through Electron Impact

The energy of beta electrons is much greater than the minimal ionization energy of hydrogen molecules ($E_{\mathrm{th}} = 15.42\,\mathrm{eV}$) [29]. Thus ionization of the neutral particles can occur. There exist different ionization channels. The dominant process is the non dissociative ionization, which can be written as

$$\mathrm{e}^- + \mathrm{T}_2 \rightarrow \mathrm{e}^- + {\mathrm{T}_2}^+ + \mathrm{e}^- \,. \tag{2.35}$$

Other ionization processes lead to a dissociation of the molecule producing atomic hydrogen and atomic hydrogen ions. These processes depend on the initial state of the hydrogen molecule. The energy threshold of these processes is higher ($E_{\mathrm{th}} > 18.15\,\mathrm{eV}$) [29] due to the molecular binding energy. The total cross section of both ionization types is depicted in figure 2.16.

It can be seen that ionization is the dominant process at energies greater than $1 \times 10^{2}\,\mathrm{eV}$. Thus beta electrons will loose their energy mainly through this channel. The lost energy E is dependent on the binding energy B and the momentum transfer W to the shell electron. After ionization both electrons are indistinguishable. Thus the maximal lost energy E_{max} is given by

$$E_{\mathrm{max}} = \frac{E_\beta - B}{2} \,. \tag{2.36}$$

The exact energy spectrum of the secondary electrons can be calculated through the works of Rudd [15] and Kim [33]. They show that the small energy losses are more probable than high energy losses. High energy losses are relevant for the description of the electron energy distribution in the source. Small energy losses are relevant for the neutrino mass measurement, as they effect the shape of the beta spectrum. Thus the energy loss at beta electron energies was measured and parameterized [10].

Electronic Excitation

Free electrons of the source can excite shell electrons of the molecules

$$\mathrm{e}^- + \mathrm{T}_2(n_1) \rightarrow \mathrm{e}^- + \mathrm{T}_2(n_2) \,, \tag{2.37}$$

where n_1 and n_2 denote the excitation state of the molecule. The transferred energy must equal to the difference of the energy levels. For hydrogen molecules this difference is of the order of $10\,\mathrm{eV}$ [29]. The cross section of the electronic excitation is dependent on the

initial electronic state of the molecule. The source of the KATRIN experiment is kept at low temperatures. Therefore it is assumed in the context of this thesis that the molecules exist in ground state. In this case there exist three main excitation channels, excitation to dipole allowed singlet state, excitation to dipole forbidden singlet states and excitation to triplet states [29]. The resulting state of the excitation is of no interest for the KATRIN experiment. Thus here only the sum of the cross sections is shown, see figure 2.16.

It can be seen that electronic excitation is relevant for electrons with an energy greater than 10 eV. The cross section is comparable to the cross section of ionization. But neveretheless the energy lost per interaction is limited by the maximal excitation energy. Thus it can be assumed that electronic excitation plays a secondary role in the cooling process of high energy electrons with enregies greater than 10^3 eV. The contribution changes for lower energies.

Rotational and Vibrational Excitation

Atoms in molecules perform a periodic movement in relation to each other. This periodic movement can be classified into a rotational and a vibrational movement for linear molecules like the hydrogen molecule. The eigenstates of the movement can be excited by the collision with free electrons. The frequency of the eigenstate is dependent on the mass of the molecule as well as the electronic configuration of the molecule. Thus the energy levels of the oscillation are molecule specific. In this case the assumption that there is no isotopic difference between hydrogen and tritium is not well justified. The cross section for the excitation of hydrogen is also depicted in figure 2.16. It can be seen, that the rotational and vibrational excitation is not a dominant process at any energy. It has an small influence on the total cross section at energies of ≈ 10 eV. In the context of this thesis rotational and vibrational excitation are neglected due to their small contribution on the cross section. More information on the the possible isotopic difference might changes this decision.

Recombination with H^+

Electrons can directly recombine with a proton through radiative recombination

$$e^- + H^+ \longrightarrow \gamma + H\,. \tag{2.38}$$

This process was studied by Kotelnikove theoretically [34]. He found that the cross section for this reaction can be approximately calculated by

$$\sigma_r^{(0)} = \frac{2^8\pi^2}{3}\frac{\nu^6 e^{-4\nu\arctan(\frac{1}{\nu})}}{(1-e^{-2\pi\nu})(\nu^2+1)^2}\,\alpha^3 a_\mathrm{b} \tag{2.39}$$

$$\sigma_r = \sigma_r^{(0)}\cdot\frac{1.202+0.5782\log(\nu^2+1)+0.2148\log^2(\nu^2+1)}{1+0.3425\log(\nu^2+1)}\,, \tag{2.40}$$

where α is the fine structure constant, a_b the bohr radius and

$$\nu = \sqrt{\frac{J_z}{E_\mathrm{kin}}} \quad \text{with } J_z = \frac{e^4 m_e}{(2\hbar^2)}\,, \tag{2.41}$$

in cgs units. The cross section is depicted in figure 2.17 in comparison to the other recombination processes and in figure 2.18 in comparison to other proton processes. It can be seen that the cross section for recombination with protons is significantly lower than for other ions. Paired with a low density of single tritium ions it can be assumed that recombination with protons can be neglected in the description of the KATRIN plasma.

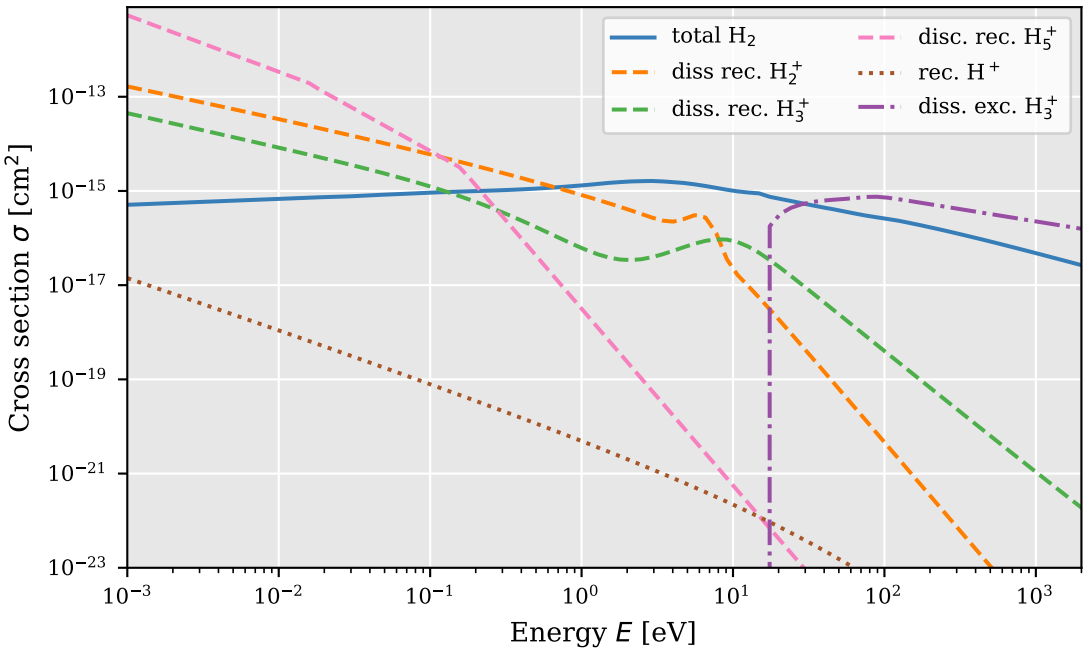

Figure 2.17.: Dissocitative recombination and dissocitatve excitation cross sections The energy describes the kinetic energy of the electron, when the interaction partner is at rest. Compared to the total cross section of electron-H_2 interactions from figure 2.16. Data taken from [29, 55, 34].

Dissociative Excitation and Recombination of H_2^+

Electrons and the hydrogen molecule H_2^+ can interact amongst others through dissociative excitation and dissociative recombination. The dissociative excitation occurs by "electron capture into a double excitade dissociative H_2 state or into a number of auto-ionizing dissociative Rydberg states"[29]

$$e^- + H_2^+(v) \longrightarrow H_2^{**} \longrightarrow e^- + H^+ + H \tag{2.42}$$

$$e^- + H_2^+(v) \longrightarrow H_2^{*\mathrm{Ryd}} \longrightarrow e^- + H^+ + H\,. \tag{2.43}$$

Dissociative recombination does occur by "direct capture of incident electron on a double excited state of H_2 ... or by vibrational excitation of H_2^+ and simultaneous capture of the electron on a dissociative auto-ionizing Rydberg state"[29]. The reaction equation is similar to equations 2.42 and 2.43 and reads as

$$e^- + H_2^+(v) \longrightarrow H_2^{**} \longrightarrow H + H \tag{2.44}$$

$$e^- + H_2^+(v) \longrightarrow H_2^{*\mathrm{Ryd}} \longrightarrow \ + H^+ + H\,. \tag{2.45}$$

The cross section of both the dissociative excitation and recombination can be found in figure 2.19 in comparison to other H_2^+ reactions. It can be seen that dissociate recombination is the dominant process over dissociatie excitation for energies below 0.5 eV. For energies above this threshold dissociate excitation is more dominant. The interaction probability is dependent on the density of the interaction partners. The ion density is higher at lower energies. Thus dissociate recombination will have a greater influence on the electrons and ions in the source than dissociative excitation.

The cross section of dissociative recombination is also depicted in figure 2.17 compared to recombination processes of electrons with other ion cluster sizes and to the total cross section of electron-H_2 interactions. It can be seen that

- the cross section of recombination with H_2^+ is comparable to other clusters. Thus it should have the same relevance at the descripition of the ions.
- the cross section of recombination is higher than the total cross section of electron-H_2 interactions. Nevertheless interactions with H_2 are more frequent due to the large density difference ($n_{T_2} \approx 1 \times 10^{15}\,\mathrm{cm}^{-3}$, $n_{T_i} \approx 1 \times 10^{6}\,\mathrm{cm}^{-3}$).

Dissociative Excitation and Recombination of H_3^+

The reaction formula of dissociative processes of H_3^+ clusters are similar to the dissociative processes of H_2^+ ions. The dissociative excitation occurs by the excitation to an intermediate highly excited state

$$\mathrm{e}^- + \mathrm{H_3}^+(v_3) \longrightarrow \mathrm{e}^- + \mathrm{H_3}^* \longrightarrow \mathrm{e}^- + \mathrm{H}^+ + 2\mathrm{H} \tag{2.46}$$

and the dissociative recombination occurs by electron capture to a double excited state or an excited Rydberg state and subsequent electron capture

$$\mathrm{e}^- + \mathrm{H_3}^+(v_3) \longrightarrow \left(\mathrm{H_3}^{**}, \mathrm{H_3}^{*\mathrm{Ryd}}\right) \longrightarrow \mathrm{H_2} + \mathrm{H}\,. \tag{2.47}$$

The corresponding cross sections are depicted in figure 2.17 in comparison to recombination processes with other ion clusters. It can be seen that dissociative excitation exhibit a threshold energy. The origin of this behavior is not stated in Janev *et al.* but was confirmed by various measurements [29]. Dissociative excitation is the dominant process above its thershold energy (15 eV) over dissociative recombination. Nevertheless the ion density is higher at lower energies. Thus dissociate recombination will have a greater influence on the electrons and ions in the source than dissociative excitation.

In figure 2.17the cross section of dissociative recombination is also depicted in comparison to recombination processes of electrons with other ion cluster sizes and to the total cross section of electron-H_2 interactions. It can be seen that

- the cross section of recombination with H_3^+ is comparable to other clusters. Thus it should have the same relevance at the descripition of the ions.
- the cross section of recombination is higher than the total cross section of electron-H_2 interactions. Nevertheless interactions with H_2 are more frequent due to the large density difference ($n_{T_2} \approx 1 \times 10^{15}\,\mathrm{cm}^{-3}$, $n_{T_i} \approx 1 \times 10^{6}\,\mathrm{cm}^{-3}$).

Recombination of D_5^+

There is only scarce data on the cross section of hydrogen clusters with sizes greater $i \geq 5$. The last available cross section data is published by Petterson *et al.* [48] for collisions of electrons with D_5^+ ions. They investigated the cross section by using an ion storage ring. Petterson *et al.* provide a numerical expression for the recombination cross section described by the following expression

$$\sigma(E) = \begin{cases} 10^{-14.87} E^{-1.20}\mathrm{cm}^2 & \text{for } 0.0005 \leq E \leq 0.017\,\mathrm{eV} \\ 10^{-15.93} E^{-1.78}\mathrm{cm}^2 & \text{for } 0.017 \leq E \leq 0.159\,\mathrm{eV} \\ 10^{-17.50} E^{-3.75}\mathrm{cm}^2 & \text{for } 0.159 \leq E \leq 1.0\,\mathrm{eV} \end{cases} . \tag{2.48}$$

The corresponding cross section is depicted in comparison to the other recombination processes in figure 2.17. It can be seen that the cross section is significantly higher at lower energies ($< 0.1\,\mathrm{eV}$) than for the other recombination channels. The density of T_5^+ is assumed to be only slightly lower than the density of T_3^+. Thus in total T_5^+ recombination should be as relevant as T_3^+ recombination at the experiment.

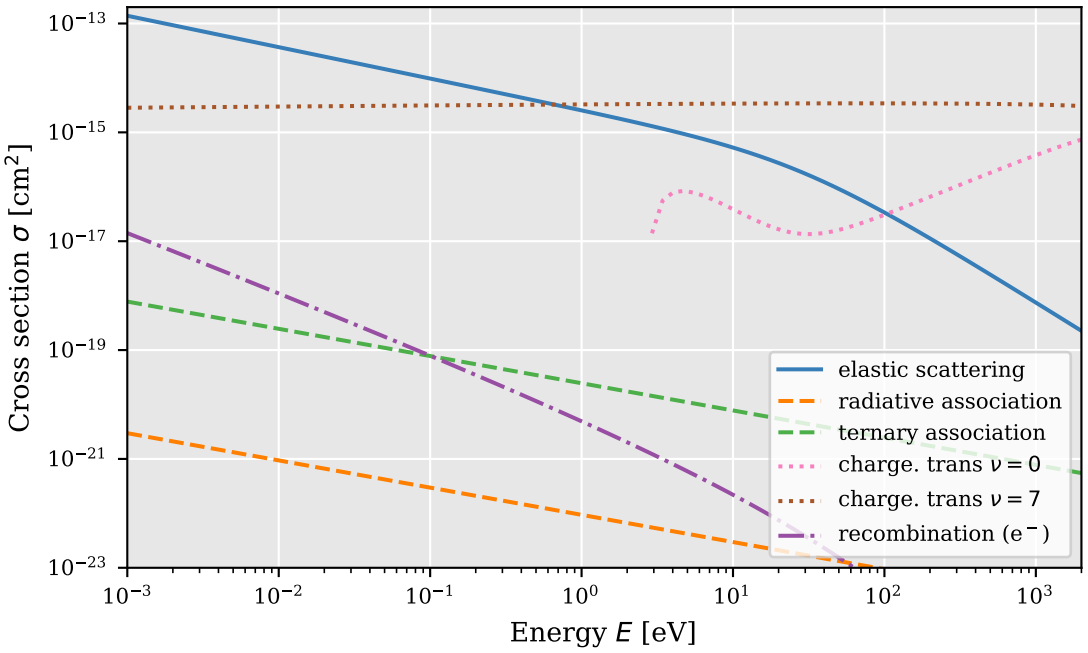

Figure 2.18.: Selection of H^+-H_2 cross sections The energy describes the kinetic energy of the ion, when the hydrogen molecule is at rest. Ternary association cross section calculated using a neutral gas density of $1 \times 10^{15}\,\mathrm{cm}^{-3}$ with data from [23]. Recombination cross section for comparison (in relation to the the kinetic energy of the electron). Data taken from [29, 55, 34]

2.4.3. Ion-Interactions

Interaction of ions can occur in collisions with electrons, with other ions and with neutral gas. As mentioned before the interaction probability depends on the density and the cross section of the interaction. Both the density of electrons and ions is significantly lower than the density of the neutral gas particles, whereas the cross section of the interaction is comparable. Thus interactions with the neutral gas occur more often. Hence this section will focus on interaction with neutral gas. Interactions of electrons and ions are described in the previous section and will not be discussed further here. Ion-ion interactions result in a similar interaction products as ion-neutral interactions and have similar cross sections [29]. Taken into account that the density of ions is much smaller than the density neutral particles any ion-ion interaction are neglected in the following.

In the context of this thesis only positive ions are investigated. Negative ions can be produced by radiative electron attachment to hydrogen or through electron impact dissociation of hydrogen molecules. The cross section of both reactions is small compared to other electronic interactions [29]. Thus they are not investigated further here.

In most cases there is no data available on interactions of tritium ions with molecular tritium but for their isotopic partners hydrogen or deuterium. Thus in the context of this thesis it is assumed that there is no isotopic effect between the isotopes.

2.4.3.1. Interactions of H^+ Ions

Hydrogen ions show multiple reaction channels with neutral hydrogen molecules. A conclusive summary is given by Tabata *et al.* [55] and Janev *et al.* [29] combining measurement data as well as theoretical calculations. The following description is based on their results.

Elastic Scattering

Elastic scattering of ions and neutral gas is significantly different than the elastic scattering of electrons with neutral gas. First the mass of ions is much higher. Thus the recoil of the ions needs to be taken into account after the interaction. Second ions are have a finite extension in comparison to the point like structure of electrons. Thus the elastic cross section is significantly higher for ions than for electrons.

The cross section of elastic scattering is depicted in figure 2.18. It can be seen that elastic scattering is the dominant interactions for ions below 0.5 eV. At the center of the WGTS the density of neutral particles is approximately $10^{15}\,\mathrm{cm}^{-3}$ at a temperature of 80 K. Thus the mean free path of ions in the center is in the order of 0.1 mm, see section 3.2.3. The mean free path is therefore much smaller than the size of the system. This means that ions will fulfill many elastic scatterings with the neutral gas. Hence it can be assumed that the ions will adapt the Maxwell-Boltzmann distribution from the neutral gas. The density is significantly reduced after the first two pump ports, see section 2.3.1.1. Thus the mean free path in this region is increased by the inversion proportion. Thus ions in this region can show a different energy distribution than the neutral gas.

Charge transfer

In a charge transfer reaction the proton interacts with a neutral molecule. One electron is donated by the molecule, which produces a hydrogen atom and a molecular ion

$$\mathrm{H}^+ + \mathrm{H}_2 \longrightarrow \mathrm{H} + {\mathrm{H}_2}^+ . \tag{2.49}$$

The cross section of this reaction is dependent on the initial vibrational state ν of the molecule. For $\nu = 0$, 1, 2 the reaction is endothermic. Thus there is an energy threshold for the reaction [29]. At higher vibrational states this reaction becomes exothermic and thus it looses its energy threshold.

The cross section of a charge transfer reaction with a molecule in ground state ($\nu = 0$) and an excited state ($\nu = 7$) can be seen in figure 2.18. It can be seen that charge transfer to a molecule in ground state is the dominant reaction above 100 eV. For lower energies the only charge transfer reaction with higher order clusters are relevant. The energy difference between two vibrational states is in the order of 1 eV. Thus it can be assumed that the molecules mostly reside in ground state because of their low temperature of 80 K. This means that charge transfer to higher states is suppressed. For a reaction with an molecule in ground state the ion needs an energies greater than the threshold energy. Thermal ions almost never have higher energies than the threshold energy. Thus it can be concluded that charge transfer to the ground state is negligible. In total it can be assumed that charge transfer plays only a secondary role in the development of the ions density distribution.

Radiative and Ternary Association

Hydrogen ions can form ion clusters with hydrogen through radiative and ternary association

$$\mathrm{H}^+ + \mathrm{H}_2 \longrightarrow {\mathrm{H}_3}^+ + \gamma\,, \tag{2.50}$$

$$\mathrm{H}^+ + \mathrm{H}_2 + \mathrm{H}_2 \longrightarrow {\mathrm{H}_3}^+ + \mathrm{H}_2\,. \tag{2.51}$$

Both the photon and the second molecule ensure conservation of momentum. Currently there is no data available on the cross section of both reactions. The cross section will be derived here from rate coefficients k measured by Gerlich *et al.* [23]. The corresponding conversion is presented in the following.

The number of particles which are created by a given reaction per given time interval is given by the reaction rate r. Is is calculated by

$$r = k \cdot n \,, \tag{2.52}$$

where k is the rate coefficient and n the density of the interaction partner. From a microscopic point of view this rate can be identified with the collision rate ν

$$\nu = \frac{v}{\lambda} \,, \tag{2.53}$$

where v is the mean velocity of the interacting particle and λ the mean free path, see section 3.3.3. The velocity can be calculated from the kinetic energy E of the interacting particle. The mean free path can be directly derived through the cross section and the density of the reaction partner

$$\lambda = \frac{1}{n\sigma} \,. \tag{2.54}$$

Thus in total the cross section can be written as

$$\sigma = \frac{k}{\sqrt{\frac{2E}{m}}} \,, \tag{2.55}$$

where m is the mass of the interacting particle.

This procedure can only be taken as a rough estimate of the cross section but can provide a first order approximation, when no data on the cross section is available. The cross section of a ternary process σ_3 can be derived similarly. In that case the the reaction rate is given by

$$r = k \cdot n^2 \,. \tag{2.56}$$

Thus the cross section of the ternary process can be calculated by

$$\sigma_3 = \frac{kn}{\sqrt{\frac{2E}{m}}} \,. \tag{2.57}$$

Gerlich *et al.* measured the rate coefficient for ternary and radiative association at different gas temperatures. As expected they found a temperature dependence. For a gas temperature of 80 K the rate coefficient were measured to be $k_R = 1.3 \times 10^{-16}\,\mathrm{cm^3 s^{-1}}$ for the radiative association process and $k_3 = 5.4 \times 10^{-29}\,\mathrm{cm^6 s^{-1}}$ for the ternary association process.

The corresponding cross sections for the association processes were calculated and are depicted in figure 2.18. The ternary process cross section was calculated using the maximal neutral particle density of $6.3 \times 10^{14}\,\mathrm{cm^{-3}}$, similar to the density in the center of the WGTS. Thus the values of ternary association only represent the maximal cross section. It can be seen that both cross sections are significantly lower than the cross section for elastic scattering. Thus elastic scattering is the dominant process over the association processes.

The overall relevance of the association processes for the experiment can be evaluated by comparing the collision frequency of the association with the mean time an neutral particle is in the central part of the source. See section 3.3.3 for more information on the collision rate. For a central density of $6.3 \times 10^{14}\,\mathrm{cm^{-3}}$ and a ternary cross section of $4.8 \times 10^{-19}\,\mathrm{cm^2}$ the ions collide each 0.14 s. The mean time of an hydrogen molecule spends in the source is in the order of 0.5 s. Thus association processes can occur in the source but a thorough investigation must be employed to determine the exact contribution.

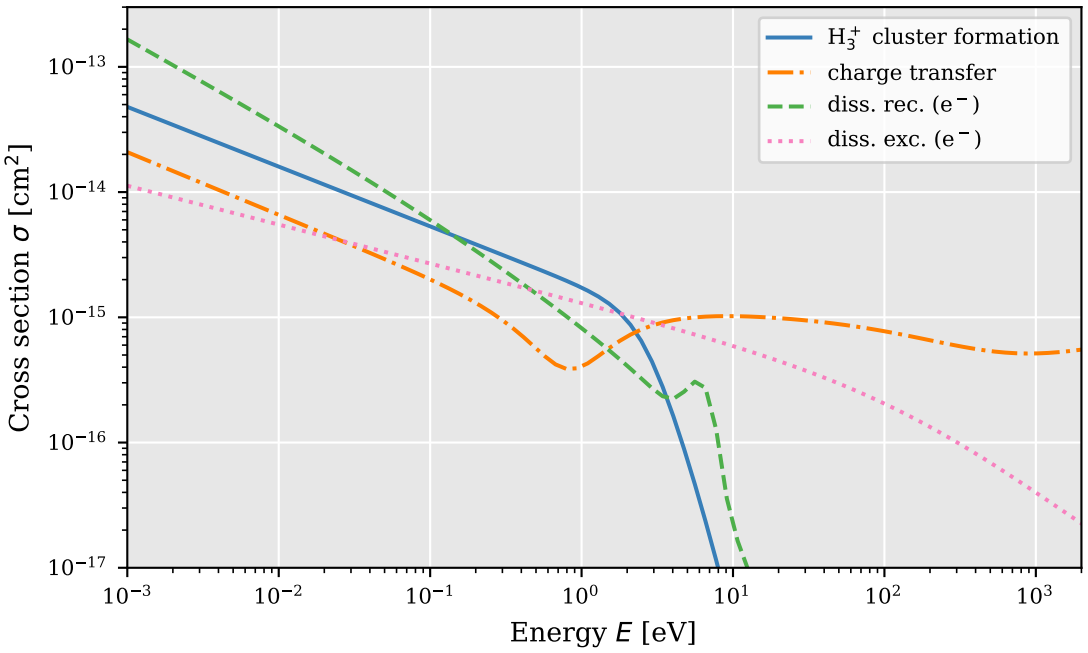

Figure 2.19.: Selection of H_2^+-H_2 cross sections The energy describes the kinetic energy of the ion, when the hydrogen molecule is at rest. Dissociative recombanition and dissociative excitation cross section for comparison (in relation to the the kinetic energy of the electron). Data taken from [29, 55]

2.4.3.2. Interactions of H_2^+ Ions

Hydrogen molecule ions show multiple reaction channels with neutral hydrogen molecules. A conclusive summary is given by Janev *et al.* [29] combining measurement data as well as theoretical calculations. A short summary of the interaction channels will be provided in the following. The dominant channels are cluster formation and charge transfer. Elastic scattering is suppressed, in contrast to hydrogen ions, where elastic scattering is the dominant interaction channel. Collisions with electrons (dissociative recombination and dissociative excitation) were already discussed in section 2.4.2.

Charge Transfer

In a charge transfer reaction the hydrogen molecule ion interacts with a hydrogen molecule. One electron is donated by the molecule to the ion and thus creating a new ion.

$$H_2^+ + H_2 \longrightarrow H_2 + H_2^+ . \tag{2.58}$$

Ions created in this way will therefore show a similar energy distribution like the neutral gas. The cross section of this reaction depends on the initial and final vibrational state of the particles. Nevertheless Janev *et al.* also provide a total cross section for the charge transfer, where a mean distribution of states is assumed. The corresponding cross section is depicted in figure 2.19 in comparison to other interaction channels. It is apparent that the charge transfer channel is dominant at energies greater than 2 eV. Nevertheless it also contributes significantly at lower energies to the total cross section, only surpassed by the cluster formation. The cluster formation however will suppress the importance of the charge transfer at the experiment because the H_2^+ ions will transform very efficiently to H_3^+.

Cluster Formation

Hydrogen molecule ions can form hydrogen ion clusters in a collision with hydrogen molecules either by proton transfer or by atom transfer. Most experimental studies investigated only the total cross section of both channels together. In the context of this thesis it is not differentiated between a hydrogen ion with an attached molecule or an hydrogen molecule ion with an attached atom. Thus the process reads as

$$H_2{}^+ + H_2 \longrightarrow H_3{}^+ + H\,. \tag{2.59}$$

The total cross section was measured for the vibrational ground state of both interaction partners. The cross section for higher vibrational states is determined through a linear scaling of the cross section of the ground state. The ratio of the cross sections is close to identity [29]. Thus in the context of this thesis only the cross section of the vibrational ground state is taken into account. The cross section of cluster formation is depicted in figure 2.19 in comparison to other interaction channels of $H_2{}^+$. It is apparent that the cluster formation channel is the dominant channel at energies below 2 eV. Thus it can be assumed that $H_2{}^+$ there is only a small amount of $H_2{}^+$ in the central part of the source, where collisions are frequent. In regions with smaller amount of neutral gas there is the possibility that the $H_2{}^+$ ions will survive.

2.4.3.3. Interactions of $H_3{}^+$ Ions

Hydrogen cluster ions mostly interact with neutral hydrogen molecules and electrons. Experimental data or theoretical calculations of the cross section for the interaction with hydrogen molecules is scarce due to the multitude of competing channels. In the context of this thesis the data from Tabata *et al.* [55] is used for the description of the elastic scattering and the results from Janev *et al.* [29] for the description of the collision induced dissociation. For a description of the reactions with electrons please refer to 2.4.2.

Elastic Scattering

The cross section for the elastic scattering were tabulated by Phelps *et al.* [49] through an investigation of drift velocities of $H_3{}^+$ in a H_2 gas. The data is only available in the range of 0.1 eV to 1 eV. In [55] an approximate formula was found to describe the data of Phelps. In the context of this thesis the formula of Tabata is used for all energies, even below 0.1 eV due to the lack of data. The cross section of the elastic scattering is depicted in 2.20 in comparison to other interaction channels. It is apparent that elastic scattering is the dominant interaction channel for energies below 20 eV. Thus it can be assumed that the ions will adopt the velocity distribution of the neutral gas in the center of the source. In regions with lower density the ions will continue with this velocity distribution, only influenced by electric fields.

Collision Induced Dissociation

Hydrogen cluster ions can be dissociated by collision with hydrogen molecules to either hydrogen or hydrogen molecule ions by forming an intermediate excited state

$$H_3{}^+ + H_2 \longrightarrow \left(H_5{}^*,\, H_3{}^{+*} + H_2\right) \longrightarrow H^+ + 2\,H_2 \tag{2.60}$$

$$\longrightarrow H_2{}^+ + H + H_2 \tag{2.61}$$

The collision energy must be greater than the binding energy of the cluster. Thus the reaction shows a threshold energy at 4.32 eV and 6.16 eV respectively [29]. The cross section of both reactions is dependent on the vibrational state of the reaction partners.

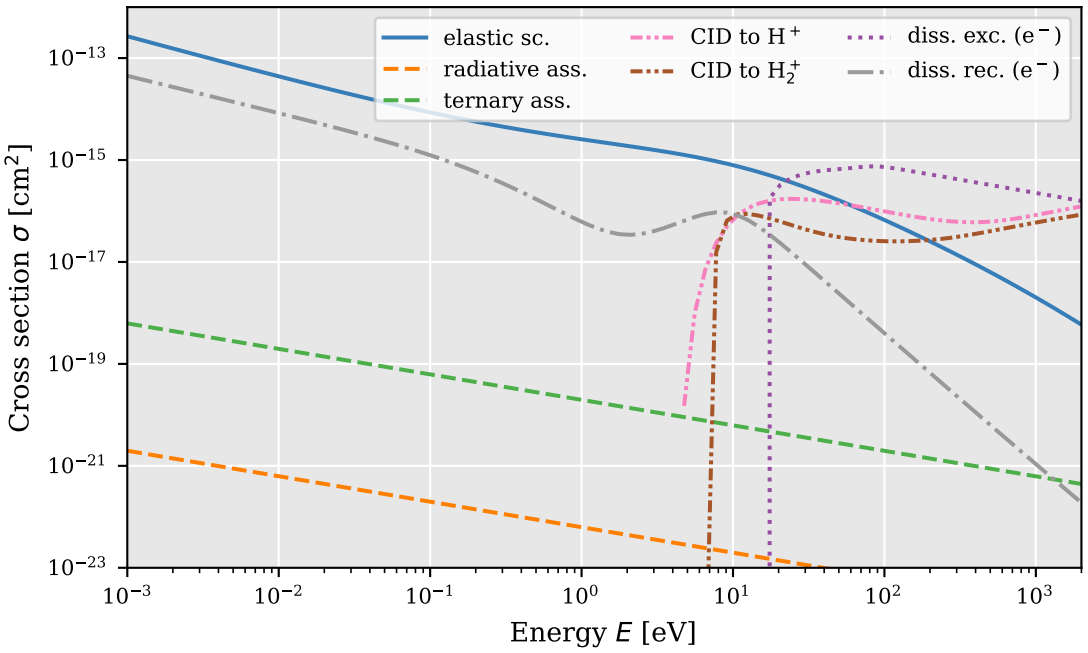

Figure 2.20.: Selection of H_3^+-H_2 cross sections The energy describes the kinetic energy of the ion, when the hydrogen molecule is at rest. Ternary association cross section calculated using a neutral gas density of $6.3 \times 10^{14}\,\mathrm{cm}^{-3}$ with data from [23]. Recombanition cross section for comparison (in relation to the the kinetic energy of the electron). Data taken from [29, 55, 34]

Nevertheless Janev *et al.* also provide a total cross section where a mean distribution of states is assumed. The corresponding cross sections are depicted in figure 2.20 in comparison to other interaction channels. It can be seen that the collision induced dissociation is the dominant process for energies above 100 eV. From the elastic scattering cross section it can be assumed that the ions will adopt the Maxwell-Boltzmann distribution of the neutral gas. Thus the ions will mostly have energies below 10^{-2} eV. Hence collision induced dissociation will not significantly influence the evolution of the ions.

Radiative and Ternary Association

Higher order cluster ions can be formed by radiative and ternary association

$$H_3^+ + H_2 \longrightarrow H_5^+ + \gamma \tag{2.62}$$

$$H_3^+ + H_2 + H_2 \longrightarrow H_5^+ + H_2\,. \tag{2.63}$$

Both the photon and the additional hydrogen molecule are necessary to fulfill the conservation of momentum. Similar to H^+ there is no data available on the cross sections. Gerlich *et al.* measured reaction rates $k_r < 0.5 \times 10^{-16}\,\mathrm{cm}^3/\mathrm{s}$ and $k_3 = 2.5\,\mathrm{cm}^6/\mathrm{s}$ at $T = 80\,\mathrm{K}$ for radiative and ternary association [23]. Thus the same procedure presented for the H^+ ions will be used here to derive an approximation for the cross section from the reaction rates, see section 2.4.3.1 and equations 2.55 and 2.57.

The corresponding cross sections for the association processes were calculated and are depicted in figure 2.20. The ternary process cross section was calculated using the maximal neutral particle density of $6.3 \times 10^{14}\,\mathrm{cm}^{-3}$, similar to the density in the center of the WGTS. Thus the values of ternary association only represent the maximal cross section. It can be seen that both cross sections are significantly lower than the cross section for elastic scattering. Thus elastic scattering is the dominant process over the association processes.

The overall relevance of the association processes for the experiment can be evaluated by comparing the collision frequency of the association with the mean time an neutral particle is in the central part of the source. See section 3.3.3 for more information on the collision rate. For a central density of $6.3 \times 10^{14}\,\mathrm{cm}^{-3}$ and a ternary cross section of $3.8 \times 10^{-19}\,\mathrm{cm}^2$ the ions collide each 0.15 s. The mean time of an hydrogen molecule spends in the source is in the order of 0.5 s. Thus association processes can occur in the source but a thorough investigation must be employed to determine the exact contribution.

2.4.3.4. Interactions of Higher Order Cluster Ions

Higher order ion clusters $\mathrm{H_i}^+$ can form though attachment of additional hydrogen molecules to existing ion clusters. There only scarce information on the interaction channels of these clusters in the literature. The only tangible data is available for creation and fragmentation rate coefficients of the clusters. Thus in the following it is only discussed whether higher order ion clusters exist in the KATRIN source or not. First the creation and fragmentation mechanism is described. Secondly the temperature dependence of the rate coefficients is discussed. Thirdly the implications of fragmentation at KATRIN conditions will be described.

Creation and Fragmentation

The relative density of higher order cluster depends on the creation and fragmentation processes. Paul *et al.* investigated these processes for a hydrogen gas at 10 K with a density of $10^{14}\,\mathrm{cm}^{-3}$ [46]. They found that in equilibrium there can be clusters of up to $i = 23$. Paul found that the primary creation mechanisms are ternary and radiative association with the rate coefficients $k_{3,i}$ and $k_{r,i}$, where i denotes the size of the initial cluster. The total creation rate coefficient $k_{g,i}$ can than be written as

$$k_{g,i} = k_{r,i} + k_{3,i}[\mathrm{H_2}]\,, \tag{2.64}$$

where $[\mathrm{H_2}]$ denotes the density of the background hydrogen gas. Paul *et al.* assume that the dominant fragmentation would occur through collision with neutral gas with the rate coefficient $k_{f,i}$. Thus the density of an ion cluster $[H_i+]$ can be derived from

$$\frac{1}{[\mathrm{H_2}]}\frac{\mathrm{d}[\mathrm{H_i}^+]}{\mathrm{d}t} = k_{g,i-2}[\mathrm{H_{i-2}}^+] + k_{f,i+2}[\mathrm{H_{i+2}}^+] - k_{f,i}[\mathrm{H_i}^+] - k_{g,i}[\mathrm{H_i}^+] \tag{2.65}$$

with the reaction equation

$$\mathrm{H_{i-2}}^+ \underset{k_{f,i}}{\overset{k_{g,i-2}}{\rightleftharpoons}} \mathrm{H_i}^+ \underset{k_{f,i+2}}{\overset{k_{g,i}}{\rightleftharpoons}} \mathrm{H_{i+2}}^+\,. \tag{2.66}$$

Equation 2.65 can be constructed for all possible indexes i. Thus the density of each specie can in general be determined by solving the coupled differential equation.

Assuming that the fragmentation rate increases with increasing order i and that there is a maximum order l an approximate fast solution to the differential equation can be found. The density of the highest order cluster $[H_l]$ then calculates to

$$[H_l] = [H_{l-2}]\frac{k_{g,l-2}}{k_{f,l}}\,. \tag{2.67}$$

Thus the ratio of the rate coefficients of creation and fragmentation can provide a measure for the density of the highest order cluster relative to the density of the predecessor. The largest cluster size is found if the ratio of fragmentation and creation is smaller than one. The measured creation and fragmentation rates of Paul *et al.* are depicted in figure 2.21. It

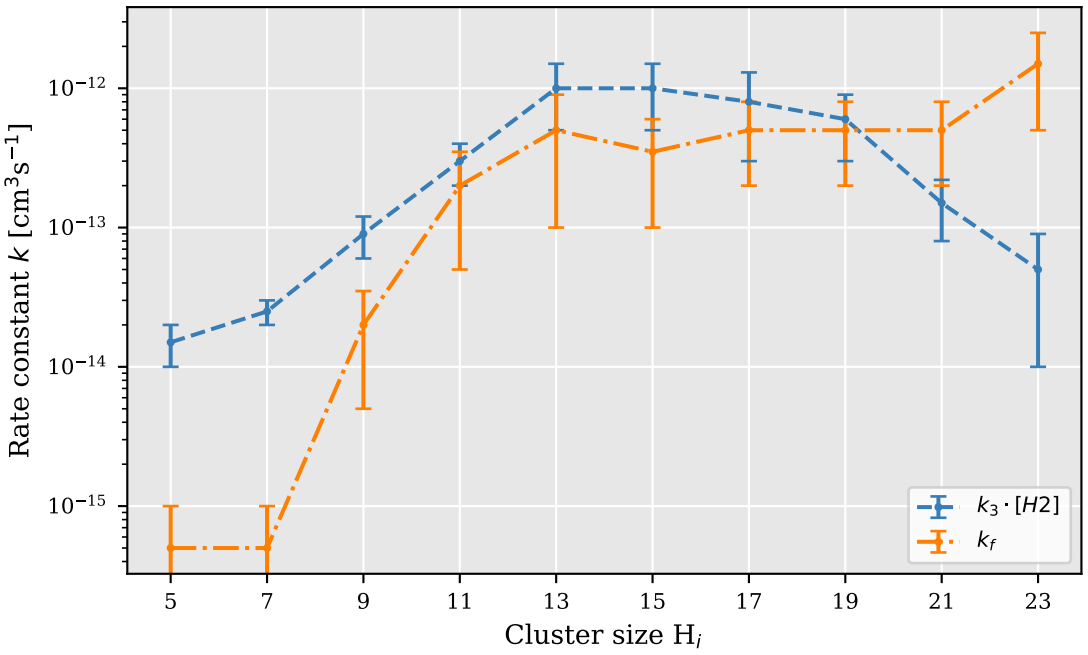

Figure 2.21.: Ion cluster creation and fragmentation at 10 K The ternary creation rate is scaled by the density of the hydrogen gas ($10^{14}\,\mathrm{cm}^{-3}$) for comparison of creation and fragmentation. Note that the large uncertainty of the fragmentation rate at cluster sizes $i = 5$, 7. The uncertainty in these cases is as high as the measured value itself. Data taken from [46]

can be seen that the ratio of fragmentation and creation is greater than one for indexes below 21. Following the argumentation from above this means that the highest cluster size should be 23. This estimation coincides with the measurements of Paul.

The measurements of Paul *et al.* can not be directly applied to the KATRIN source. The rate coefficient is in general dependent on the temperature of the reactants. Paul *et al.* measured the rate coefficients at 10 K. Thus for a description of the cluster in the KATRIN source a corresponding scale function of the coefficients needs to be found.

Creation Rate: Temperature Dependence

Paul *et al.* derived a T^-1 dependence of the ternary rate coefficient for H_5^+ clusters. In the context of this thesis it is assumed that the ternary rate coefficients of higher order clusters scale the same as H_5^+. This hypothesis can be tested by a comparison of the scaled rate coefficients to measurement data of Gerlich *et al.* [23]. They measured the ternary creation rate at 25 K for cluster sizes of up to $i = 11$ at a slightly lower hydrogen density $[H_2] = 3.7 \times 10^{13}\,\mathrm{cm}^{-3}$. Gerlich *et al.* state that there is a larger uncertainty on the creation rate of higher order cluster. The value of the uncertainty is not stated in the publication. The ternary creation rate of Gerlich *et al.* as well as the scaled creation rates of Paul can be found in figure 2.22. It can be seen that the scaled values of Paul are similar to the values measured by Gerlich. The values show a slight difference, which can be attributed to the measurement uncertainty of Gerlich.

It can be concluded that the temperature dependence of Paul can be used to determine the ternary rate at temperatures of the KATRIN source. The corresponding values can be found in figure 2.23.

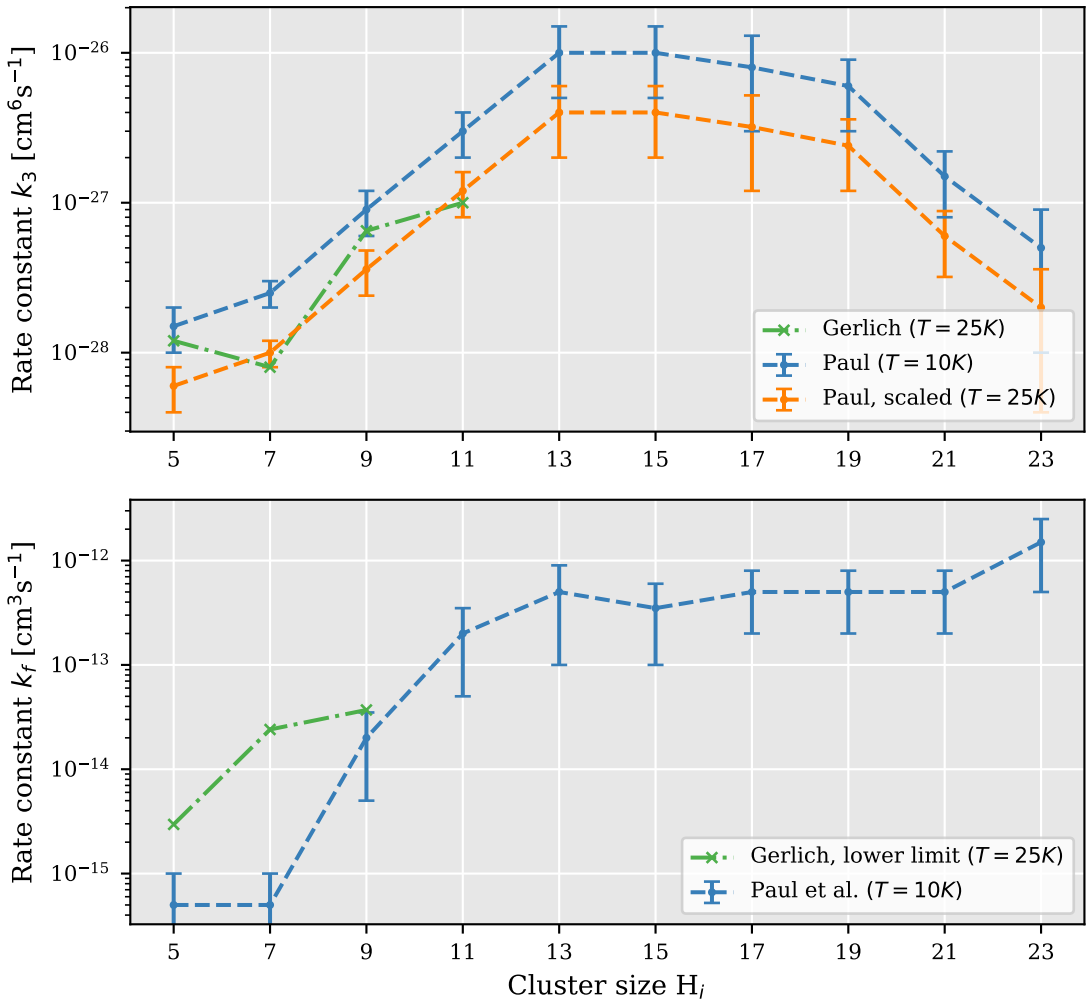

Figure 2.22.: Comparison of measurement and scaling Top: Comparison of the scaled creation rate of Paul *et al.* and the measured rates of Gerlich *et al.*. No uncertainties were provided in the data of Gerlich. Bottom: Comparison of the fragmentation rate of Paul and the lower limit determined through equation 2.67 from the data of Gerlich. Data taken from [46, 23].

Fragmentation Rate: Temperature Dependence

There is no conclusive data on the temperature dependence of the fragmentation constant in the literature. Paul *et al.* provide a possible scaling mechanism. This method is tested in the following by a comparison of the scaled values of Paul at 10 K to approximate values of Gerlich *et al.* at 25 K.

Paul *et al.* assume that the fragmentation cross section is proportional to $\sqrt{E - \Delta E}$, where ΔE is the binding energy of the cluster. Thus the rate coefficient of fragmentation can be calculated at higher temperatures from the standard Arrhenius expression

$$k_f = k_c \exp -\frac{\Delta E}{k_b T} \,. \tag{2.68}$$

The constant k_c can be calculated from the tabulated values of k_f of Paul at 10 K and from the binding energy. Paul determined the binding energy of clusters $i = 11$ to a range from 23 meV to 11 meV. The binding energy of higher order clusters is claimed to reach an equilibrium value of 9 meV. For smaller clusters $i = 5$, 7, 9 Harrison *et al.* determined the

Table 2.2.: Binding energies and fragmentation rates. Measured rates of Paul *et al.* were scaled using the Arrhenius experission from equation 2.68. Data taken from [26] and [46]

cluster index i	5	7	9	11	13
ΔE (meV)	260	17	108	11	11
$k_f(10\,\mathrm{K})$ ($\mathrm{cm^{-3}s^{-1}}$)	1.5×10^{-28}	2.5×10^{-28}	9.0×10^{-28}	3.0×10^{-27}	1.0×10^{-26}
$k_f(25\,\mathrm{K})$ ($\mathrm{cm^{-3}s^{-1}}$)	2.1×10^{63}	6.9×10^{-11}	9.1×10^{18}	4.2×10^{-10}	1.1×10^{-9}

binding energy to 260 meV, 17 meV and 108 meV respectively [26]. The fragmentation rate can now be calculated at higher temperatures.

Gerlich *et al.* could show that clusters up to index $i = 9$ exist at 25 K [23]. Gerlich *et al.* do not provide any data on the fragmentation rate coefficient. A limit on the fragmentation rate can be derived through equation 2.67 and through the observation that the density of the clusters was lower than the initial density of H_3^+. Thus the fragmentation rate of these clusters was lower than the creation rate. The creation rates can therefore be used as an lower limit on the fragmentation rates for the measurement of Gerlich *et al.*.

The limits on the fragmentation rate of Gerlich can now be compared to the hypothesis of Paul. The values at higher temperatures are calculated using equation 2.68 and the corresponding binding energies of Paul and Harrison. The scaled fragmentation rates can be found in table 2.2. It can be seen that the fragmentation rate of small cluster sizes is extremely large. This would mean that there are no clusters at 25 K. This is contradicted by the fact that Gerlich measured clusters at this temperature. It can therefore be concluded that either the Arrhenius expression can not be used in the way described above or that the binding energy has lower values than proposed.

Nevertheless it can be observed that the lower limit on the fragmentation rate of Gerlich is greater than the corresponding fragmentation rate of Paul. It can therefore be assumed that the fragmentation rate is further increased at temperatures greater than 25 K. The number of particles which have energies greater than the binding energy will increase at least linear with the temperature. Thus the fragmentation rate should at least scale linear as well.

Cluster Sizes at KATRIN

The results of Paul *et al.* and Gerlich *et al.* can be used to provide a limit on the cluster sizes in the KATRIN source. The creation rate can be scaled directly to 80 K. The corresponding values are depicted in figure 2.23 for a central neutral particle density of $6.3 \times 10^{14}\,\mathrm{cm^{-3}}$. The fragmentation rate can not be quantified directly at 80 K. Three possible different methods can be used to define a lower bound on the fragmentation rate:

1. The measured fragmentation rate of Paul is used directly.
2. The fragmentation rate is at least as high as the measured creation rate of Gerlich.
3. The fragmentation rate can be scaled linearly. The parameters are defined by the fragmentation rates of 1. and 2.

The corresponding values of each method are depicted alongside the creation rates in figure 2.23.

The maximal cluster size in the KATRIN source will be determined here following equation 2.67. Thus the maximal cluster size is reached if the fragmentation rate is bigger than the creation rate. The maximal cluster size is dependent on the method employed to determine

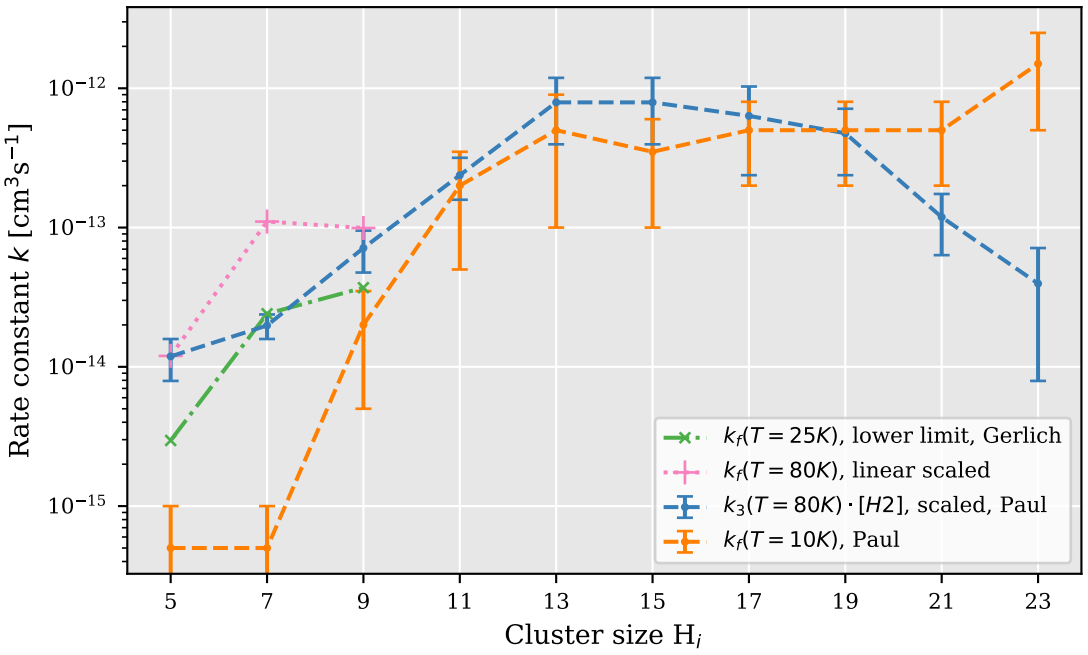

Figure 2.23.: Clustering at 80 K Creation rate scaled from Paul and adjusted to a neutral denisty of $6.3 \times 10^{14}\,\mathrm{cm}^{-3}$. Fragmentation rate either from measurements of Paul directly, derived from the data of Gerlich using equation 2.67 or through linear scaling through both data of Gerlich and Paul. Data taken from [46, 23].

the fragmentation rate from above. The conclusion of each case is summarized by the following

1. The creation rate is well above the fragmentation rate up to index $i = 9$. The uncertainties above this index are large enough that the fragmentation rate could be higher than the creation rate. This is even more pronounced considering that the fragmentation rate of 10 K is only the lower limit of the fragmentation rate at 80 K. The maximal cluster size index $i = 21$ is, when only considering the measured value without the uncertainties.

2. A maximal cluster size can not determined in this case. It can only be deduced that the density of H_7^+ is lower than the density of H_5^+. No conclusion can be given for higher cluster sizes.

3. The fragmentation rate is well above the creation rate it index $i = 7$. Thus the maximum cluster size in this case is $i = 5$.

It can be seen that there is no conclusive result on the maximal cluster size from the data of creation and fragmentation rates. Further investigation is necessary.

In the discussion above only interactions of ions with neutral gas were considered, whereas there is a non negligible amount of electrons with energies greater than the binding energy of the cluster ions. The data in the literature on these collisions is very scarce. Following the argumentation of Miderski *et al.* it can be assumed that the recombination rate coefficient for a H_5^+ cluster is increased dramatically in contrast to the recombination rate of H_3^+. Thus it can be assumed that the cross section for dissociative collisions is increased as well. Hence many higher order clusters will be destroyed by electron collisions.

For the description of the plasma only cluster sizes of up to index $i = 5$ will be considered. It is assumed that the density of higher order clusters is negligible.

2.5. Measurements on the Source Plasma

The KATRIN experiment is equipped with many different methods to investigate the source plasma experimentally. These methods revolve around either on the measurement of electrons of the source, which will have gained or have lost energy through the plasma or on the measurement of particle fluxes leaving the source. In the first category fall krypton line measurements, the Pro-KATRIN measurements and egun measurements. In the second category fall the measurements of the rear wall current and the measurement of the dipole ion flux. A selection of these measurement techniques will be described in the following and a short summary of the current findings will be presented. The investigations are still ongoing. Thus this will only provide a preliminary few of the data and will provide a short insight in the current experimental exploration of the plasma.

The KATRIN experiment offers many ways to influence the source plasma. While this can be used to reduce the effects of the plasma on the neutrino mass measurement these methods can also be used to investigate the plasma itself. These methods include among others the adaptable magnetic field strength in all parts of the source, the variation of the potential at the rear wall and the dipole electrodes, the variable tritium density in the source and the introduction of additional electrons to the source through a illumination of the rear wall. These methods will be employed in some of the investigations shown below.

2.5.1. Krypton Line Measurements

^{83m}Kr is a metastable isotope which produces monoenergetic electrons in its decay. Some of the conversion electrons have energies close to the tritium beta endpoint energy. Others can reach energies up to 32 keV. "The isotope has a short half-life of 1.83 h and, as a noble gas with no long-lived daughters, can be allowed to diffuse through the experimental apparatus without the risk of long-term radioactive contamination." [6]. Thus ^{83m}Kr is an ideal candidate for commissioning and calibration measurements.

At the KATRIN experiment gaseous krypton is injected into the source. The krypton then decays and thus provides its monoenergetic conversion electrons. The spectrum of the conversion electrons is then measured with the KATRIN detector. The injection of krypton can be done in an empty source and also with tritium inside the source. Thus a comparison of these measurements can provide insight on the plasma properties.

In 2019 a measurement of the krypton conversion lines K-32, L_3-32 and $N_{2,3}$-32 was performed in an empty source. Both the line position and line width of the conversion was determined with an unprecedented accuracy [6]. The measured electrons originate from different positions in the source. Thus the line position and line width are dependent on the conditions at these positions. One of these conditions is the potential at the decay position, named starting potential. Its mean value throughout the source increases or decreases the line position, while its spatial and time distribution increases the line width.

The same measurement can be performed with tritium background gas. Thus a different line positions and line widths can be determined with a plasma inside the source. It is assumed that the plasma is not effected by the presence of Krypton. Thus the difference in line position and width can be attributed to the presence of the plasma. Its main contribution is in the exertion of the plasma potential. Thus the line position is raised by the mean plasma potential $\bar{U}(r)$, where the average is derived over the length of the source. The line width $\sigma(r)$ is increased by a convolution of the density distribution of the krypton gas $n_{\mathrm{Kr}}(r, z)$ with the distribution of the plasma potential $U(t, r, z)$. The plasma potential distribution can not be determined directly through this measurement. Nevertheless these measurements can provide limits on the influence of the plasma on the neutrino mass measurements. Moreover these measurements constrain possible plasma

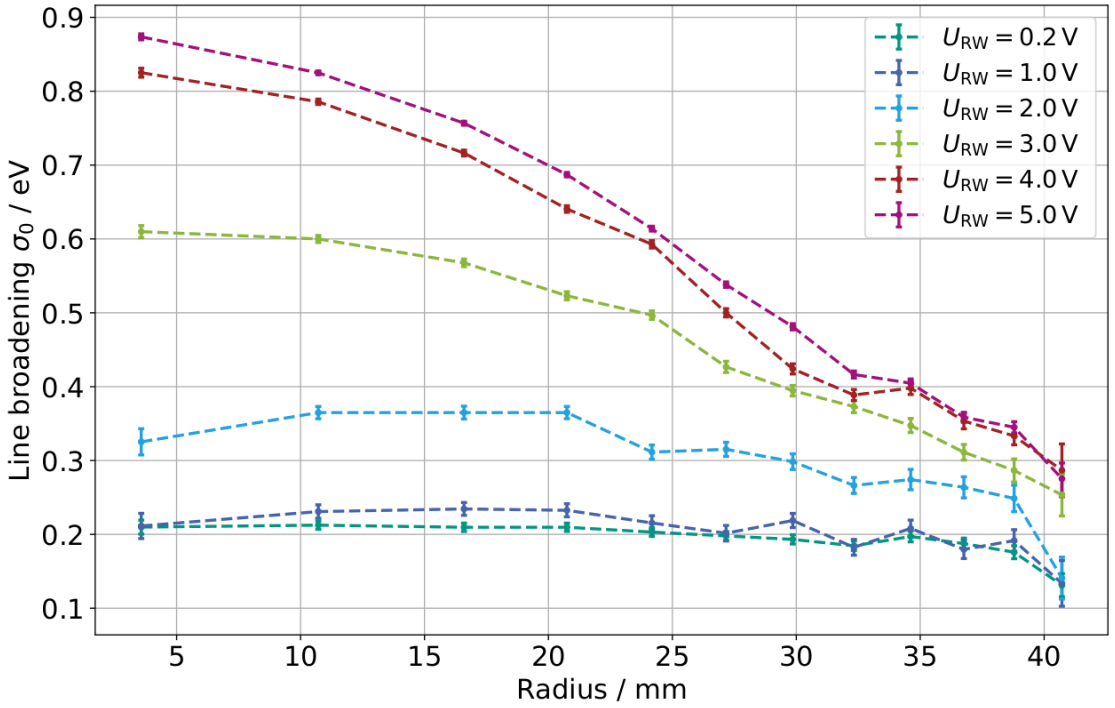

Figure 2.24.: Line width Measurement of the line width for different rear wall potentials from the measurement campaign KNM2. Figure taken from [44]

models experimentally and are therefore an important contribution in the investigation of the plasma.

The boundary conditions of the source can have a great influence on the plasma potential. It can be assumed that there exists a specific potential difference of the rear wall and the tube walls at which the plasma potential has the smallest effect on the neutrino mass measurement. The krypton line width can provide insights onto this specific set value of the rear wall potential. The line width can be determined experimentally in relation to the rear wall potential. An exemplary measurement is shown in figure 2.24. It can be seen that the line broadening is vastly influenced by the rear wall potential. This influence is different for different radii. Thus there exists a plasma potential distribution for which the longitudinal variance is radial dependent. In general it can not be concluded that a radial homogeneous line broadening will result in the smallest effect on the neutrino mass measurements. The description of the deconvolution of the line position and line broadening to the plasma potential exceed the context of this thesis. For more information please refer to the dedicated study by Machatschek [42]. Also the influence of other source conditions like the magnetic field and particle density will be described there.

The measured line widths and line positions can be compared with simulated values obtained by simulation of the plasma. Thus the Krypton measurements can be used to constrain the plasma model. The plasma model can then be used to find optimal values of the rear wall potential.

2.5.2. Particle Current Measurements

The measurement of the electric current of particles leaving the source can provide a valuable insight on the plasma inside the source. It can either be used for monitoring of the source or it can be used to probe the predictions of the different descriptions of the plasma.

Charged particles inside the KATRIN source are created by the beta decay of tritium and subsequent ionization of the surrounding gas. The number of charged particles n inside the

source can be described by the continuity equation

$$\frac{\partial n}{\partial t} + \nabla \mathbf{j} = k_c(n) - k_r(n)\,, \tag{2.69}$$

where j is the particle current leaving the source, k_c the creation rate of new particles through ionization and beta decay and k_r the recombination rate. Additionally it can be assumed that the number of charged particles reaches a steady state after a sufficient long time. Thus the sum of all electrical currents I_i leaving the source is equal to zero

$$0 = \sum_i I_i\,. \tag{2.70}$$

The total current of particles leaving the source can not be measured because of the intricate design of the source. In general it can be assumed that charged particles can leave the source either by a collision with the tube walls, by a collision with the rear wall or by a collision the dipole electrodes of the DPS. The dominant channel is dependent on the type of particle. Ions can move to both directions of the source and can neutralize at the rear wall (I^i_{rw}) as well as on the dipole electrodes (I^i_{dp}). Whereas electrons are reflected either by the potential of the dipole electrodes or at the potential of the spectrometers. Thus they mostly neutralize at the rear wall (I^e_{rw}). The number of electrons leaving the apparatus at the detector can be neglected at this point, provided the small count rate at the detector. In conclusion equation 2.70 can be written as

$$0 = I^e_{\mathrm{rw}} + I^e_{\mathrm{t}} + I^i_{\mathrm{rw}} + I^i_{\mathrm{dp}} + I^i_{\mathrm{t}}\,, \tag{2.71}$$

where I^e_{t} and I^i_{t} describe the electric current of electrons and ions respectively neutralizing at the tube walls. In a previous model of the plasma [37] it was assumed that the electrical current towards the tube walls can be neglected due to the large magnetic field inside the source. Current measurements have shown that the sum of all measured currents is only zero for a specific rear wall voltage U_0, see figure 2.25. Thus the measurements have shown that the plasma models need to be adapted to include also an electric current towards the beam tube. Thus the measurement of currents provide a valuable insight to the plasma. For more information on these types of measurements please refer to the work of Friedel [17]. Also the influence of other source conditions like the dipole electric field strength, source temperature and neutral particle density will be described there.

2.5.3. Pro-KATRIN Measurements

The measured electron flux at the detector depends in first order on the initial electron energy and the difference between the potential at the starting position in the source and the potential at the analyzing plane in the main spectrometer. Thus a measurement of the rate where the starting potential is increased would yield the same result as if the potential at the main spectrometer is lowered. This method allows for an investigation of the influence of external potentials on the potential inside the source, especially the rear wall potential. The method can also be used to find an optimal rear wall potential for the neutrino mass measurements. Thus it is also called *plasma rear wall optimization at KATRIN*, in short PRO KATRIN.

In the description of Kuckert [37] it is assumed that the potential inside the source is dominated by the potential at the rear wall. This assumption is based on a fluid description of the plasma. It is hypothesized that the strong magnetic field in the source causes a high conductivity in longitudinal direction and a low conductivity in radial direction. Thus the potential of the rear wall would penetrate deep into the plasma. This hypothesis can be tested with the PRO KATRIN method. A exemplary measurement is shown in figure

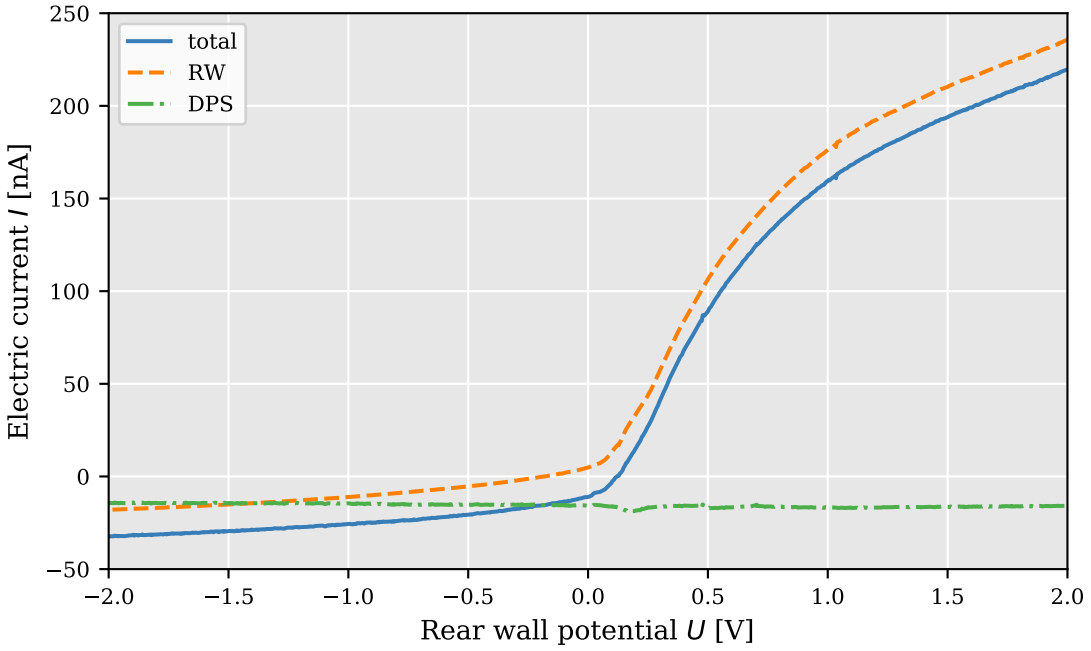

Figure 2.25.: Measured electric currents leaving the source Data from the rear wall (RW) and from the dipole electrodes in the DPS. Total current is the sum of both measurement points. Data from [17].

2.26. Three different regions can be identified there. The first is the potential range −0.2 V to 0.5 V. Here a change in the rear wall potential result in the same shift as a change in the main spectrometer potential. The second range comprises all rear wall potential values below −0.2 V. Here the rear wall potential has a negligible effect on the rate at the detector. The third region contains all rear wall potential values above 0.5 V. Here a change of the rear wall potential has less effect than the change in the main spectrometer potential, but is not negligible. At KATRIN these three ranges are also called maximally-coupled region, decoupled region and partly-coupled region. From the measurements it can be concluded that there exists indeed a region, where the potential inside the source is dominated by the rear wall potential as hypothesized by Kuckert. Nevertheless there exist also rear wall potential values, where this assumption does not hold true. Optimally a full description of the plasma will also include these values as well. Thus a measurement with the PRO KATRIN method allows for testing of plasma models.

The PRO KATRIN method can also be used to investigate the stability of the source. The potential values at which there is a transition between the regions is dependent on the specific conditions inside the source. A change in the plasma conditions will also result in a change in the transition value. For more information on the PRO KATRIN method please refer to the work of Friedel [17]. There the method will be described in detail, including additional investigation of the regions depending on the radius inside the source. These results can provide valuable insights into the plasma and its radial potential distribution in conjunction with the krypton measurements.

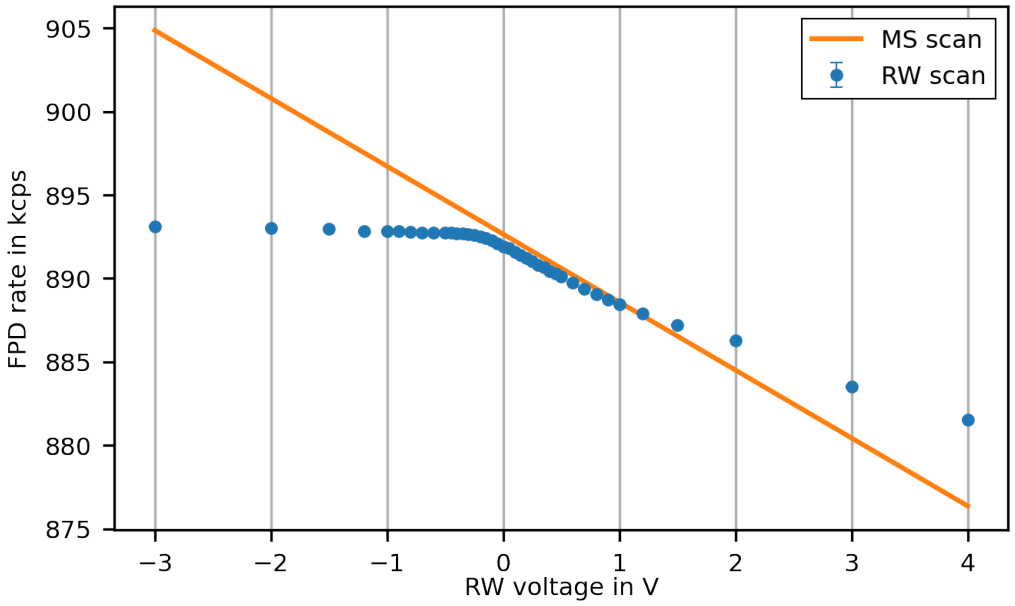

Figure 2.26.: Pro Katrin Measurement Exemplary measurement data from the measurement campaign KNM2. Figure from [17].

Chapter 3
Classification of the KATRIN Plasma

This chapter focuses on the specific classification of the plasma at the KATRIN experiment. Therefore first a short introduction into plasmas will be given. Then characteristic length scales and characteristic frequencies will be discussed for conditions at the experiment. These parameters then allow for a discussion of suitable models to describe the plasma. Two different models will be presented thereafter: a fluid approach of a previous work and a partly collisional model developed in the scope of this thesis.

3.1. Introduction to Plasmas

There is no common definition, what a plasma is. Hermann and Preppernau define a plasma as "the entirety of relatively free moving charged particles, which interact with each other through electromagnetic forces. The total system, where the entirety of the charged particles belong to must be neutral to the outside"(translated from [28]). Cap defines a plasma similarly, but adds that the core properties of the medium must be influenced by the presence of the entirety of the charged particles [13]. The presence of free moving charged particles is not sufficient enough to describe a plasma. The charged particles must show a collective behavior. Thus a common salt solution can be described as a plasma whereas the particle cloud at high energy accelerators might not be described this way [13].

There exists many different characteristics which describe a plasma, see sections 3.2 and 3.3 for a in depth description. Some of these can be used to determine if there exists a plasma. One easy accessible property is the quasineutrality.

From the definitions above it is apparent that the absolute number of charged particles is not relevant in these definitions of a plasma, but rather that the number of positive and negative charges must be approximately equal. Assume that there are negative and positive charged particles in a sphere with the densities n_e and n_i respectively. The total charge Q in this sphere with radius R can be written as

$$Q = -\frac{4\pi R^3}{3}(n_e - n_i)e\,. \tag{3.1}$$

The electric field at the radius r with $r \geq R$ is then calculated by

$$E = \frac{Q}{r^2} = -\frac{4\pi}{3}(1-a)\frac{R^3}{r^2}n_e e\,, \tag{3.2}$$

with the relative density factor $a = n_i/n_e$. The electric field at the rim of a sphere with radius $R = 1\,\mathrm{cm}$, a charge density of $n_e = 1 \times 10^{15}\,\mathrm{cm}^{-3}$ and the small relative density of $a = 0.99$ will then be $E = 6.03 \times 10^6\,\mathrm{V/cm}$. This large electric field will then restore the quasineutrality. Thus it can be assumed that there exists quasineutrality in all plasmas.

This condition will be broken if there are boundary conditions involved or if there exists oscillations with a sufficient high frequency [13].

The plasma condition is influenced by many parameters like the density of the charged particles, the density of neutral particles, the magnetic field and many others. These parameters can have a wide range of values. Thus there exists also many different theoretical models of plasmas, see section 3.4. In order to distinguish between these models characteristic parameters can be employed. A selection of these parameters will be described in the following.

3.2. Characteristic Length Scales

The characteristic length scales of a plasma mostly rely on the consideration of the interactions between the charged particles, neutral particles, and electromagnetic fields. In this section first the most dominant effect of plasmas, the Debye shielding will be described. The Debye length can then be used to classify if there exists a collective behavior of the charged particles. Secondly the Landau length will be discussed, which provides an insight into spontaneous recombination processes. The discussion is followed by a description of the mean free path. This parameter will provide an overview of the dominant processes apart from electromagnetic interactions. After that the gyro radius will be brought into focus, followed by a description of the inertial length. The inertial length can then be used to give a limit on boundary effects. The section will be concluded by a comparison of the parameters presented before. This comparison then allows for a classification of the plasma.

3.2.1. Debye-Length

The Debye length λ_D describes the length of the screening effect of the plasma, where the electric field of a single charged particle is attenuated by the presence of other charged particles. Consider a positive ion in free space. The electric field of the ion follows the Coulomb's r^{-2} law. The interaction strength has therefore an infinite range. Consider the same ion in a cloud of electrons and other ions. The ion will attract electrons and repel other ions such that the electric field of the ion is reduced to a bare minimum at a certain distance. This distance is called Debye-length. A graphical representation of this behavior together with the potential of a free charge can be seen in figure 3.1.

The electric potential for a debye sphere can be calculated from the Poission equation (in cgs)

$$\nabla\phi = \frac{1}{r^2}\frac{\mathrm{d}}{\mathrm{d}r}r^2\frac{\mathrm{d}\phi}{\mathrm{d}r} = -4\pi e(n_e - Zn_i)\,, \tag{3.3}$$

where n_e and n_i describe the density of electrons and ions respectively. Electrons and ions are assumed to follow the Boltzmann statistics

$$n_i = n_{i,0}\,\exp\left(-\frac{Ze\phi}{k_bT}\right) \tag{3.4}$$

$$n_e = n_{e,0}\,\exp\left(\frac{e\phi}{k_bT}\right)\,, \tag{3.5}$$

with the temperature T and Boltzmann's constant k_b. Equation 3.3 can the be rearranged assuming quasineutrality and that the electric potential is much smaller that the thermal energy of the particles ($e\phi \ll k_bT$):

$$\frac{1}{r^2}\frac{\mathrm{d}}{\mathrm{d}r}r^2\frac{\mathrm{d}\phi}{\mathrm{d}r} = 4\pi e^2 n_{e,0}\frac{1+Z}{k_bT}\phi\,. \tag{3.6}$$

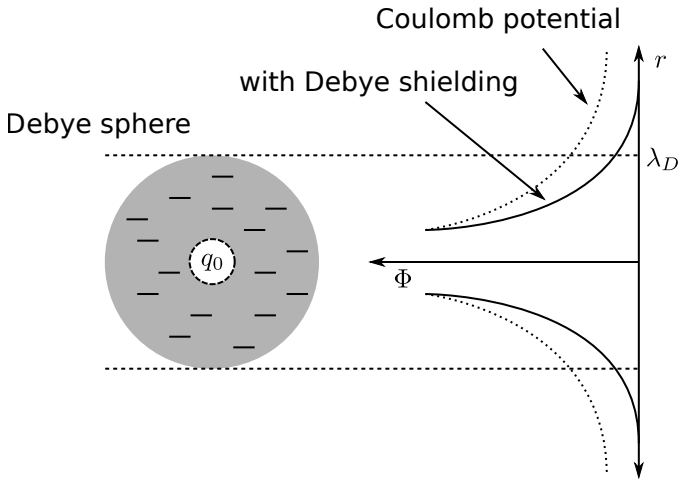

Figure 3.1.: Debye Shielding A single charge q_0 will be surrounded by other charges forming the Debye sphere. The electric potential Φ of this charge will be reduced from the infinite range of the Coulomb potential to a finite length in the order of the Debye length λ_D. Figure adapted from [54]

This differential equation is solved by the ansatz

$$\phi(r) = \frac{1}{r} \exp\left(-\frac{r}{\lambda_D}\right) . \tag{3.7}$$

Thus the Debye length λ_D can be calculated by

$$\lambda_D = \sqrt{\frac{k_b T}{4\pi e^2 n_{e,0}(Z+1)}} . \tag{3.8}$$

It can be seen from equation 3.7 that the potential drops to a value of $1/e$ at the radius $r = \lambda_D$. Thus the presence of other charged particles decreases the influence of the electric field of a single particle. The Debye length can therefore provide a limit on the length at which single particle effects play a role in a cloud of charged particles. For length smaller than the Debye length direct particle interactions have to be considered while for length greater than the Debye length the collective behavior of the plasma takes over.

In section 3.1 it was stated that charged particles can be considered as a plasma if there exists a collective behavior of the charged particles. Thus the Debye length can be used in conjunction with the mean distance between charged particles a to determine if the particles have to be treated as a plasma. Collective behavior is to be assumed when

$$a < \lambda_D . \tag{3.9}$$

The same result can be obtained by requesting that there must be enough charge carriers in the near vicinity to justify a continuous description of the particles. This relation can be written as

$$\Lambda := \frac{4\pi}{3} \lambda_D^3 n_e \gg 1 , \tag{3.10}$$

where Λ is called the plasma parameter. This relation is equivalent to equation 3.9 by identifying the mean distance between charged particles with the inverse cubic root of the particle density $n_e^{-1/3} = a$.

Debye-Length at the KATRIN experiment: It can be assumed that the electrons have thermal energies in the center of the source, due to elastic collisions with the neutral gas. The gas has a temperature of 80 K, see section 2.3.1.2. The electron density is not constant in the source. Simulations with KARL source code, see chapter 4, show that the electron density ranges from $10^4\,\mathrm{cm}^{-3}$ to $10^7\,\mathrm{cm}^{-3}$. Thus the Debye length has values of 0.6 cm and 0.02 cm respectively. The Debye length is depicted in figure 3.3 in comparison with other characteristic length scales.

It is apparent that the plasma condition of equation 3.9 is fulfilled for all possible electron densities at the KATRIN source. Thus the charged particles in the source will show a collective behavior. The relative factor between the Debye length and the mean distance of particles is small in comparison to other plasmas. Thus the plasma at the KATRIN experiment can be described as a plasma with a low density.

3.2.2. Landau Length

The Landau length l_L describes the distance at which the electrostatic energy of two charged particles in a plasma is equal to the kinetic thermal energy of these particles. The Landau length can therefore be calculated as

$$l_l = \frac{e^2 Z}{k_b T}\,. \tag{3.11}$$

The mean distance between particles a must be greater than the Landau length to ensure that recombination processes play only a secondary role in the plasma:

$$a > l_L\,. \tag{3.12}$$

Landau length at the KATRIN experiment: The Landau length is only dependent on the temperature of the electrons. It can be assumed that the electrons have thermal energies in the center of the source, due to elastic collisions with the neutral gas. The gas has a temperature of 80 K, see section 2.3.1.2. Thus the Landau length at the experiment is 1.8×10^{-9} cm. The Landau length is depicted in figure 3.3 in comparison with other characteristic length scales.

It is apparent that the Landau length is much smaller than the mean distance between charged particles. Thus it can be assumed in first order that the charged particles will not recombine spontaneously through their thermal motion. The Landau length is additionally much smaller than the Debye length. This implies that direct charged particle interactions are negligible [13] for thermal particles in the source.

3.2.3. Mean Free Path

The mean free path λ describes the distance a particle will move statistically between two collisions. It can be derived from the probability that a particle will interact by flying through a particle cloud, see equation 2.27. The probability that a particle can be detected after a distance x then reads as

$$\mathcal{P}(x) = e^{-x/\lambda}\,. \tag{3.13}$$

Thus the mean free path describes the point at which this probability is decreased to a value of $1/e$. This distance can be directly calculated from the density of the traversed particle cloud n and the total cross section of the interaction σ through

$$\lambda = \frac{1}{\sigma n}\,. \tag{3.14}$$

Table 3.1.: Mean free path. Approximate values of the mean free path for densities similar to the densities at the rear wall and the center of the source.

		Rear wall	Center
n_e	[cm^{-3}]	10^4	10^7
n_{T2}	[cm^{-3}]	10^{12}	10^{15}
$\lambda(e^-\text{-}T_2)$	[cm]	1600	1.6
$\lambda(T_3{}^+\text{-}T_2)$	[cm]	17	0.017
$\lambda(e^-\text{-}e^-)$	[cm]	8400	10

Limitations of the mean free path: The mean free path can only be calculated if the total cross section has finite values. The cross section is in general dependent on the energy and the scattering angle. Thus to obtain the total cross section of an interaction a integral over all possible scattering angles has to be performed. This integral diverges for the Coulomb interaction between two free moving charged particles, because of the infinite range of the electromagnetic force. Thus it would not possible to determine the mean free path for the collision of electrons with electrons. The electromagnetic force in a plasma is limited due to the Debye shielding. Thus the integral can be performed for particles in a plasma. Assuming that the particle energy is equal to the Boltzmann energy $E = k_b T$ the cross section can be approximated to

$$\sigma \approx \frac{4\pi e^4 Z^2}{k_b^2 T^2} \ln\left(\frac{\lambda_D}{l_L}\right) . \tag{3.15}$$

Please refer to the work of Cap [13] for a full description of the derivation. This cross section has to be adapted for each interaction, electron-electron, electron-ion, ion-ion.

Mean free path at the KATRIN experiment: The mean free path is dependent on the energy of the interacting particle through the energy dependence of the cross section. In the following it is assumed that all electrons and ions have thermal energies, due to the collisions with the neutral gas of the source. The cross section is in most cases decreased with increased energy. The mean free path of thermal energies can therefore be used as a lower limit.

The electron density is not constant in the source. Simulations with KARL source code, see chapter 4, show that the electron density ranges from $10^4\,cm^{-3}$ at the rear wall to $10^7\,cm^{-3}$ in the center of the source. The neutral particle density also varies over the length of the source from $10^{12}\,cm^{-3}$ at the rear wall to $1 \times 10^{15}\,cm^{-3}$ in the center of the source, see section 2.3.1.1. Thus the mean free path will show significantly different values, depending on the position in the source. The position at the rear wall and in the center of the source will be used in the following to provide upper and lower limits on the mean free path. The corresponding values can be found in table 3.1. These values are also depicted in figure 3.3 alongside other characteristic length scales.

The values of the mean free path allow for the following conclusions:

- The mean free path of ions in the center is much smaller than the diameter $D = 9\,cm$ and length $L = 1300\,cm$ of the source tube. It can therefore be assumed that ions will have many interactions before coming in contact with the tube walls. Thus the ions in the center will show a similar velocity distribution as the neutral gas, see section 2.3.1.
- The mean free path of ions at the rear wall is comparable to the diameter of the source. Hence the velocity distribution of the ions can deviate from the velocity distribution of the neutral gas.

- The mean free path of electrons in the center is smaller than the dimensions of the source tube. Hence the electron velocity distribution will show some characteristics of the velocity distribution of the neutral particles. Nevertheless the Debye length and mean distance between particles is smaller than the mean free path of the electrons. Hence plasma effects will play a vital role in the description of the electron movement. The difference of the mean free path and the Debye length is comparably small. Hence a description of the plasma in the central region of the WGTS has to include scattering as well.
- The mean free path of electrons at the rear wall is greater than the geometric details of the source. Hence electron interactions with neutrals can be neglected here.
- The mean free path of electron-electron Coulomb interactions is comparably high to the other mean free paths and to the Debye length. Hence direct interactions of electrons with electrons play a secondary role. A fluid description of the electrons is therefore not justified. See section 3.4 for more information on the different plasma models.

3.2.4. Gyro Radius and Classical Diffusion

The magnetic field of the KATRIN source is very strong (2.5 T). Thus the movement of charged particles is heavily influenced by this field. The charged particles perform a radial movement around the magnetic field lines. The radius of this motion is given by the Larmor radius r_L, also named gyro radius. It is calculated by

$$r_L = \frac{m v_\perp c}{cB}\,, \tag{3.16}$$

where $v_\perp$ is the velocity perpendicular to the direction of the magnetic field, m the mass of the charged particle and B the magnetic field strength. The perpendicular velocity can be expressed in terms of the temperature T in the case of thermal movement of charged particles.

$$r_L \approx \frac{c}{eB}\sqrt{\frac{8 k_b T m}{\pi}} \tag{3.17}$$

Gyroradius at the KATRIN experiment: The gyro radius is only dependent on the temperature of the particles and the magnetic field strength. It can be assumed that the electrons have thermal energies in the center of the source, due to elastic collisions with the neutral gas. The gas has a temperature of 80 K, see section 2.3.1.2. Thus the gyro radius for electrons is 7.9×10^{-6} cm and for ions 1.0×10^{-3} cm. The gyro radius of both species is depicted in figure 3.3 in comparison to other characteristic length scales.

The electron gyro radius is much smaller than the ion gyro radius. This is expected due to the large mass difference. The gyro radius for both electrons and ions is smaller than any other characteristic length, except the Landau length. Hence the magnetic field will play a vital role in the description of the plasma.

Electrons and ions which are created close to the wall can be diverted by the magnetic field, so that these particles hit the wall in one gyro motion. This effect plays only a very minor role as both ion and electron gyro radius are much smaller than the diameter of the WGTS.

Electrons and ions can collide with neutral gas during the gyro motion. If this collision has a large scattering angle the center of gyration will be shifted to another position, also

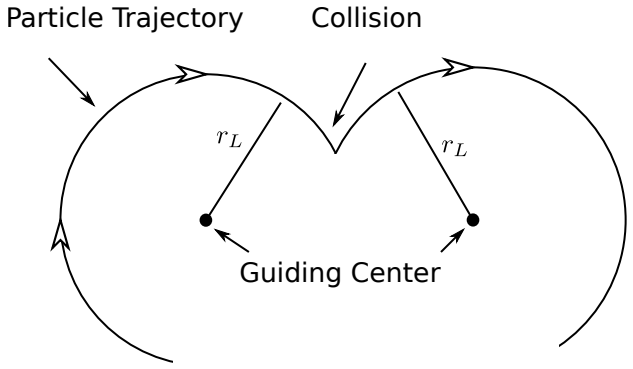

Figure 3.2.: Classical diffusion. The particle is gyrating around the guiding center until collision. The guiding center after collision can be different from the guiding center before collision. Thus particles can diffuse across magnetic field lines.Figure adapted from [14]

seen in figure 3.2. Thus the particle can traverse in radial direction. This motion can be described by the classical diffusion coefficient D. It can be approximated by

$$D \approx \nu\, r_L^2\,, \tag{3.18}$$

where ν is the collision frequency. This diffusion coefficient is much smaller for electrons than for ions due to the significant difference in the gyro radius. It can therefore be assumed that diffusion due to collisions can be relevant for ions, but not for electrons. This assumption has to be tested in a thorough simulation.

3.2.5. Inertial Length

The inertial length of electrons describes the depth to which an external light wave can penetrate into a plasma. For this reason it is also called skin depth. The inertial length is calculated from the dispersion relation of a so called Langmuir or plasma mode. This mode is generated by charge density differences in the plasma. For more information on the plasma mode please refer to section 3.3.1. Light waves will traverse the plasma undisturbed if the frequency of the incoming wave is much greater than the plasma frequency. In that case electrons can not follow the change of electric field due to their inertia. If the frequency of the incoming wave is smaller that than the plasma frequency,the electrons will cancel out the displacement current. The wave can not penetrate the plasma is this case and becomes evanescent [54]. The penetration depth of the wave is given by the electron inertial length and is calculated by

$$l_{\text{skin}} = \frac{c}{\omega_{\text{pe}}}\,, \tag{3.19}$$

where ω_{pe} is the plasma frequency. The plasma frequency is proportional to the square root of the electron density. Thus the skin depth proportional to the inverse square root of the electron density.

Inertial length at the KATRIN experiment: The electron density is not constant in the source. Simulations with KARL source code, see chapter 4, show that the electron density ranges from $10^4\,\text{cm}^{-3}$ to $10^7\,\text{cm}^{-3}$. Thus the inertial length has values of 5300 cm and 170 cm respectively. The inertial length is depicted in figure 3.3 in comparison with other characteristic length scales.

It can be seen that the skin depth is one of the largest length scale of the plasma. It is greater much greater than the diameter of the WGTS and only slightly smaller than the length of the source tube. Hence it can be assumed that boundary effects will play a vital role in the description of the plasma. Nevertheless there is a strong magnetic field in the KATRIN source, whereas the derivation of the skin depth assumes a non magnetized plasma. A more precise evaluation can be given by simulation.

3.2.6. Summary

In the previous sections the Debye length, the Landau length, the mean free path, the gyro radius and the inertial length were discussed. Each parameter was described individually and key differences to the other parameters was provided. In this section the focus lies on the overall conclusion of all the parameters, especially for the description of the plasma. The parameters are depicted in figure 3.3 in dependence to the electron density.

Single particle vs Collective behavior: First the focus lies on the distinction if the charged particles in the source have to be treated as single particles or if they show a collective behavior and thus have be treated as a plasma. The following conclusions can be made from the characteristic length scales:

- $\lambda_D > a$, $\Lambda > 1$: The particles in the source can show a collective behavior.
- $L > \lambda_D$, $D > \lambda_D$: The collective behavior of the particles is dominant in the source. A treatment of the particles as a plasma is necessary. Single particle treatment has do be employed at scales below λ_D
- $a > l_L$: Electrons and ions will not recombine through thermal motion.

Hence it can be concluded that the particles in the source have to be treated as a plasma.

Plasma models: There exist many different models describing plasmas, see section 3.4. The choice of model is dependent on the characteristic length scales. A suitable model can be found with the following conditions:

- $R_e \ll L, D$, $R_i \ll L, D$, $R_e \ll \lambda_D$: Electron and ion motion is dominated by the magnetic field. Thus the plasma is strongly magnetized.
- $\lambda_{e,c} > \lambda_D$: Collisions of electrons with neutrals play a secondary role in the center of the WGTS. Nevertheless they have to be considered because of the small the difference of the parameters. Thus the plasma in the center is partly collisional.
- $\lambda_{e,rw} \gg \lambda_D$: Collisions of electrons with neutrals do not play a role close to the rear wall. Thus the plasma is collisionless here.
- $\lambda_{ee} \gg \lambda_D$: Electron-electron collisions are very infrequent. The electrons can not be treated as a fluid.
- $\lambda_{i,c} < \lambda_D$: Ions interact very often with the neutral gas in the center of the WGTS. Their movement will be collision dominated.
- $\lambda_{i,rw} \gg \lambda_D$: Ions will interact seldomly with neutral gas close to the rear wall. Their movement will be dominated by plasma effects.

It can be concluded from this that the plasma model needs to treat the plasma as a strongly magnetized, low density, partly collisional, bound, multi species, partially ionized plasma with thermal and non thermal components of low but finite temperature.

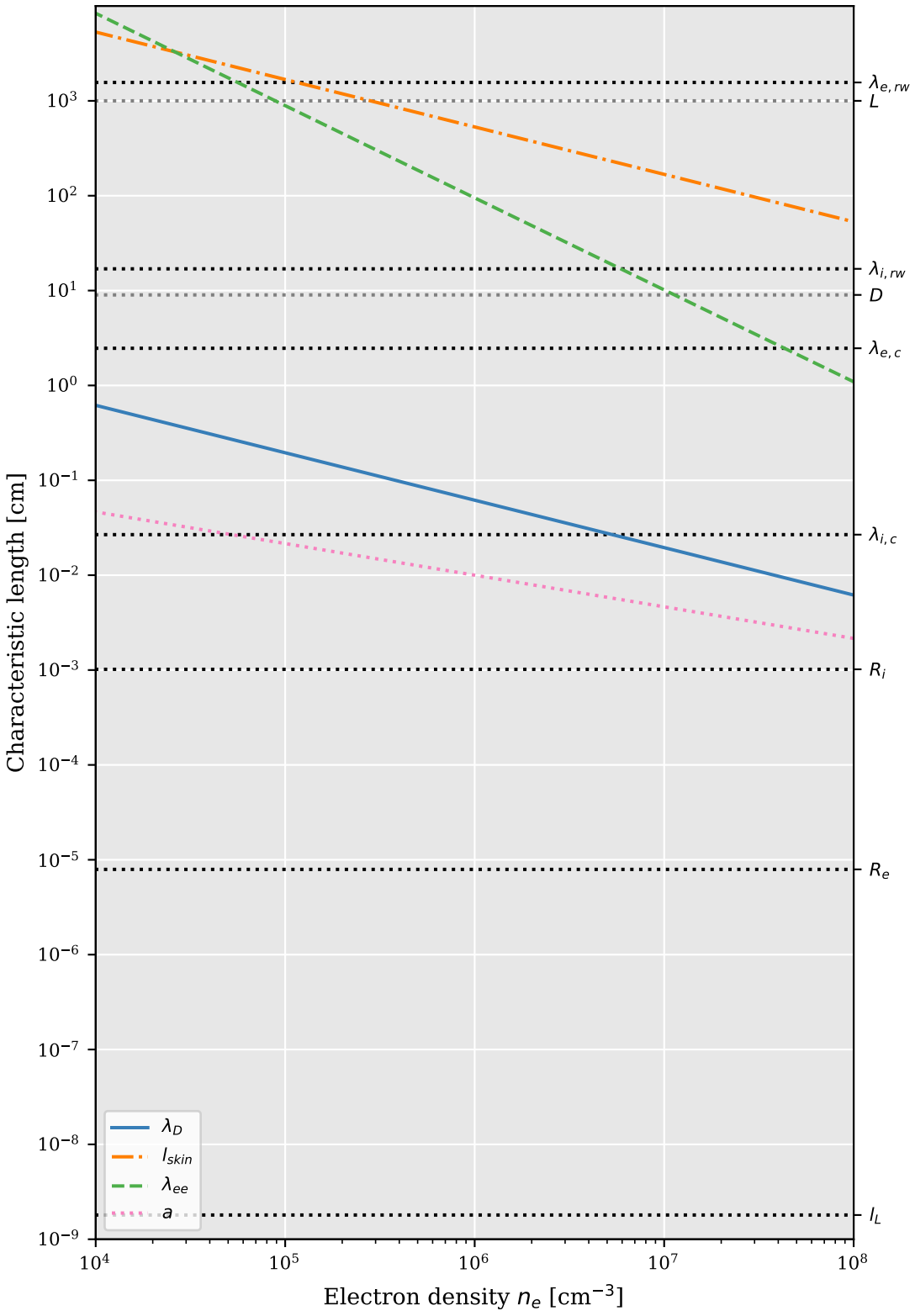

Figure 3.3.: Characteristic length scales. λ_D: Debye length, a: mean distance between electrons, L: length of the source, D: diameter of the source, l_{skin}: inetrial length, $\lambda_{e,rw}/\lambda_{i,rw}$: mean free path of electrons/ions in front of the rear wall, $\lambda_{e,c}/\lambda_{i,c}$: mean free path of electrons/ions in the center of the source, λ_{ee}: mean free path of electrons due to Coulomb interactions. Neutral density: in front of rear wall $1 \times 10^{12}\,\text{cm}^{-3}$, in center $6.3 \times 10^{14}\,\text{cm}^{-3}$. Magnetic field: 2.5 T. Temperature: 80 K.

3.3. Characteristic Frequencies

The characteristic frequencies of a plasma mostly rely on the consideration of the interactions between the charged particles, neutral particles, and electromagnetic fields. The frequencies can provide an insight weither an effect has to be included in the description of the plasma or if it can be neglected.

In this section first the plasma frequency will be described. It provides a natural time scale at which plasma effects play a role. Secondly the gyro frequency will be discussed, which provides an insight into synchrotron radiation processes. The discussion is followed by a description of the collision rate. This parameter will provide an overview of the dominant processes. The section will be concluded by a comparison of the parameters presented before.

3.3.1. Plasma Frequency

The plasma frequency ω_p describes the density oscillation of electrons and ions, where the quasineutrality has been perturbed. It can be derived for cold plasmas with no magnetic field, see [13], and calculates to

$$\omega_p^2 = \omega_{pe}^2 + \omega_{pi}^2 \tag{3.20}$$

$$\omega_{pe} = \sqrt{\frac{4\pi n_e e^2}{m_e}} \tag{3.21}$$

$$\omega_{pi} = \sqrt{\frac{4\pi n_i Z^2 e^2}{m_i}}\,, \tag{3.22}$$

where n_e, n_i, m_e and m_i are the electron and ion density and mass respectively. ω_{pe} describes the oscillation of electrons and ω_{pi} describe the oscillation of ions. In general it can be assumed that the ion and electron density is equal. Thus the plasma frequency of the electrons ω_{pe} is much higher than the plasma frequency of the ions ω_{pi} due to the large mass difference and the total plasma frequency is dominated by ω_{pe}.

The plasma frequency provides a limit on the frequency of light waves which can traverse the plasma. Waves with frequencies below the plasma frequency become evanescent, while waves with frequencies much greater than the plasma frquency can traverse the plasma undisturbed. Additionally the plasma frequency can be used as a natural time scale of plasma effects which relate to electron movement.

Plasma Frequency at the KATRIN experiment: The electron density is not constant in the source. Simulations with KARL source code, see chapter 4, show that the electron denisty ranges from $10^4\,\mathrm{cm}^{-3}$ to $10^7\,\mathrm{cm}^{-3}$. Thus the plasma frequency of electron has values of $9.0 \times 10^6\,\mathrm{rad/s}$ and $2.9 \times 10^7\,\mathrm{rad/s}$ respectively, whereas the plasma frequency of ions has values of $7.0 \times 10^4\,\mathrm{rad/s}$ and $2.2 \times 10^5\,\mathrm{rad/s}$ respectively. The plasma frequency of each specie is depicted in figure 3.4 in comparison with other characteristic frequencies.

It can be seen that the plasma frequency is not larger than the gyro frequency of the system. This is notworthy because the plasma frequency in allmost all standard types of plasmas is the highest frequency [13]. Only gas discharges show a similar behavior. A comparison of the KATRIN plasma and gas discharges is not gainfull because the charged particle density and the temperature is much smaller at the KATRIN experiment. Thus both plasma will behave differently.

3.3.2. Gyro Frequency and Synchrotron radiation

While the gyro radius describes the radius at which charged particles move around the guiding center the gyro frequency describes the rotationaly frequency of this movement. It is calculated by

$$\Omega = \frac{eB}{mc}\,, \tag{3.23}$$

where m is the mass of the particle and B the magentic field strength. Thus the gyro frequency is different for electrons and ions.

The strong magnetic field at the KATRIN source forces the particles to gyrate with a very high frequency. It is therefore necessary to investigate the enregy loss due to synchrotron radiation. The characteristic frequency f_R at which the kinetic energy of a particle is reduced to a factor $1/e$ is given by

$$f_R = \frac{4e^2\Omega^2}{3mc^3} = \frac{4e^4B^2}{3m^3c^4}\,. \tag{3.24}$$

It is apparent that f_R decreases with the mass and thus is much higher for electrons than for ions.

Gyro Frequency and Synchrotron Loss at the KATRIN experiment: Both the gyro frequency and the sychrotron loss frequency are independend on the charged particle density in the source but soleley on the magnetic field strength in the source. The magnetic field in the source is 2.5 T. Thus the gyro frequency of electrons is 4.4×10^{11} rad/s and of ions is 2.7 rad/s. Both frequencies are very high in comparison to all other frequencies in the system, see figure 3.4. This means that the particles will perform many gyrations before all other interactions.

The sychrotron loss frequency for electrons is 2.4 Hz. It is small in comparison to the collision frequencies in the system. Thus many interactions will have taken place in between the radiation. Hence these losses do not play a vital role in the description of the plasma. Nevertheless they will be modeled in the kinetic simulations presented in chapter 5. Radiation losses have to be taken into account for the neutrino mass measurement, where also small energy losses have to be taken into account. The synchrotron loss frequency of ions is well below any frequency and is therefore not further mentioned here.

3.3.3. Collision Rate

The collision rate ν or collision frequency describes the mean time between two collisions of a particle in a cloud of other particles. It can be dierctly derived from the mean velocity of a particle $\bar{v}$ and the mean free path λ

$$\nu = \frac{\bar{v}}{\lambda} = \bar{v}\sigma n\,. \tag{3.25}$$

The mean velocity of a thermal particle is calculated from the standard Boltzmann statistics.

Collision Frequency at the KATRIN experiment: The collision frequency is dependent on the density and the energy. Due to the extreme amount of parameters only the collision rate of the elastic scattering with neutral gas, recombination and Coulomb interactions of electrons will be presented here. The collision rate increases directly with the velocity of the incoming particle, in contrast to the mean free path. Here only thermal velocities of ions and electrons are used to reduce the number of parameters.

The collision frequency is dependend on the density of the traversed particle cloud. The electron density is not constant in the source, as mentioned before. Simulations with KARL

source code, see chapter 4, show that the electron denisty ranges from $10^4\,\mathrm{cm}^{-3}$ at the rear wall to $10^7\,\mathrm{cm}^{-3}$ in the center of the source. The neutral particle density also varies over the length of the source from $10^{12}\,\mathrm{cm}^{-3}$ at the rear wall to $1 \times 10^{15}\,\mathrm{cm}^{-3}$ in the center of the source, see section 2.3.1.1. Thus the collision frequency will show significantly different values, depending on the position in the source. The position at the rear wall and in the center of the source will be used in the following to provide upper and lower limits on the collision frequency.

The collision frequency of elastic scattering with neutral gas is in the center of the source approximately $10^6\,\mathrm{Hz}$, see figure 3.4. This value is similar for electrons and ions, despite the large difference of the cross section. This is caused by the large velocity difference between the two species. It can be observed that the elastic collision frequency is below the plasma frequency. Nevertheless it can not be concluded from this fact that collisions do not have an influence on the development of plasma modes. The interplay of collisions, electromagnetic fields and paricle motion is too extensive for this conclusion.

The collision frequency of elastic scattering wtih neutral gas in front of the rear wall is approximately $10^3\,\mathrm{Hz}$, see figure 3.4. Again this value is similar for electrons and ions. The elastic collision frequency does not provide any more insight despite that is is higher than the synchrotron loss frequency. Hence synchrotron losses do not play a role in the description of the plasma in this low neutral density section of the source.

The elastic collision rate is lower than the gyro frequency of the corresponding species. Therfore the particles will perform multiple gyro motions until they interact through collision. The collision rate is much greater than the collision rate of Coulomb interactions and recombinations. Thus elastic scattering is the dominant effect over the others.

3.3.4. Summary

In the previous sections the plasma frequency, the gyro frequency, the synchrotron losses, and the collision rate were discussed. Each parameter was described individually and key differences to the other parameters was provided. In this section the focus lies on the overall conclusion of all the parameters. The parameters are depicted in figure 3.4 in dependence to the electron density.

The time scales can, in contrast to the length scales, not be used directly to determine if the particles have to be treated as a plasma. Nevertheless the time scales can provide an insight into the characteristics of the plasma.

- $\nu_{eT_2} \gg \nu_{ee}$: Direct electron interactions play only a secondary role. A pure electron fluid approach is not viable here.
- $\nu_{eT_2} \gg \nu_{\mathrm{rec}}$: Recombination is only a secondary effect in the source.
- $f_R \ll \nu_{eT_2}$: Cyclotron radiation can be neglected for the description of electrons in the soucre. This is also true for ions.

The survey of the time scales can provide a limit on relevant effects which influence the plasma through their temporal evolution. These effects have to have frequencies which are similar to the frequency of the influenced particle. Thus if the temperature of the beam tube would change at a frequency of 1 Hz it would not influence the plasma by its temporal evolution but through its value. The temperature can in this case be assumed to be constant for all plasma related effects.

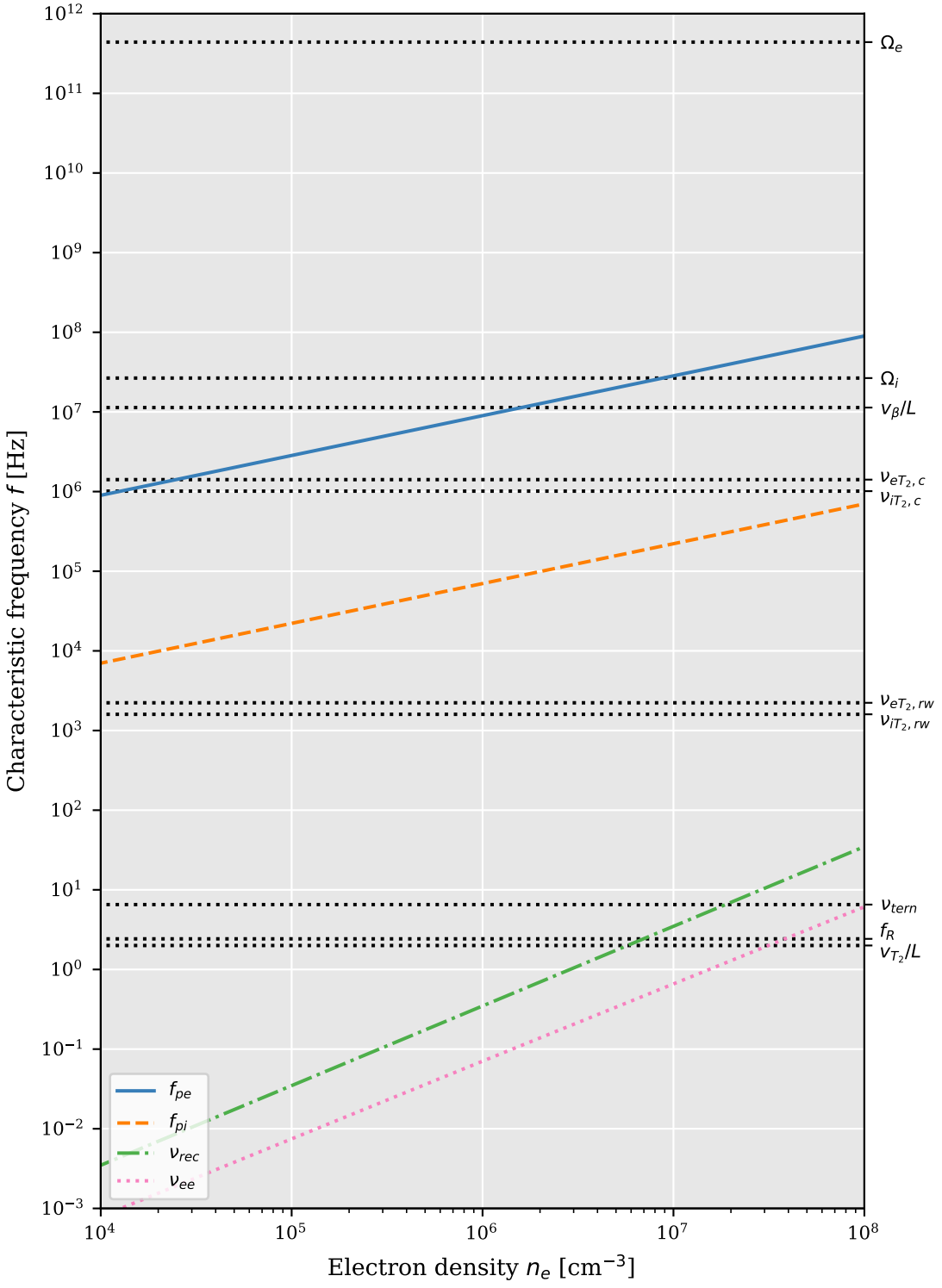

Figure 3.4.: Characteristic time scales. f_{pe}: electron plasma frequency, f_{pe}: ion plasma frequency, ν_{rec}: collision rate of recombination, ν_{ee}: Coulomb collision rate, Ω_e: electron gyro frequency, Ω_i: ion gyro frequency, $\nu_{e,rw}/\nu_{i,rw}$: elastic collision freuqency of electrons/ions in front of the rear wall, $\nu_{e,c}/\nu_{i,c}$: elastic collision freuqency of electrons/ions in the center of the source, f_R: synchrotron loss frequency, ν_{tern}: ternary association rate, v_{T_2}/L: mean inverse time of neutrals in the source, v_β/L: mean inverse time of betas in the source. Neutral density: in front of rear wall $1 \times 10^{12}\,\mathrm{cm}^{-3}$, in center $6.3 \times 10^{14}\,\mathrm{cm}^{-3}$. Magnetic field: 2.5 T. Temperature: 80 K.

3.4. KATRIN Plasma Models

In general it is not possible to solve all equations of movement for all particles in a plasma directly due to the large number of particles and the unknown starting conditions. Thus statistical methods need to be employed. Additionally if the density of particles is large enough direct particle interactions will need to be taken into account. [13]

The evolution of a particle system can be described by the Liouville distribution function F. It states the probability that a specific particle can be found at a certain space, time and velocity, while all other particles will be found at another certain space and velocity. The temporal evolution of the distribution function can then in theory be calculated by the Liouvill equation. In parxis the equation can not be solved because of the vast amount of parameters. The amount of parameters can be reduced by assuming that there are only binary collisions without an external field and that the interaction range of the collisions is small. Thus the distribution function F can be split into individual distribution functions f_i for each specie i. The evolution of the individual distribution functions is in this case given by the Boltzmann equation

$$\frac{\partial f_i}{\partial t} + \frac{\mathbf{p_i}}{m_i} \cdot \nabla f_i + \mathbf{F} \cdot \frac{\partial f_i}{\partial \mathbf{p_i}} = \left(\frac{\partial f_i}{\partial t}\right)_{\text{coll.}}, \tag{3.26}$$

with the momentum $\mathbf{p}_i$, mass m_i and the force $\mathbf{F}$ acting on the particles. Collisions of particles are expressed in the collision term

$$\left(\frac{\partial f}{\partial t}\right)_{\text{coll.}} = \sum_{j=1}^{n} \iint g_{ij} I_{ij}(g_{ij}, \Omega)[f_i' f_j' - f_i f_j] \mathrm{d}\Omega \mathrm{d}^3\mathbf{p}' \tag{3.27}$$

with distribution functions f before the collision and f' after the collision, g_{ij} the magnitude of the relative momenta for the two interacting particles, $I_{ij}(g_{ij}, \Omega)$ the differential cross section and Ω the solid angle. [39] The force $\mathbf{F}$ comprises all forces acting on the particles. In the case of the KATRIN plasma gravitational forces can be neglected and the force is given by the Coulomb force $\mathbf{F}_c(E, B)$. The magnetic and eletric fields are determined by the particle motion through Maxwell's equations. Thus the field in the KATRIN source can be determined by solving the Boltzmann equation in conjunction with Maxwell's equations.

The solution of the Boltzmann equation depends on the specific assumption on the plasma particles, especially the behavior of collisions. The KATRIN plasma has the peculiar property that electron interactions are frequent enough that they can not be neglected but the collisions are too infrequent that the plasma can be fully described through a fluid ansatz, see section 3.2. Additionally the collision properties vary over the length of the beam tube, as the density of the neutral particles varies.

In a previous atempt to calculate the potential in the source by Kuckert [37] she assumed that the electrons and ions can be treated as a fluid for the central part of the source. The underlying model is shown with a short insight into the results in section 3.4.1.

The approach of Kuckert overestimates the collisions of the electrons in the center of the WGTS but is certainly not valid for the region close to the rear wall. There is no conclusive result if the description of the plasma in the central region can be decoupled from the description of the plasma close to the rear wall. Thus in the context of this thesis a new approach is developed, where the electrons are treated partly collisional and partly non collisional over the whole length of the beam tube. The resulting model and simulation strategy is shown in section 3.4.2

3.4.1. Drift-Diffusion Model

In a previous work Kuckert [37] assumed that electrons and ions can be described as a fluid and that the velocity distribution of electrons and ions follow the Maxwell-Boltzmann distribution. Thus the distribution function of each specie can be described by its temperature T and its density $n_i(\mathbf{x})$. The zeroth moment of the Boltzmann equation, the species continuity equation then reads

$$\frac{\partial n_i}{\partial t} + \nabla \Gamma_i - R_i = 0\,, \tag{3.28}$$

where Γ_i is the particle flux density and R_i the chemical production of the specie i. The chemical production is evaluated via the Boltzmann collision integral. In the case of thermal particles the integral can be performed resulting in a convolution of the cross section with the Maxwell-Boltzmann distribution. Kuckert derived the production coefficent R not through integration but through an evaluation of rate equations of electron, ion and neutral paricle interactions from literature.

The particle flux density is then linked to the electric potential U through Poisson's equation and the current continuity equation. The electron flux density is modeled here by using the drift-diffusion approximation through the electron mobility μ_e and the diffusion constant D_e:

$$\Gamma_e = -D_e \nabla n_e - \mu_e n_e \left(\nabla U - \frac{k_B}{e} \nabla T_e \right) \tag{3.29}$$

It states that the flux can be solely described by the diffusion of the electron density, the thermal flux and a collective movement movement of electrons in an electric potential. Kuckert assumed that the diffusion coefficient follows the classical diffusion described in [14] and that the mobility can be linked to thourgh the Einstein relation [39].

Kuckert used the software framework COMSOL to obtain solution of the coupled differential equations. The software uses the finite element method to solve the underlying equations. Kuckert assumed that there exists a time independend solution, such that after a long time the densities and currents of the particles reach a steady state.

The simulated geometry of Kuckert was assumed to be an cylinder with a length of 10 m and a radius of 4.5 cm. This corresponds to the central tube of the WGTS. The boundaries were choses, such that the cylinder walls and the left end cap absorb all incoming charged particles. The right end cap was assumed to reflect electrons, while ions are absorbed. The electric potential of the tube wall and the right cap was set to zero, while the potential of the left cap could be adjusted to mimic the potential of the rear wall.

An exemplary potential map of Kuckert can be found in figure 3.5. Here the temperature of the particles was set to 30 K, the density of neutral particles was set to $0.8 \times 10^{21}\,\mathrm{cm}^{-3}$ and the rear wall potential was set to zero. It was found that the electron density reaches a maximum value of approximately $3 \times 10^{6}\,\mathrm{cm}^{-3}$ and the potential reaches values of up to 12 mV. The density as well as the potential show a strong dependence along the length of the tube. In radial direction the potential increases from half its maximum value to its maxmimum and then drops at the last few milimeters to zero.

Kuckert investigated the properties of the potential in dependence on the column density, the temperature of the electrons, the magnetic field and the rate coefficient of recombination of electrons and ions. She found that the potential distribution does not change significantly through a variation of these parameters. The specific results can be found in her thesis [37].

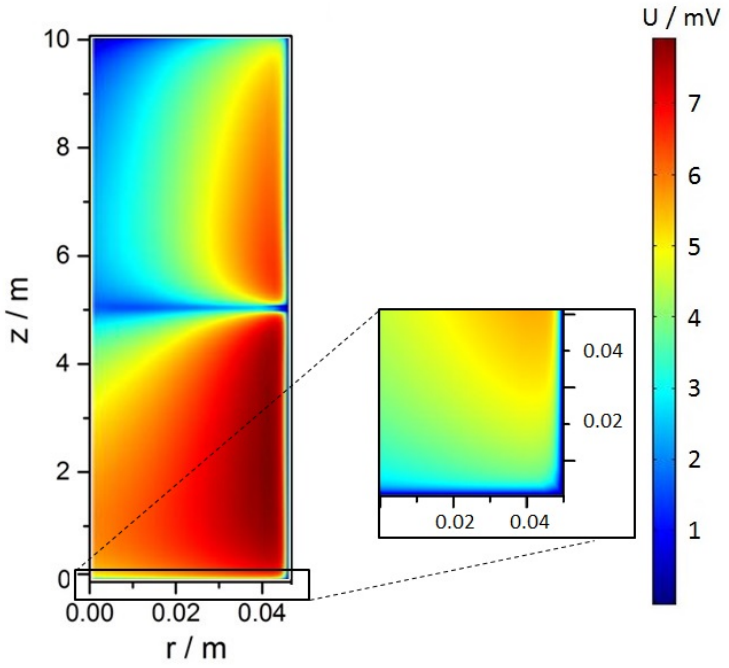

Figure 3.5.: Potential map of Drift-Diffusion Model Simulated using the software framework COMSOL in the center of the source. Figure taken from [37].

3.4.2. Partly Collisional Vlasov Model - Scope of this Thesis

Vlasov Model and Simulation

Assume that there are no collisions in the plasma. This means that the collision term in the Boltzmann equation, equation 3.26 is set to zero. The resulting equation is called Vlasov equation and reads

$$\frac{\partial f_i}{\partial t} + \frac{\mathbf{p_i}}{m_i} \cdot \nabla f_i + \mathbf{F} \cdot \frac{\partial f_i}{\partial \mathbf{p_i}} = 0\,. \tag{3.30}$$

This means that the distribution of two particle species is linked only via the Coulomb force. The Coulomb force is calculated through the eletric and magnetic field. These fields are calculated using Maxwell's equations, which in turn are effected by the charged particle current j. The current can be split into a contribution of electrons j_e and a contribution of ions j_i. Thus the distribution of the electrons is dependent on the ion current and vise versa.

Electron and ion currents show different temporal characteristic because of the large mass difference. The electron current changes much faster than the ion current. So when considering the electron movement on small time scales the ion current can be assumed to be constant. The resulting eletric field from the electron movement then influences the ion movement and thus changing the ion current on a large time scale. Again this influences the electron movement and the cycle starts again.

The large difference of time scales makes in general a simulation of both particle species at the same time unfeasible. A possible ansatz for the simulation can be an iterative approach, where the electron movement is simulated with a fixed ion current alternating with a simulation of the ion movement in a mean electric field. After a number of cycles it is assumed that the resulting distribution functions reach a steady state. The result of such a simulation is of course dependent on the inital distributions.

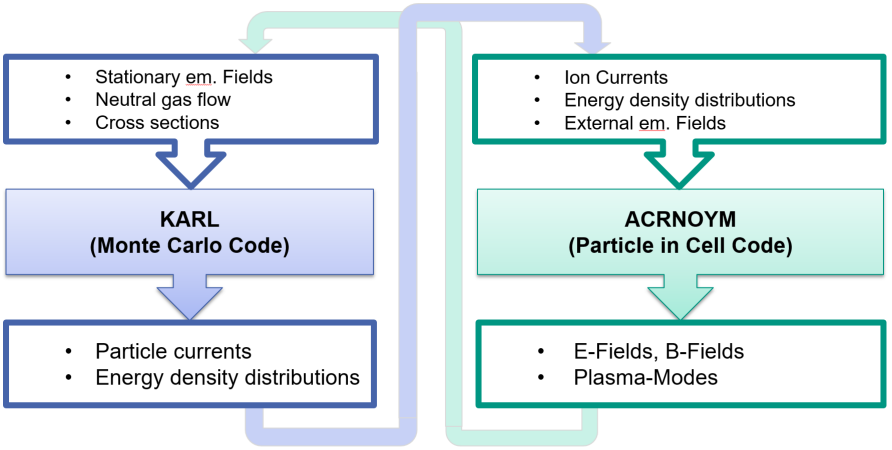

Figure 3.6.: Simulation strategy The particle densities and particle currents are simulated in a Monte Carlo Code (KARL) and used as an input for kinetic simulations of the electrons in a particle in cell code (ACRONYM). The resulting electromagnetic fields are used as an input for the Monte Carlo simulations.

Partly Collisional Simulation

Now consider that there are collisions. In the KATRIN source they occure for electrons on larger length scales than the Debye length. The difference of the length scales are larger close to the rear wall and smaller in the center of the WGTS. Whereas collisions of ions occure on a smaller length scale than the Debye length in the center of the WGTS and on smaller length scales closer to the rear wall. See section 3.2.3 for more informations.

Thus both electrons and ions can be considered collisionless close to the rear wall. It is viable to use a Vlasov model here. In the center of the WGTS electrons and ions can be considered partly collisonal. The movement of electrons and ions is influenced by collisions but the collisons occure on such small length scales that the distribution of the electrons and ions are not soleley influenced by the collisions.

In the scope of this thesis it is assumed that the electric fields are manly moderated by electrons while ions only contribute by their constant current. Thus electrons can be simulated seperately from ions. A iterative ansatz is proposed. First the electron distribution and the electromagentic fields are simulated with a constant ion current. Then the ions are simulated with collisions in the electromagentic field produced by the electrons. The ion current is then used to start a new cycle of electron simulations. The electron simulation depends on the inital distribution of the electrons. These distributions are also simulated, while simulating the ion movement. Thus collisions of both electrons and ions are taken into account. This simulation strategy is also depicted in figure 3.6.

The determination of the electron distribution functions and the electromagentic fields will be simulated using the well tested ACRONYM code [32], see also chapter 5 for more information. Here the Vlasov equation is solved numerically with the usage of a particle in cell method.

The simulation of the ions and electrons in a stationary electric field with particle collisions will be performed with a newly developed code, called KARL. This code utilizes a Monte Carlo approach of particle generation, movement and collisions within self generated particle densities. For more information on the KARL code please refer to chapter 4.

Scope of this Thesis

In the scope of this thesis two major tasks needed to be accoplished. First the KARL code needed to be designed and tested. The necessary tasks can be summarized by the following list:

- develope a simulation strategy for the Monte Carlo approach, including interactions of electrons and ions
- determine the relevant interactions of electrons and ions in the KATRIN source
- incorporate electromagentic fields from the ACRONYM simulation in the particle movement
- provide a suitable output of the particle currents and particle distributions
- find suitable tests to ensure the correctnes of the simulation

Secondly the ACRONYM code needed to be adapted to incorporate also the specific conditions of the KATRIN source. The necessary tasks are summarized by the following list.

- include circular boundary conditions for particle movement and electromagentic field calculations to mimic the KATRIN geometry
- include position dependent background electric fields to include surface potentials and charging of the rear wall
- include position dependent background ion currents to provide a link to the output of the simulation with the KARL code
- include a space dependent inital arbitrary energy density distribution of electrons to provide a linke to the output of the simulation with the KARL code
- include electron generation through beta decay and ionization to mimic the generation of electrons during the simulated time
- include particle injection at the simulation boundaries
- find suitable tests to ensure the correctnes of the simulation

Chapter 4
Simulation of Particle Distributions with KARL

The density and its energy distribution of all species defines the plasma in the KATRIN source. The specific density distribution is dependent on the cross section of each interaction, the particle movement and the geometry of the source. Initially only beta electrons are created. Subsequent interactions with the surrounding gas create multiple other electrons and ions with varriing energy. This scenario ist best simulated using the Monte Carlo technique. This technique was implemented in the newly developed KAtrin WGTS electon and ion spectrum monte CaRLo (KARL) code. The code was developed in collaboration with C. Reiling in his master thesis [52] and extended together with Rupp in his master thesis **[Cite: MA Joachim]**. The code and its first results will be presented in this chapter. **ToDo**

4.1. Simulation Method

The KARL code uses a special approach of the Monte Carlo technique. Each paritcle chain starts at the beta decay, where the position of the new electron (and ion) is sampeled from the neutral particle denisty distribution, see section 2.3.1.1. The energy is sampeled from the known Fermi spectrum of the beta decay, see section 2.1. The beta decay particles are then added to the particle queue and the simulation starts its iterative cycle, see figure 4.1. In each iteration step a particle is selected randomly from the particle queue. Then the mean free path is determined from the interacting partner density at the position of the particle and the energy of the particle. The particle is then moved according to the mean free path and the electromagnetic fields to a new position, see section 4.1.3. If the particle hits the simulation boundaries it will be deleted. Otherwise a interaction is selected randomly from the available interactions, see section 4.1.4. The interaction products are then added to the particle queue and the iteration starts from the beginning. The particle loop is repeated until there are no more particles in the particle queue. Then a new beta decay particles are created and processed until the specified targed decay number is reached.

The KATRIN source tube is approximated by a cylinder with an open end. Electrons are reflected at this end, which corresponds to the reflection of electrons at the DPS dipole electrodes or at the main spectrometer potential. All ions are removed at the DPS side. All other boundaries of the cylinder are considered perfectly electric conductors. Thus all particles hitting the cylinder walls will be removed from the simulation.

The simulation is evaluated using two methods: virtual current borders and density fields, which provide energy dependend particle currents and particle densities in relation on the position in the source. They will be discussed in the following.

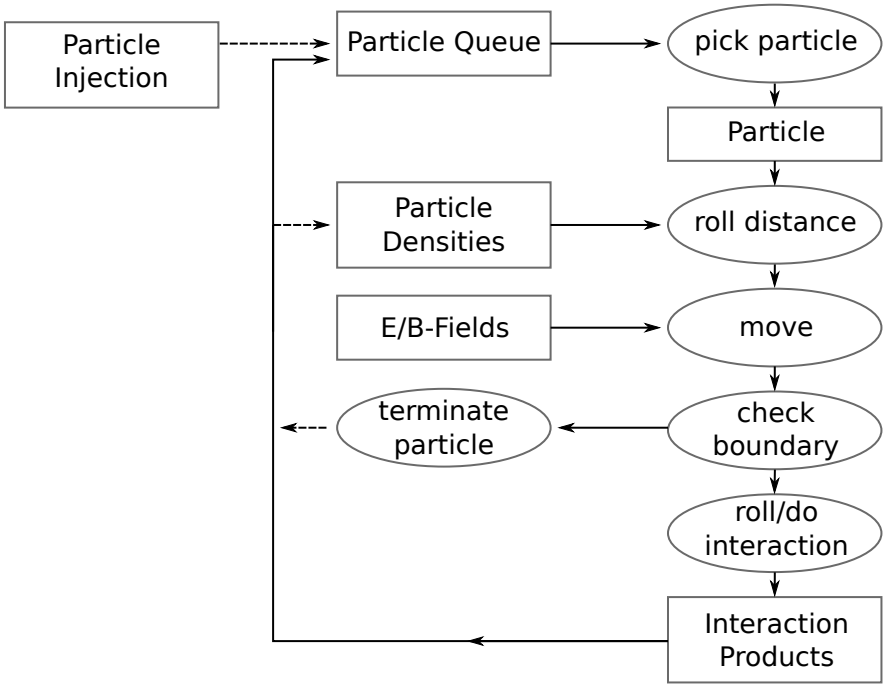

Figure 4.1.: KARL Simulation procedure. Beta electrons are injected to the particle queue. A particle is picked from the queue and processed. The iteration step either ends in an particle interaction or through termination at the simulation boundaries. The particle queue is processed until no particle is in the queue and a new beta particle is injected. The particle densities are determined during the simulation.

4.1.1. Virtual Current Borders

In the simulation the source is segmented longitudinally, radially and azimutally. Each particle is registered, when it crosses from one segment to another. The total current through the segment faces is then given by

$$j = \frac{N^+ - N^-}{AT}\,, \tag{4.1}$$

where N^+ and N^- is the number of particles crossing the faces in positive and negative direction, A is the area of the face and T the simulated time. The simulated time is determined by the number of decays N_β, which were simulated and the total activity a of the source

$$T = \frac{N_\beta}{a}\,. \tag{4.2}$$

The current through the faces can be determined depending on the energy and type of species crossing the faces. Thus the simulation can provide an energy and position dependend particle current in the KATRIN source.

4.1.2. Density Fields

The segmentation of the source is also used in the determination of the individual particle densities. During the simulatio it is recorded how long a particle stays in one segment. The density of a species α is then proportional to the total time of all particles of the specie spend in the segment and the volume V of the segment

$$n_\alpha = \frac{\sum_i t_i}{TV}\,. \tag{4.3}$$

This equation is only valid for a simulation with particles, which do not recombine with each other. In case of recombination an additional term has to be added corresponding to the number of recombinations of the recombination partner γ in the segment

$$n_\alpha = \frac{\sum_i t_i}{TV} - \frac{N_\gamma}{V} \,. \tag{4.4}$$

Again the density can be determined depending on the energy and type of specie. Thus the simulation can provide an energy and position dependend particle density of the KATRIN source.

4.1.3. Particle Movement

The particle movement is a central part of the simulation. Particles are moved from an original position to a new position depending on the mean free path and the electromagentic fields in the source. The movement of the particle can be performed in the code using the Boris push algorithm or through the drift approximation algorithm. The former can be used in arbitrary electromagnetic fields and resolves also the gyro motion of the particle. In the latter the motion of the particle is compound by a motion of the guiding center and the circular gyro motion around this guiding center. The Boris push algorithm provides highly accurate results at the cost of computing time. Both algorithms can be used by the KARL code but in most simulations only the drift approximation algorithm is used to conserve computing time. Therefore the drift approximation algorithm will be presented here. The Boris push algorithm is also used by the ACRONYM code and will be therefore discussed in section 5.1.3.

Drift Approximation Algorithm

In the drift approximation algorithm the movement of the particle is described by the superposition of the movement of the guiding center and the gyro motion of the particle around the guiding center. It is only applicable to time and spatial constant magnetic fields. In the context of the KARL simulation it is assumed that the magnetic field is constant over the whole source. Thus the drfit approximation algorithm can be used.

The particle is moved in total by the distance L, which is determined by the mean free path, see below. Nevertheless the movement of the particle is subdivided into small spatial steps Δx. The step size is chosen by the step size of the electromagnetic field data, to avoid movement across multiple eletric field cells. The discretization of the spatial dimension can be translated into a discretization of the time domain to

$$\Delta t = \frac{\Delta x}{|\mathbf{v}^i|} \,, \tag{4.5}$$

where $|\mathbf{v}|$ is the absoltue velocity of the particle before movement. The position z in longitudinal direction then is calculated by

$$z^{i+1} = z^i + v_\parallel^i \Delta t \,, \tag{4.6}$$

where the index i denotes the timestep at which the quantity is given and $v_\parallel^i$ is the velocity of the particle perpendicular to the magnetic field. The electric during the motion is approximated by the mean of the field value at the original position and at the new position

$$\mathbf{E} = \frac{\mathbf{E}(z^{i+1}) + \mathbf{E}(z^i)}{2} \,. \tag{4.7}$$

This field is then used to calculate the movement perpendicular to the magnetic field and used to determine the new velocity $v_{\parallel}^{i+1}$. The perpendicular particle position changes to

$$x^{i+1} = x^i + v_{\perp,x}\Delta t \tag{4.8}$$
$$y^{i+1} = y^i + v_{\perp,y}\Delta t\,, \tag{4.9}$$

where $v_\perp$ is given by

$$v_\perp = \frac{\mathbf{E}\times\mathbf{B}}{B^2}\,. \tag{4.10}$$

The parallel velocity changes corresponding to the Lorentz force to

$$v_{\parallel}^{i+1} = v_{\parallel}^{i} + \frac{qE_{\parallel}}{m}\Delta t\,, \tag{4.11}$$

where $E_\parallel$ is the electric field strength parallel to the magnetic field, m is the mass of the particle and q its charge.

Travelled Distance

The actual travelled distance L is determined through a random number $\eta \in (0,1)$ and the mean free path λ

$$L = -\lambda \cdot \log\eta\,, \tag{4.12}$$

which is the inverse of equation 3.13. The mean free path is determined through equation 2.54 depending on the cross section of the interaction and density of the target particles. The mean free path of multiple competing interaciton channels i is given by

$$\lambda = \frac{1}{\sum_i \sigma_i n_i}\,, \tag{4.13}$$

where σ_i is the cross section and n_i the density of the target particles. The cross section is dependend on the energy of the incidend E_i and target particle E_t. The transformation into the target frame is dependent on the incident angle θ of the interaction and its distribution $f(\theta)$. Thus each contribution to the mean free path is written as

$$\sigma_i n_i = \frac{1}{\pi}\iint dE_t\, d\theta\, f(\theta)\sigma_i(E_t, E_i, \theta)\frac{dn_t}{dE_t}(E_t)\,. \tag{4.14}$$

In the simulation it assumed that the incident angle is isotropically distributed to reduce calculation effort. Further more small and large incident angles are neglected. The transformation to the target frame can result otherwise in a vanishing energy, which in turn would result in an overestimation of the cross section toward lower energies. The energy distribution of the target density is collected in discrete bins. Thus the integral is not performed directly but replaced through a sum over all possible energy bins.

4.1.4. Particle Interactions

Four different particles species can be distinguished in the simulation: electrons e^-, tritium ions T^+, tritium molecule ions ${T_2}^+$ and tritium cluster ions ${T_3}^+$. Higher order cluster ions can in principle be used as well but are not used in the current version of the code because of missing cross section data. Furthermore it can be assumed from rate constant measurement, see section 2.4, that the density of higher order clusters is significantly lower than the density of ${T_3}^+$. Thus the impact of these ions on the simulation results should be small.

Each of the particle species have multiple different interaction channels, see section 2.4. The specific interaction channel at each interaction point in the simulation is determined randomly, corresponding to the probability of the interaction channel. A measure for the the probability that a specific channel is chosen is given by the inverse mean free path of the channel. The higher the inverse the higher the probability of that interaction. In the code a random number η is drawn from the interval $[0, \sum_i \sigma_i, n_i]$, where i denotes the different interaction channel. A specific interaction channel j is used, where

$$\eta \geq \sum_{i}^{j} \sigma_i n_i \tag{4.15}$$

is fullfilled.

4.1.4.1. Elastic Scattering

Elastic scattering is the dominant interaction channel for all particle species. In the interaction the velocity changes its direction but not its absolute value. The interaction can therefore be described by a rotation in direction of the velocity. The rotation is characterized in spherical coordinates by the azimutal angle θ and polar ange ϕ. The angle θ is given by the differentical cross section $\frac{d\sigma}{d\theta}$. The differential cross section is dependend on the particle type and energy. Isotropic scattering is assumed for all ion interactions and for electrons below 10 eV. The azimutal angle at higher energies is sampeled from the differential cross section using the ELSEPA code [53]. Large and small scattering angles are surpressed in this case. The polar angle is sampled from a uniform distribution in the interval $[0, 2\pi)$. This represents the polar symmetry of the interaction.

In the code the new velocity vector is derived through the following procedure:

- Roll the energy of the target particle from the density field at the position of the interacting particle.
- Convert the target particle to a velocity vector (isotropic distribution with an additive drift velocity).
- Transform the velocity of the primary particle of to the center of mass frame.
- Roll azimutal angle θ and roll polar angle ϕ.
- Rotate the primary velocity in the center of mass frame.
- Transfrom the velocity back to the laboratory frame.

The rotation of the velocity is performed using the procedure provided by Haghighat [25]. The procedure is shortly summarized in the following: The inital velocity can be expressed by

$$\mathbf{v} = v_x \mathbf{e_x} + v_y \mathbf{e_y} + v_z \mathbf{e_z} = |\mathbf{v}|(n_x \mathbf{e_x} + n_y \mathbf{e_y} + n_z \mathbf{e_z})\,. \tag{4.16}$$

The unit vector $\mathbf{n}$ is then transformed to a new basis, where the new z axis is aligned with the unit vector. The new eigenvectors are

$$\mathbf{e'_x} = \mathbf{e'_y} \times \mathbf{e'_z} \tag{4.17}$$

$$\mathbf{e'_y} = \frac{\mathbf{n} \times \mathbf{e_z}}{|\mathbf{n} \times \mathbf{e_z}|} \tag{4.18}$$

$$\mathbf{e'_z} = \mathbf{n}\,. \tag{4.19}$$

In this new base the rotation can be performed trivially through

$$\mathbf{n'} = \sin\theta\cos\phi\,\mathbf{e'_x} \sin\theta\sin\phi\,\mathbf{e'_y} + \cos\theta\,\mathbf{e'_z}\,, \tag{4.20}$$

where $\mathbf{n}'$ is the rotated unit vector. The reverse basis change then results in

$$\mathbf{n}' = n'_x \mathbf{e_x} + n'_y \mathbf{e_y} + n'_z \mathbf{e_z} \tag{4.21}$$

with

$$n'_x = -\left(\frac{n_x n_z}{\sqrt{n_x^2 + n_y^2}} \cos\phi + \frac{n_y}{\sqrt{n_x^2 + n_y^2 \sin\phi}} \right) \sin\theta + n_x \cos\theta \tag{4.22}$$

$$n'_y = -\left(\frac{n_y n_z}{\sqrt{n_x^2 + n_y^2}} \cos\phi - \frac{n_x}{\sqrt{n_x^2 + n_y^2 \sin\phi}} \right) \sin\theta + n_y \cos\theta \tag{4.23}$$

$$n'_z = \sqrt{n_x^2 + n_y^2} \cos\phi \sin\theta + n_z \cos\theta \,. \tag{4.24}$$

The new velocity vector in the original base is finally given by

$$\mathbf{v}' = \mathbf{n}'|\mathbf{v}| \,. \tag{4.25}$$

The position of the primary target does not change through elastic scattering. Nevertheless the guiding center of the movement changes its position in the interaction. Thus this change of the guiding center has to be reflected in the simulation. If the particles are moved by the Boris push algorithm, see section 4.1.3 this effect is allready included because the algorithm resolves each gyro motion of the particle. If the particle movement is desribed by the drift approximation algorithm an additional change of the guiding center has to be added. Assume that the guiding center is located at the position $\mathbf{x}$. The new position of the guiding center $\mathbf{x}'$ is shifted by the length Δx with

$$\Delta x = 2 r_L \cos\theta \,, \tag{4.26}$$

where r_L is the gyro radius and θ the scattering angle, see figure 4.2. The direction of the shift is in general dependent on the polar angle ϕ of the gyration. It is assumed that there are many gyro motions between interactions, see section3.2.6. Thus the polar angle is determined randomly before the interaction from a random number $\eta \in [0, 2\pi)$. The new position is then given by

$$\mathbf{x}' = (x + \Delta x \sin 2\pi\eta)\, \mathbf{e_x} + (y + \Delta x \cos 2\pi\eta)\, \mathbf{e_y} + z\, \mathbf{e_z} \tag{4.27}$$

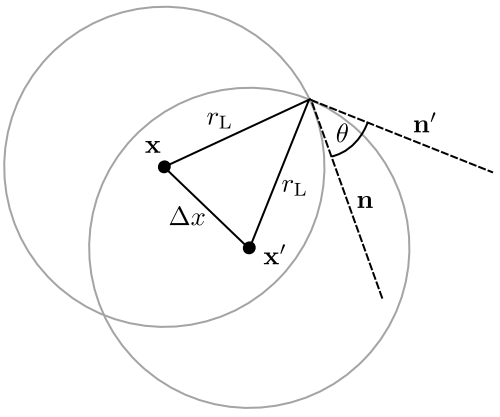

Figure 4.2.: Guiding center change

4.1.4.2. Electron Impact Ionization

In the ionization process an electron hits a neutral gas particle and creates another electron and an ion molecule (T_2^+). This ion molecule can be stable or it can disocitate spontaneously to T^+. The cross section and thershold energy depends on the type of ionization process. Janev *et al.* identified three different ionization channels [29]. These channels are incorporated in the code. Kim and Rudd developed another effective model for the ionization process [33]. The created ion in this case is considered stable. This model can also be used in the code.

There is a thershold for the reaction at the ionization energy. The remaining collision energy T has to be devided between both electrons. In the code the ion is assumed to have the same energy and velocity direction as the neutral gas particle, due to the large mass difference. The energy of the primary electron E_p is sampled from the theoretical works of Rudd and Kim [33]. The energy of the secondary electron follows directly from the energy of the pramary and the collision energy ($E_s = T - E_p$). The scattering angles of the primary and the secondary electron are sampeled from the semi emperical studies by Grosswendt and Waibel [24]. The polar angle ϕ_p of the primary electron is assumed to be uniformly distributed, while the polar angle of the secondary electron is given by $\phi_p - \pi$. The azimutal angle range of the primary electron is dependent on the energy. For small energies ($< 100\,\text{eV}$) it can be assumed that the angle is uniformly distributed between 0 and $\pi/4$. Similarly the azimutal angle range of the secondary is dependent on the energy. For small energies ($< 50\,\text{eV}$) it can be assumed that the angle is uniformly distributed between 0 and π.

4.1.4.3. Electron Impact Excitation

Electrons can among others excite electrons of neutral gas particles, vibrational and rotational states of the gas, see section 2.4. The excitation depends on the inital state of the neutral gas molecule. In the code different excitation states differ in their cross section and the energy loss. It can be destinguished between

- the 15 excitation channels of electronic excitation measured by Janev *et al.* [29].
- the experimental cross section of electronic excitation measured by Yoon *et al.* [59]
- the first two vibrational excitations measured by Janev *et al.* [29].
- the experimental cross section of vibrational excitation measured by Yoon *et al.* [59]
- the first rotational excitation excitation measurey by Janev *et al.* [29]

The interaction process itself is reduced to an energy loss of the electron. The motion of direction is assumed to stay constant.

4.1.4.4. Recombination

Recombination processes between ions and electrons need special treatment in the code. The particles interacted, in all processes before, with the neutral gas particles. The reservoir of neutral particles is considerd to be infinite, such that the interactions of electrons and ions with the gas do not change the gas flow and its properties. This is no longer valid for recombination. Each time an electron recombines not only the electron density needs to be reduced but also the ion density. Thus each event in the Monte Carlo algorithm is no longer independend from the others. Direct interactions of the particles is not possible in a Monte Carlo algorithm. In KARL this discrepancy is resolved through the density fields presented in section 4.1.2. Each time an electron recombines with an ion, the electron is deleted from the particle queue and a special counter in the corresponding ion bin is

increased. The corresponding bin is sampeled from the density distribution of the ion. Thus the electron can no longer travel the source and can no longer contribute to the density. The ion density is reduced by the counter. In total both species have reduced densities without direct interaction. The same procedure is applied, when the primary particle is the ion. In this case the ion will be deleted and the corresponding counter of the electron is increased. In the limit of many interactions both electron recombinations and ion recombination will show the same total number of recombinations.

In the code only T_2^+ and T_3^+ ions recombine, while T^+ ions do not due to the small cross section. The cross section of T_2^+ and T_3^+ ions is evaluated from the formula provided by Janev *et al.* [29].

4.1.4.5. Ion Cluster Formation

Ions can form clusters through attachement of molecules to the existing ion, see section 2.4. The cross section of the interaction depends on the inital cluster size. In the code three different cluster sizes are distinguished: T^+, T_2^+ and T_3^+. Higher order clusters are neglected here, due to their predicted low density and missing cross section data for fragmentation processes.

In the code the cross section for T^+ ions is cacluated from rate coefficient measurement of radiative and ternary association [50]. The new T_3^+ ion of this reaction is initalized with the same velocity and position as the inital T^+ ion, due to missing information on the differential cross section.

T_2^+ ions show a large cross section for cluster formation, see section 2.4. The cross section of the reaction is taken from the works of Janev *et al.*. Again the volocity and position of the new ion is initialized from the velocity and position of the initial T_2^+ ions, due to missing information on the differential cross section.

4.1.4.6. Ion Charge Transfer

Ion molecules (T_2^+) do not scatter elastically from neutral gas but take part in charge transfer reaction, see section 2.4. One electron of the target neutral gas molecule is transfered to the ion. Thus a new ion is created. The cross section of this reaction is given by Janev *et al.* [29]. The velocity direction of the new ion is calculated from the velocity of the inital ion, the scattering angles ϕ and θ and the velocity of the target molecule, see section 4.1.4.1. The angles are sampeled from the intervals $\phi \in [0, 2\pi)$ and $\theta \in [0, \pi)$. The velocity of the target molecule is sampeled from the velocity distribution of the neutral gas particles. Thus the ion charge transfer reaction is similar to elastic scattering of the other ion species.

4.2. Electromagnetic Field-Free Simulation

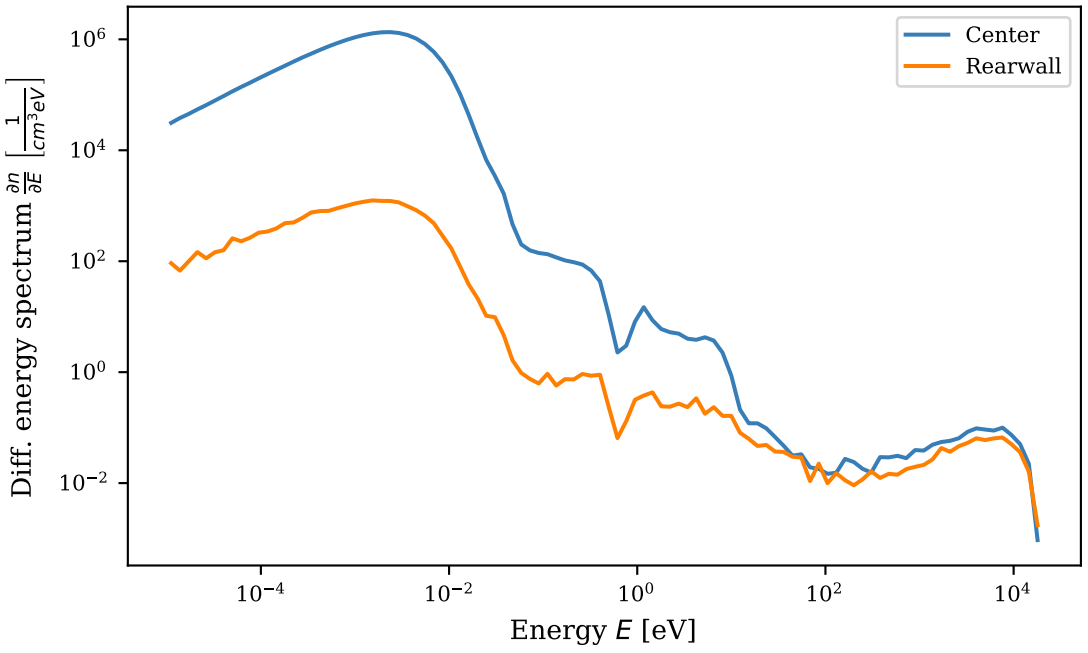

Figure 4.3.: Density distribution

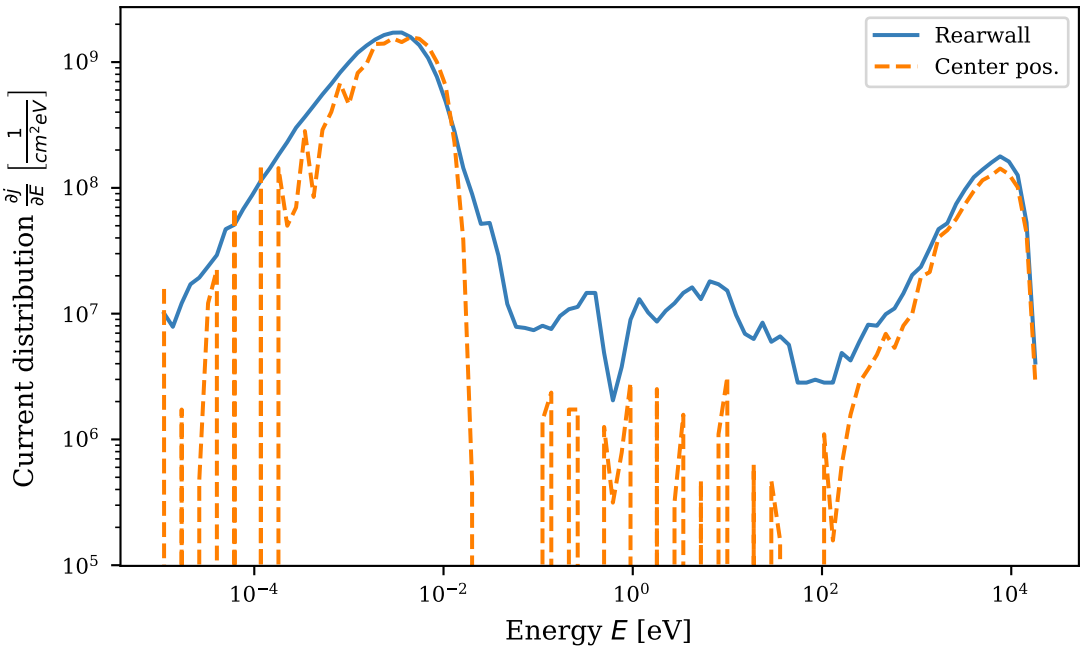

Figure 4.4.: current distribution

4.3. Conclusion

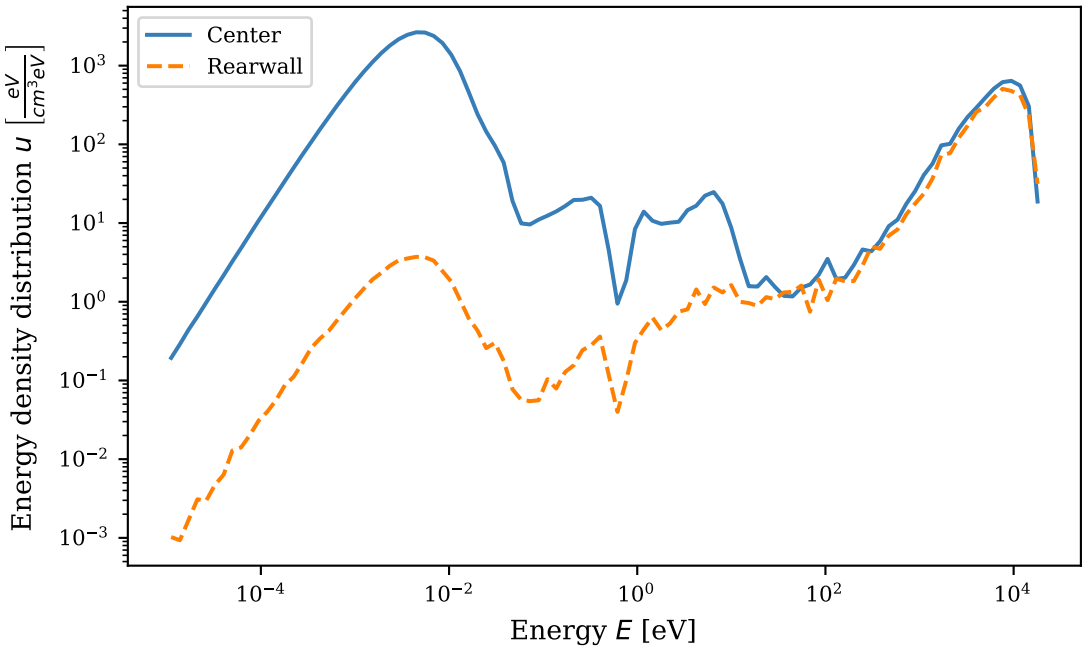

Figure 4.5.: Energy density distribution

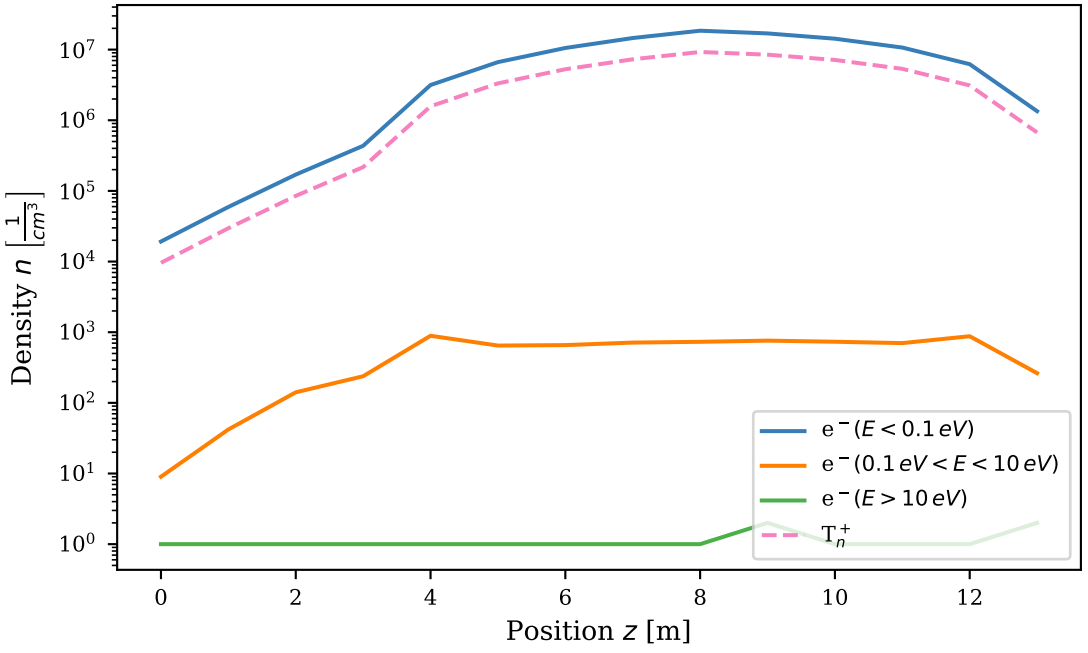

Figure 4.6.: Density in z

Chapter 5
Particle in Cell Simulations with ACRONYM

5.1. The Particle in Cell Method

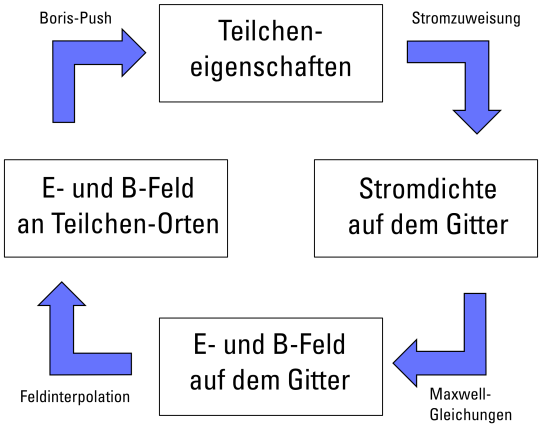

Figure 5.1.: PIC scheme

5.1.1. Grids for Currents and Fields

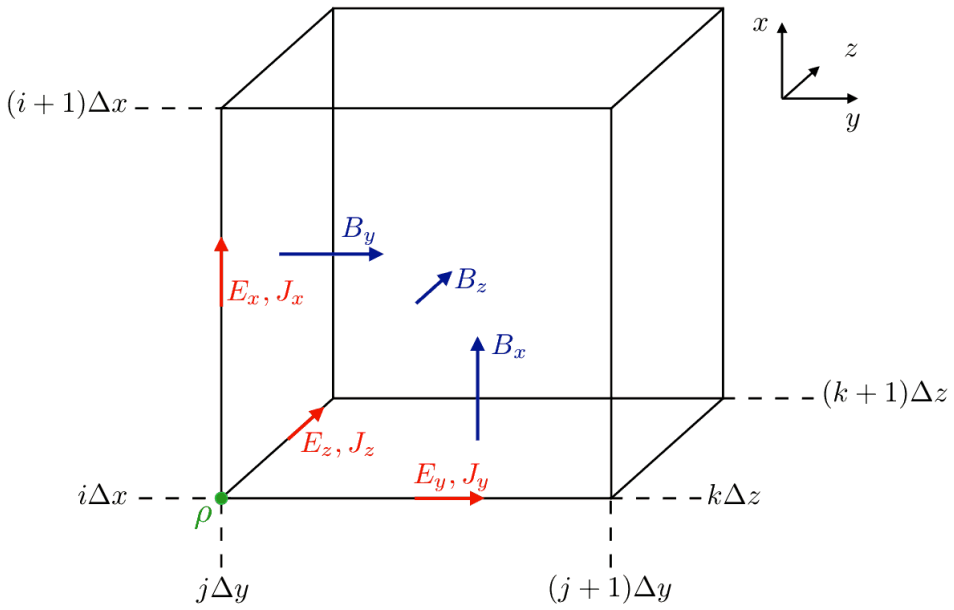

Figure 5.2.: Yee lattice

5.1.2. Macro Particles

5.1.3. Particle Movement

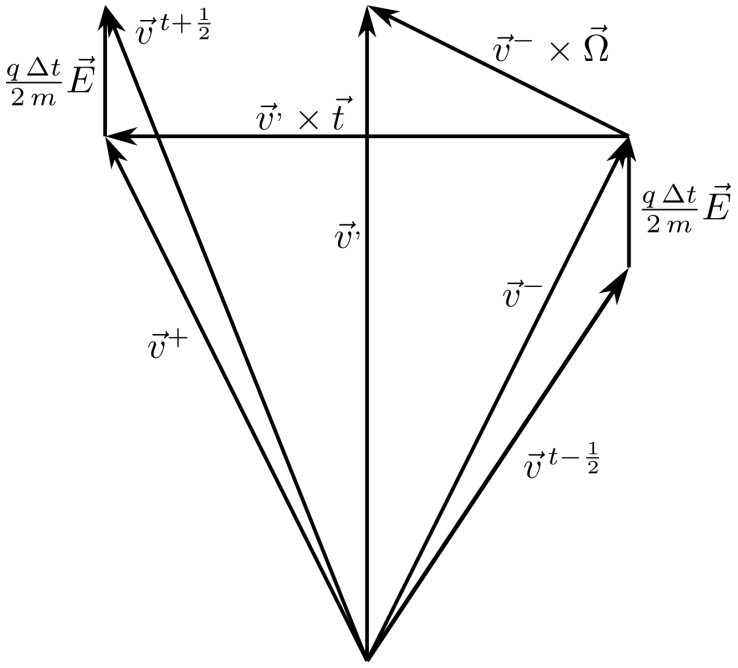

Figure 5.3.: Boris push

5.1.4. Current Deposition

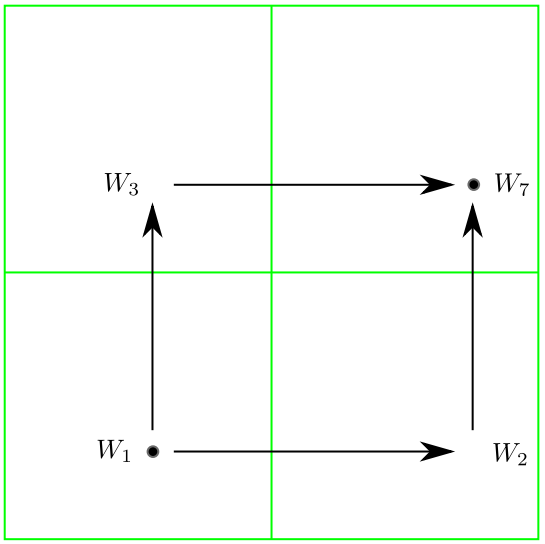

Figure 5.4.: Current deposition

5.1.5. Maxwell Solver

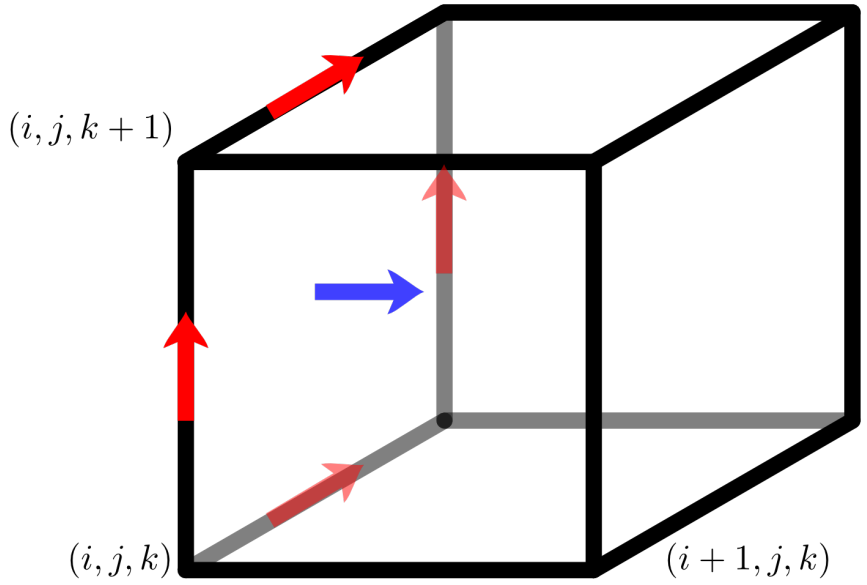

Figure 5.5.: Maxwell solver

5.2. Boundary Conditions

5.2.1. Perfect Electrical Conductor

[Sketch of handling of half cut cells and cells at borders] ToDo

5.2.2. Periodic Boundary Condition

5.2.3. Perfectly Matched Layer

5.3. Background Fields and Currents

5.4. Particle Injection

5.4.1. Injection Methods

5.4.1.1. Constant Density

5.4.1.2. Constant Current

5.4.1.3. Constant Decay Rate

5.4.2. Injection at PML boundary

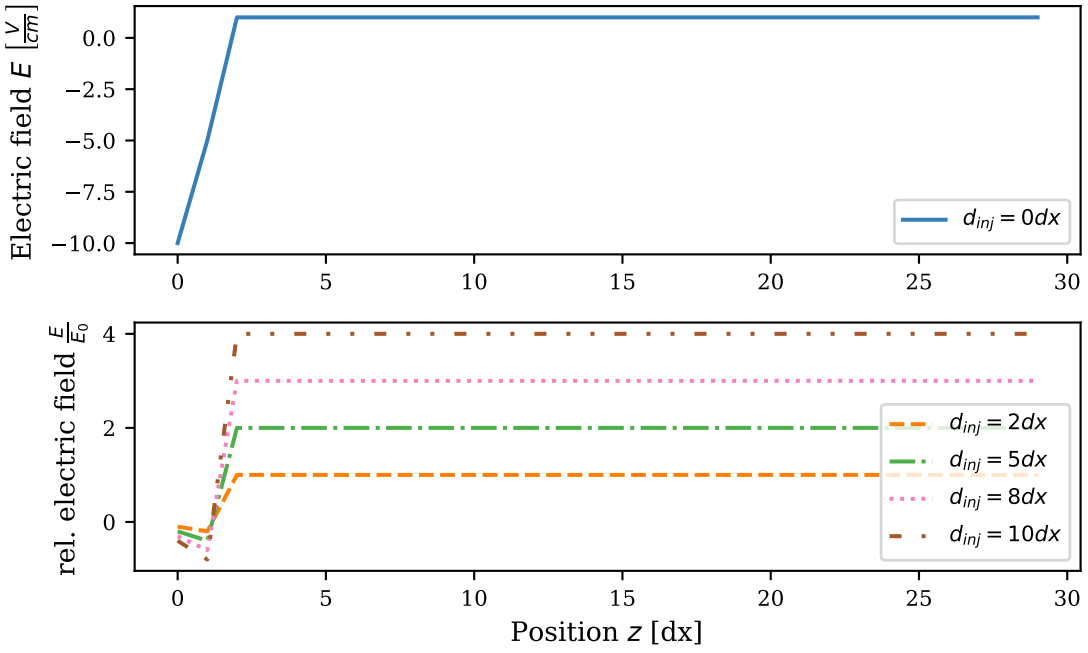

Figure 5.6.: PML far field

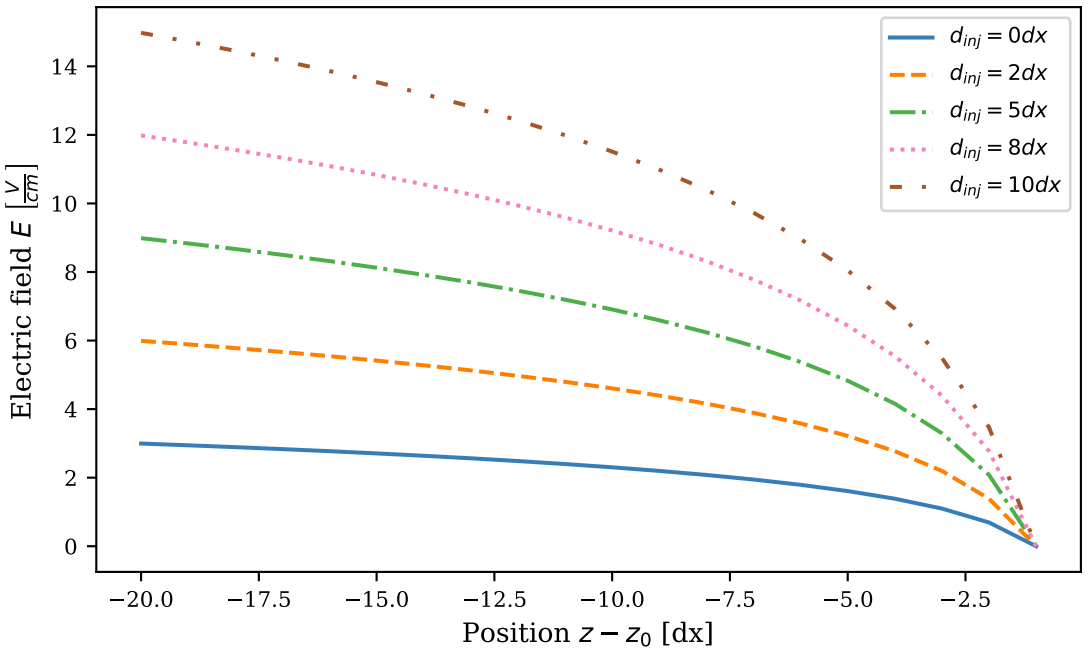

Figure 5.7.: PML far field

5.5. Electrostatic Potential from Poisson Equation

5.5.1. Finite Differences Method

5.6. Validation of ACRONYM Simulations

5.6.1. Ion Current Approximation

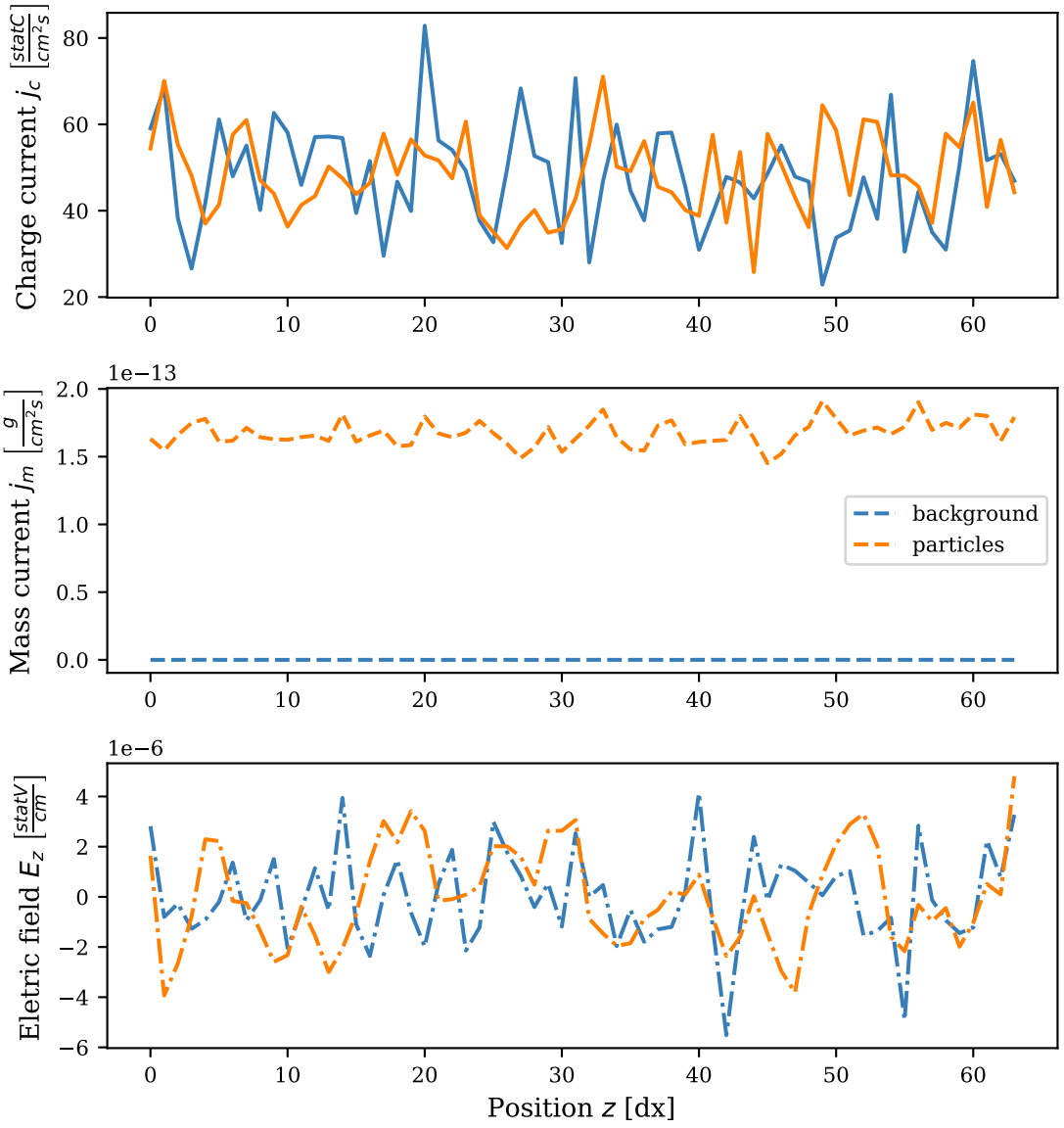

Figure 5.8.: Comparison of ion current

5.6.2. Background Electric Field

[Plot of current and electric field] **ToDo**

5.6.3. Cavity Mode Excitation

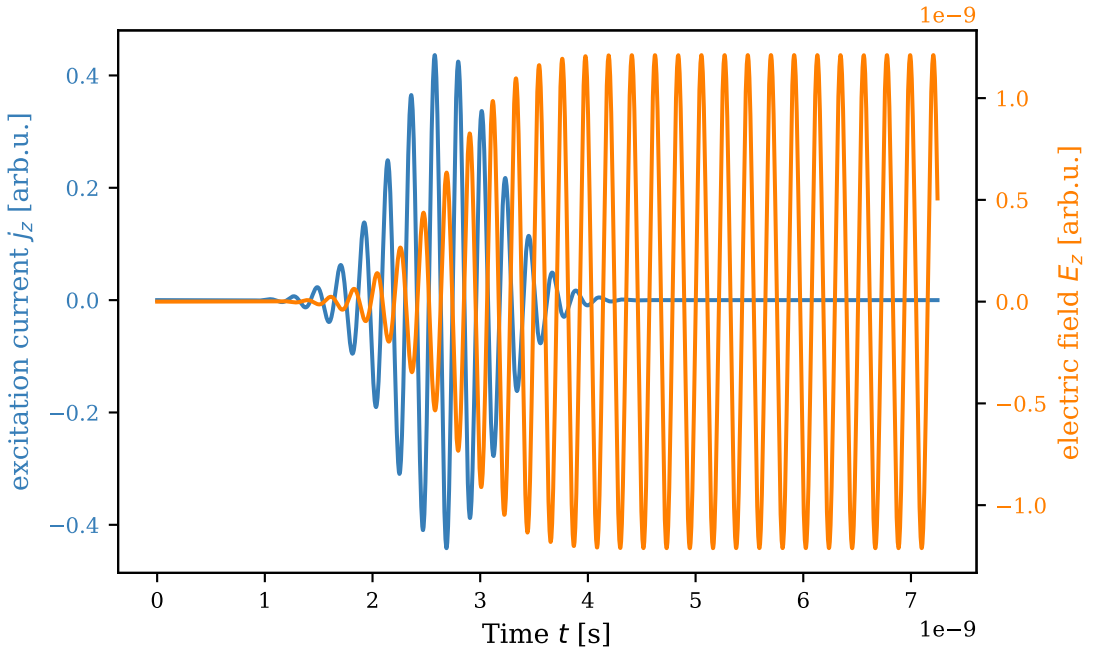

Figure 5.9.: Cavity mode excitation

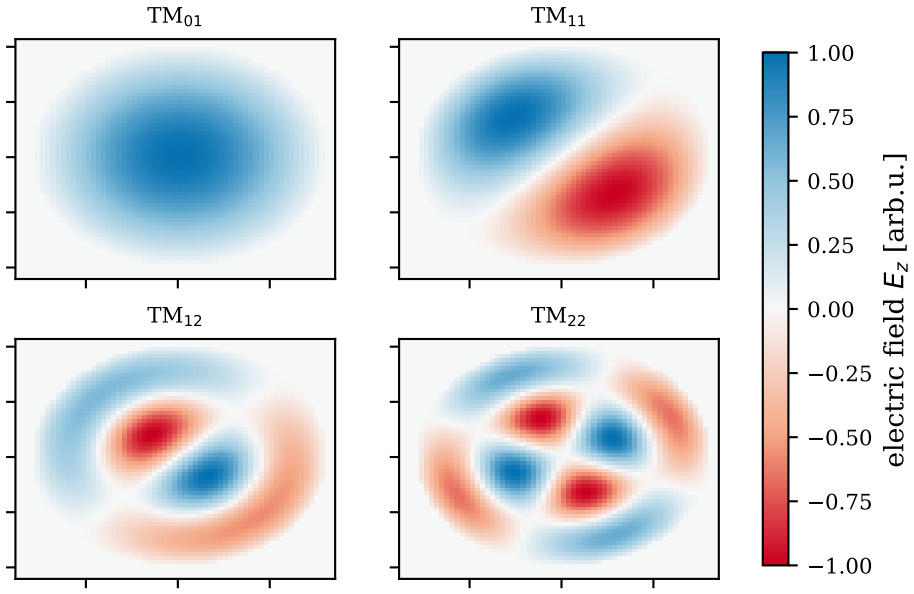

Figure 5.10.: TM mode pattern

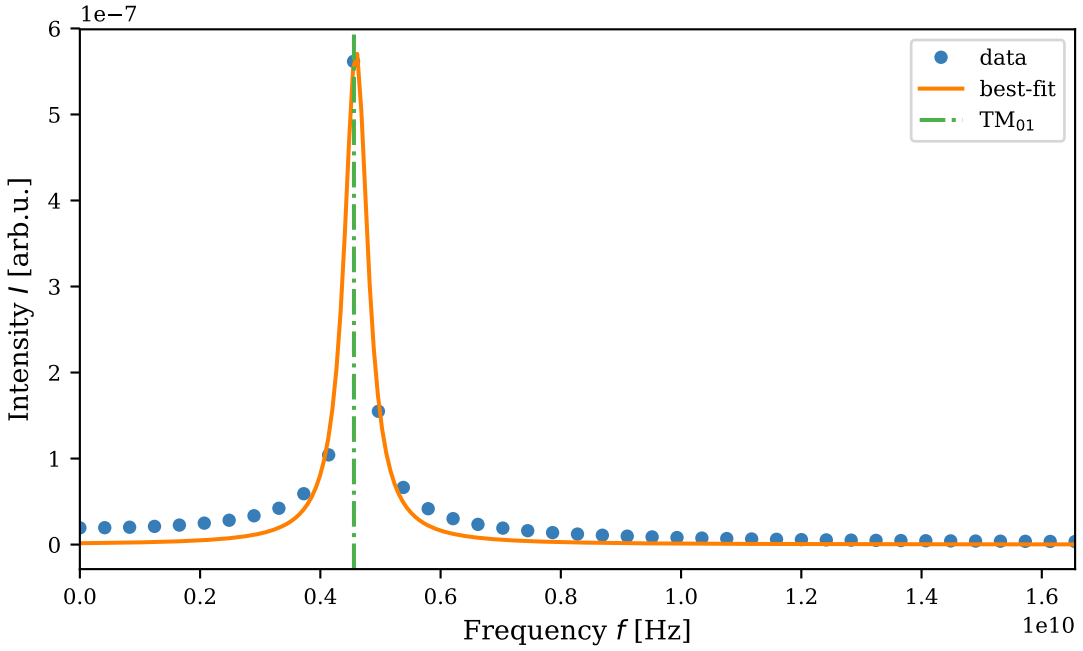

Figure 5.11.: Cavity mode fit

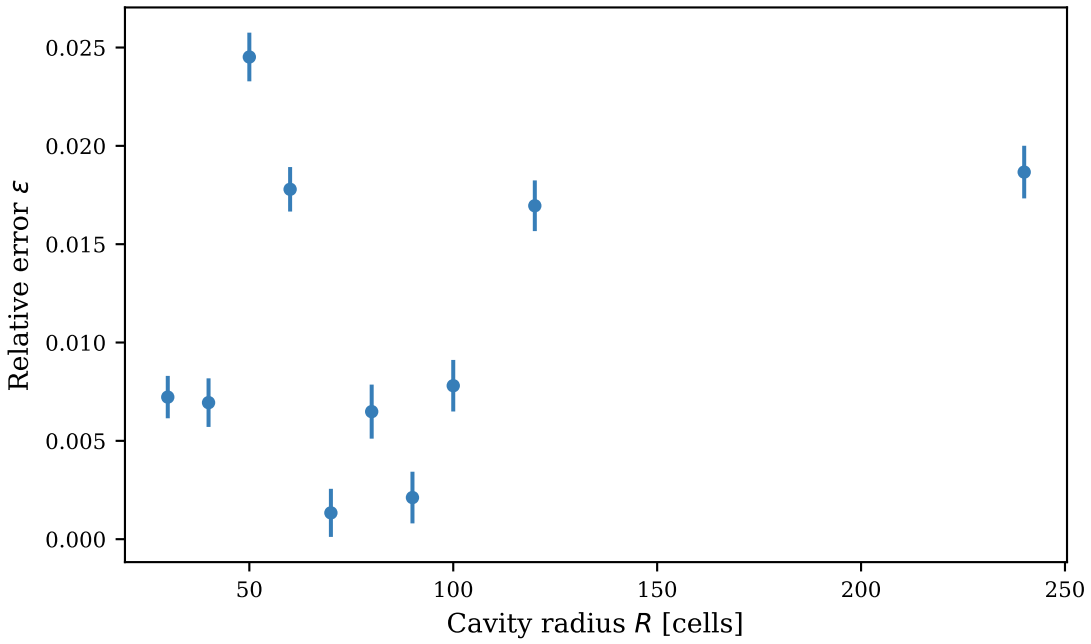

Figure 5.12.: Cavity mode excitation

5.6.4. Debye-Sheath Development

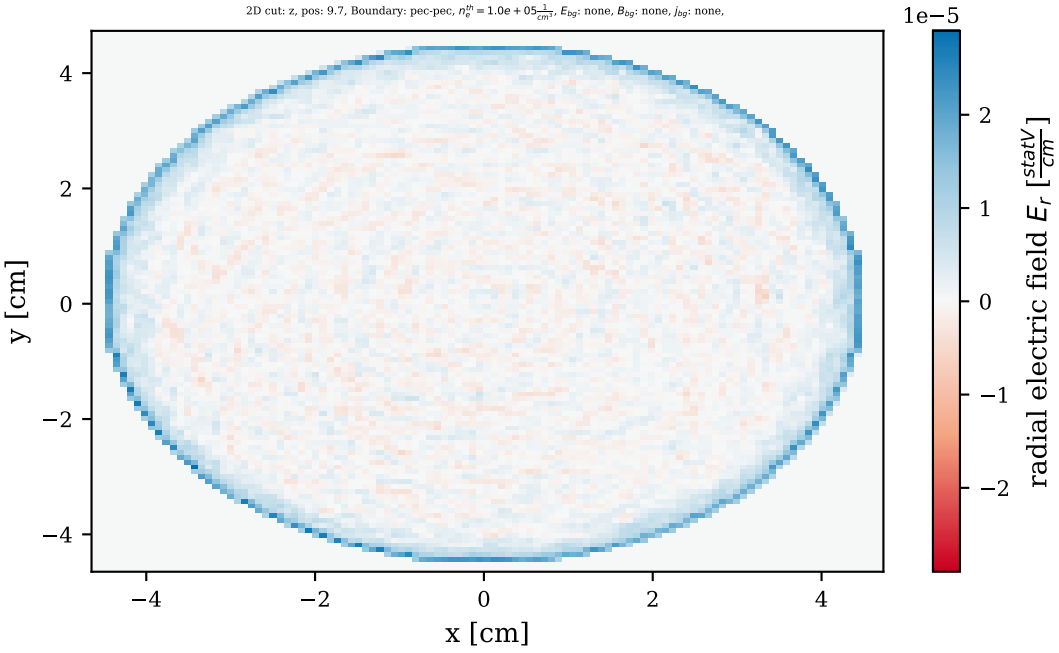

Figure 5.13.: Radial debye sheath

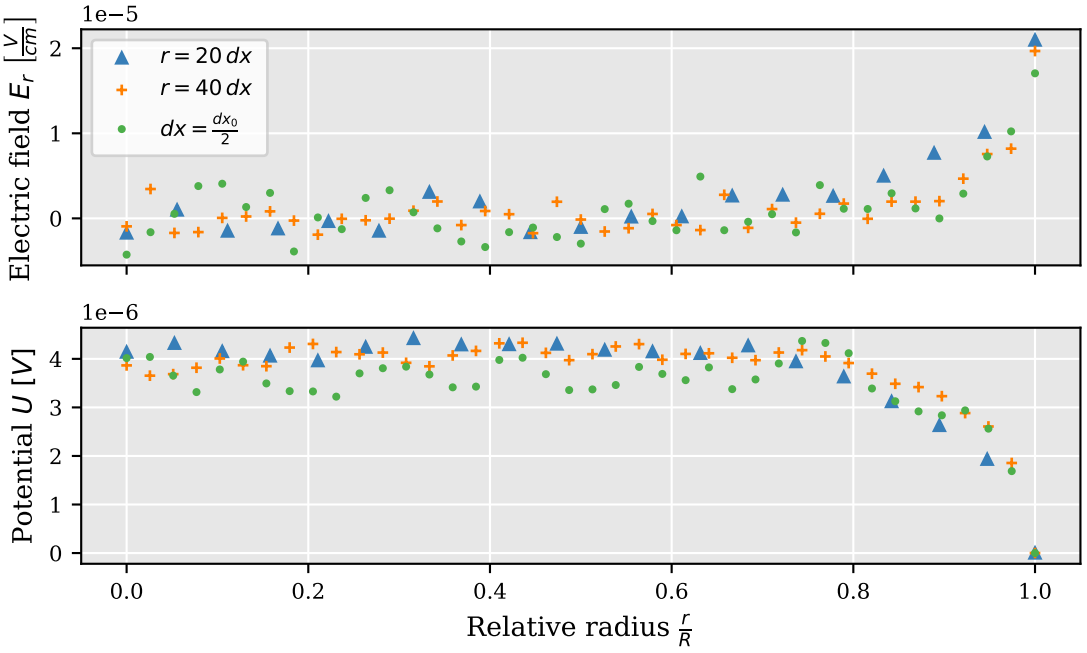

Figure 5.14.: Radial comparison

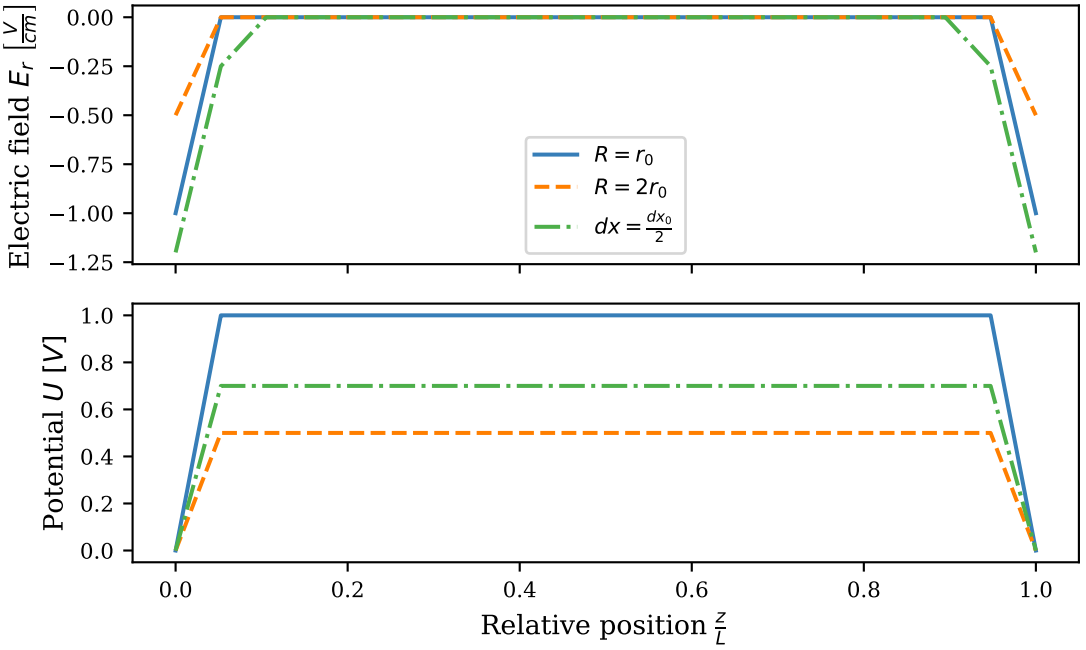

Figure 5.15.: Longitudinal comparison

5.7. Conclusion

Chapter 6
Particle in Cell Simulation of KATRIN Source

6.1. Rearwall Section

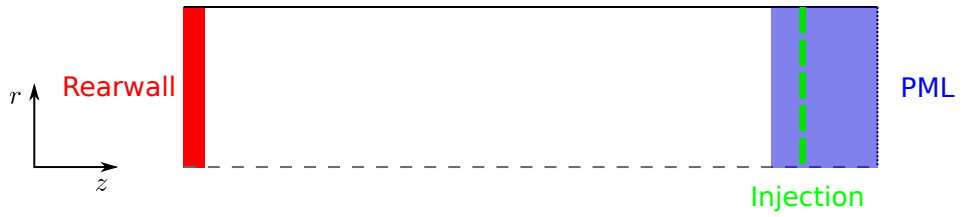

Figure 6.1.: Rear section sketch

6.1.1. Thermal electron distribution

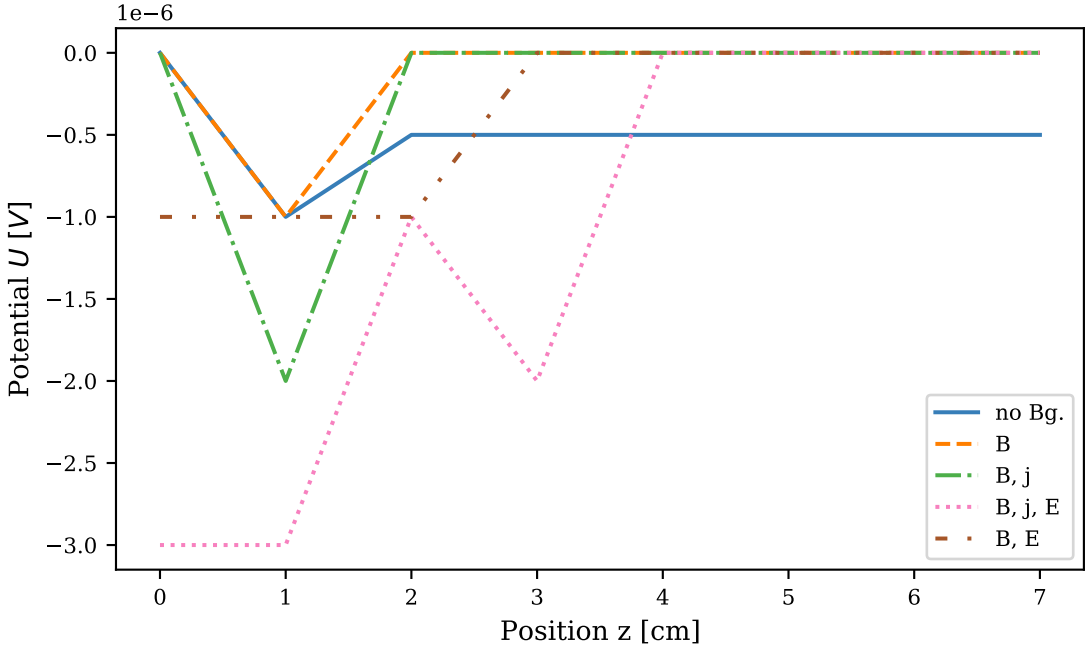

Figure 6.2.: Comparison of potential distributions

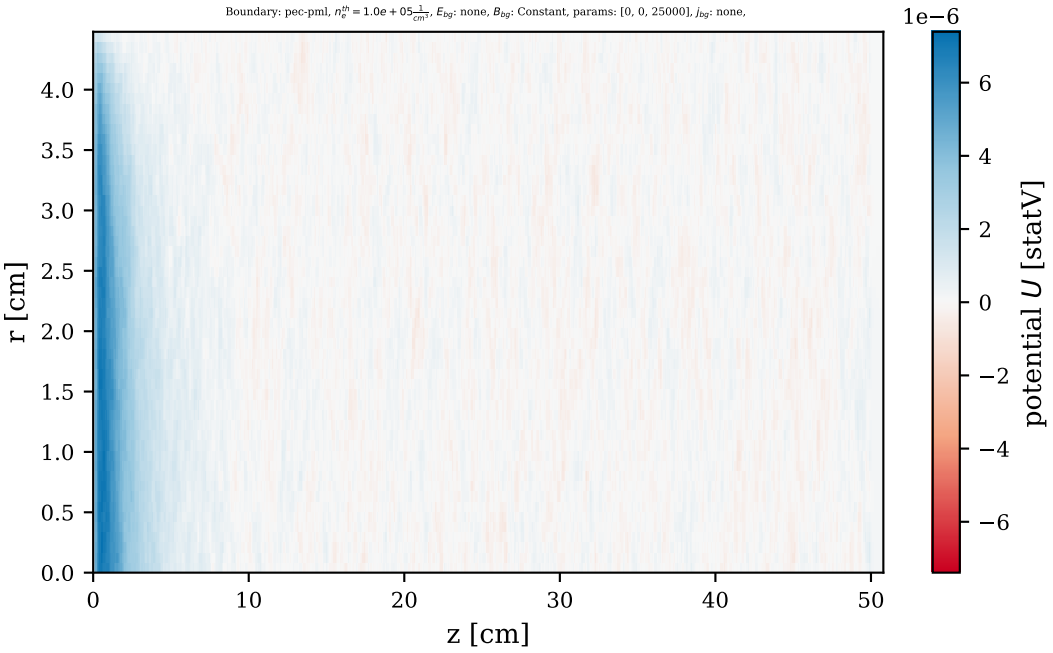

Figure 6.3.: Potential map

6.1.2. Thermal and Beta electron distribution

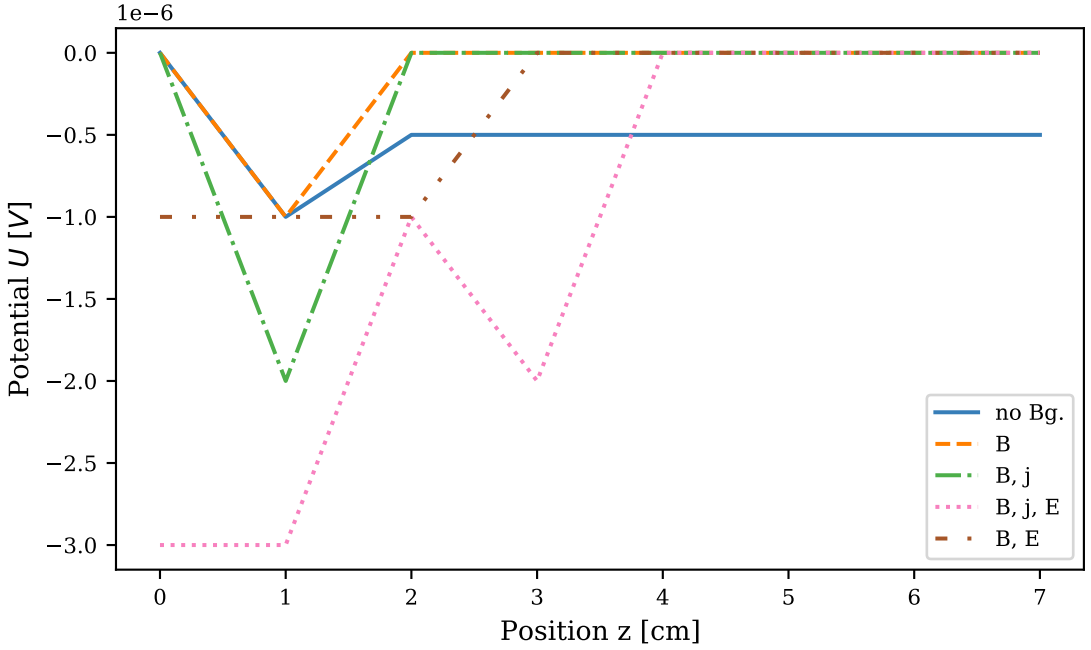

Figure 6.4.: Comparison of potential distributions

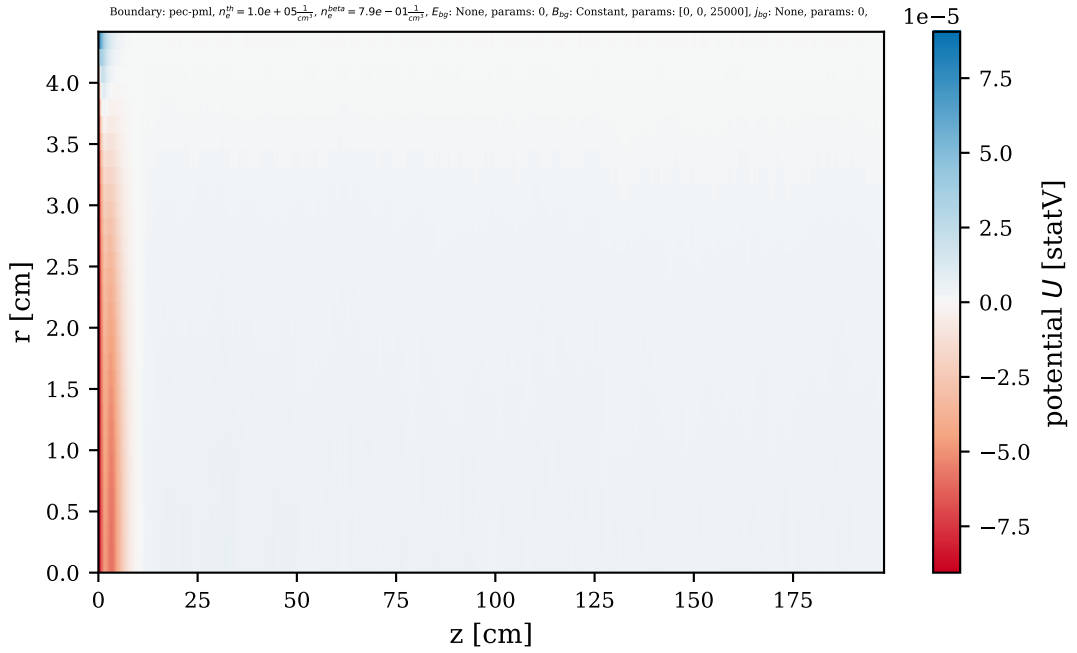

Figure 6.5.: Potential map

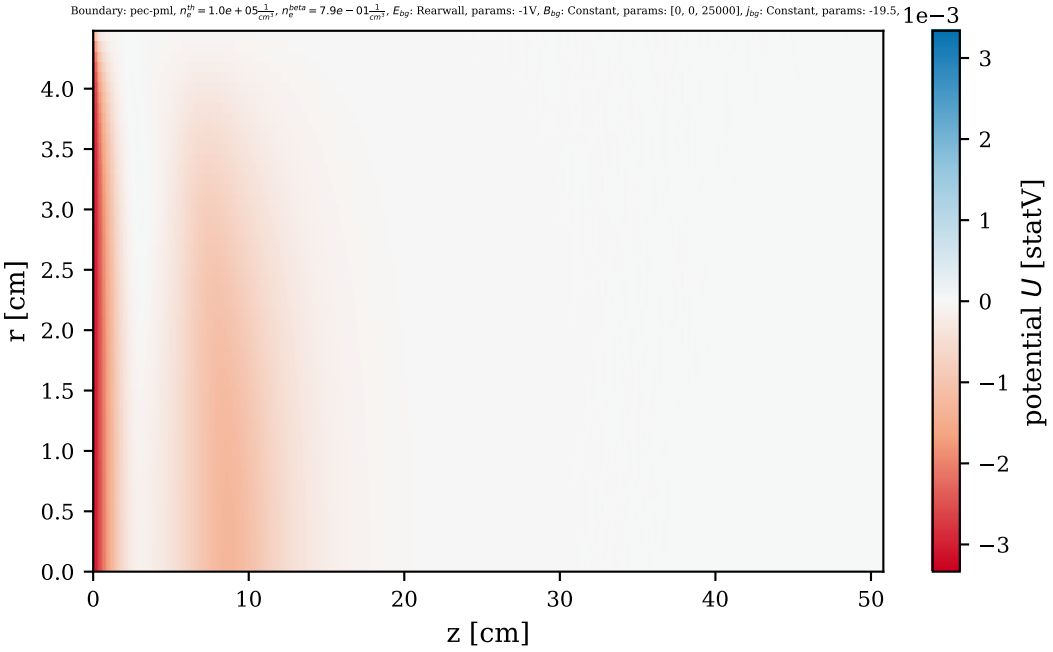

Figure 6.6.: Potential map with background field

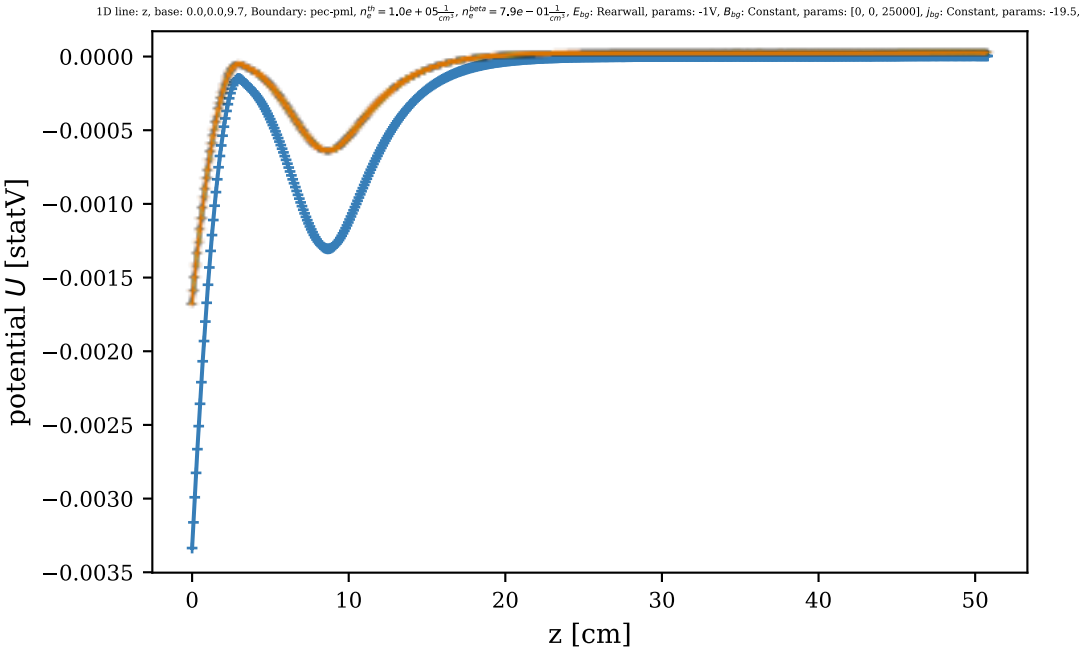

Figure 6.7.: Variation of rearwall potential

6.1.3. KATRIN Spectrum

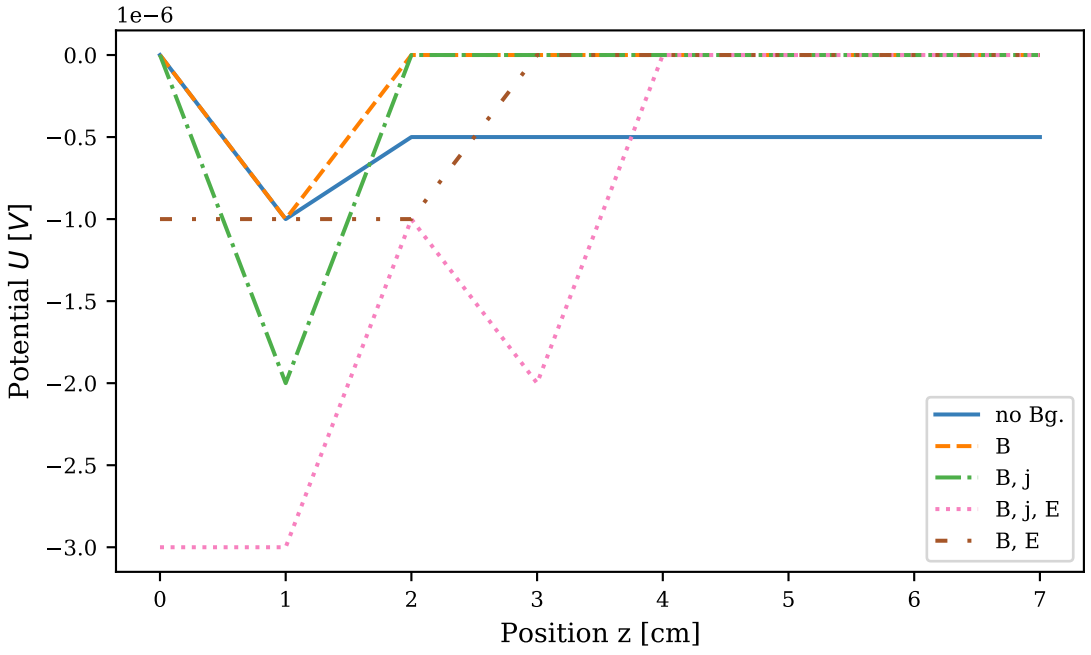

Figure 6.8.: Comparison of potential distributions

6.2. Central Section

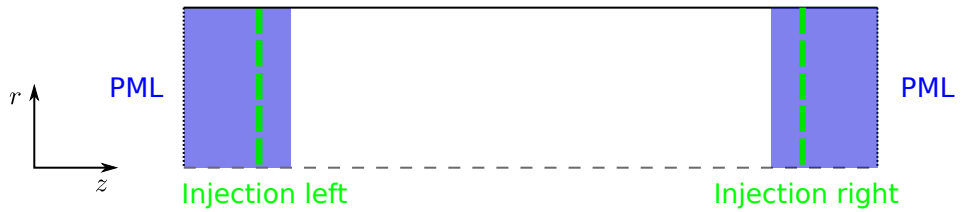

Figure 6.9.: Central section sketch

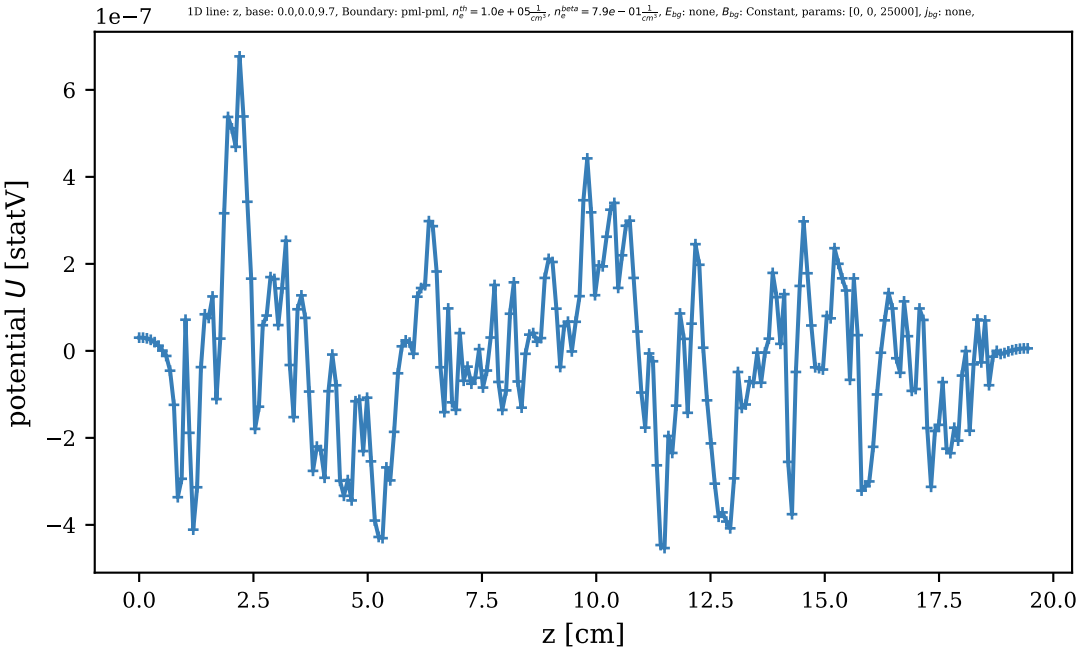

Figure 6.10.: Comparison of potential distributions

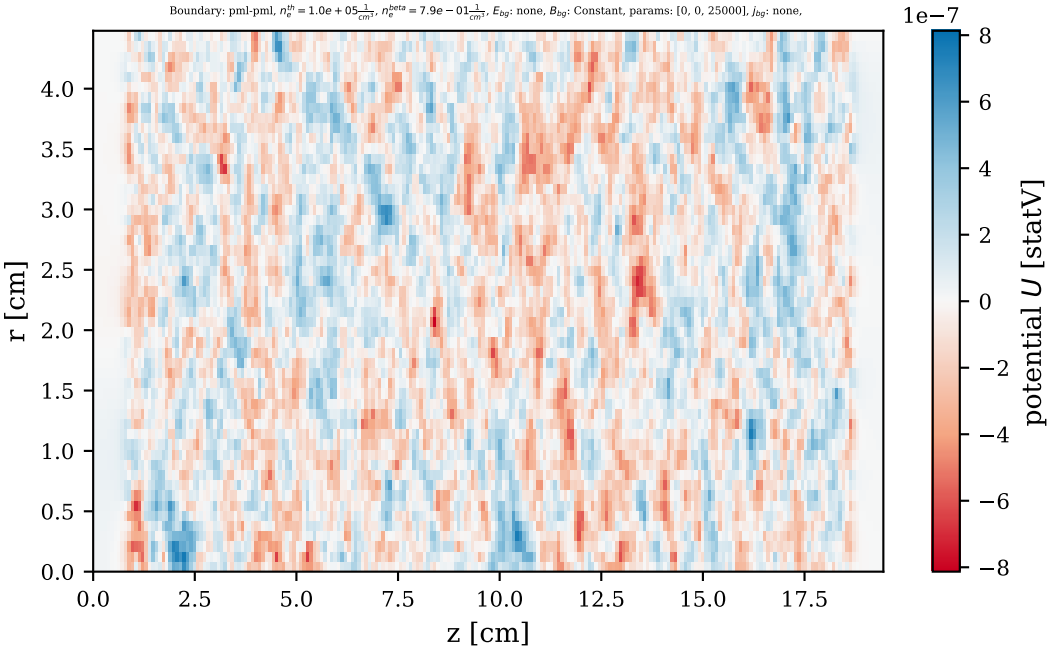

Figure 6.11.: Potential map

[Plot of potentials from different densities at left and right side] **ToDo**

6.3. Complete Source Section

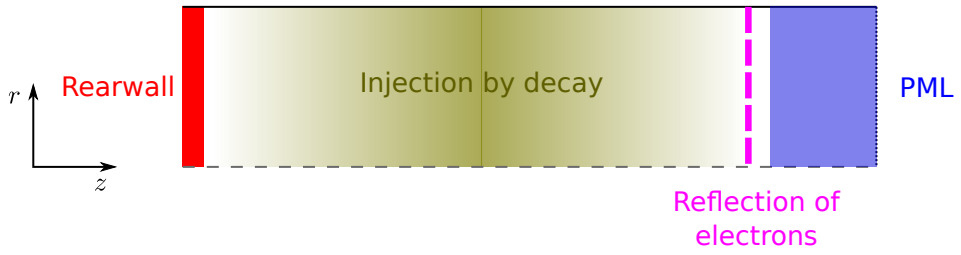

Figure 6.12.: Sketch of complete source section

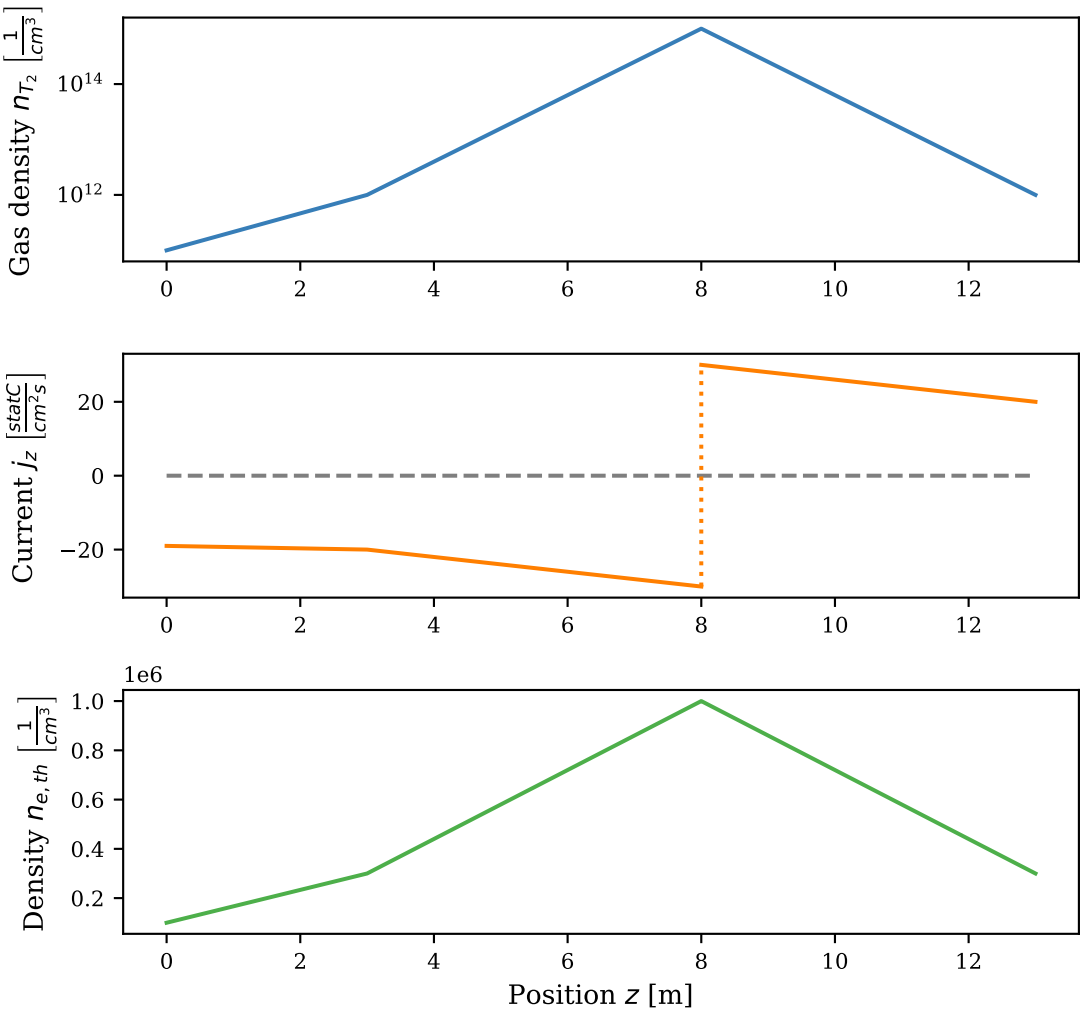

Figure 6.13.: Backgrounds

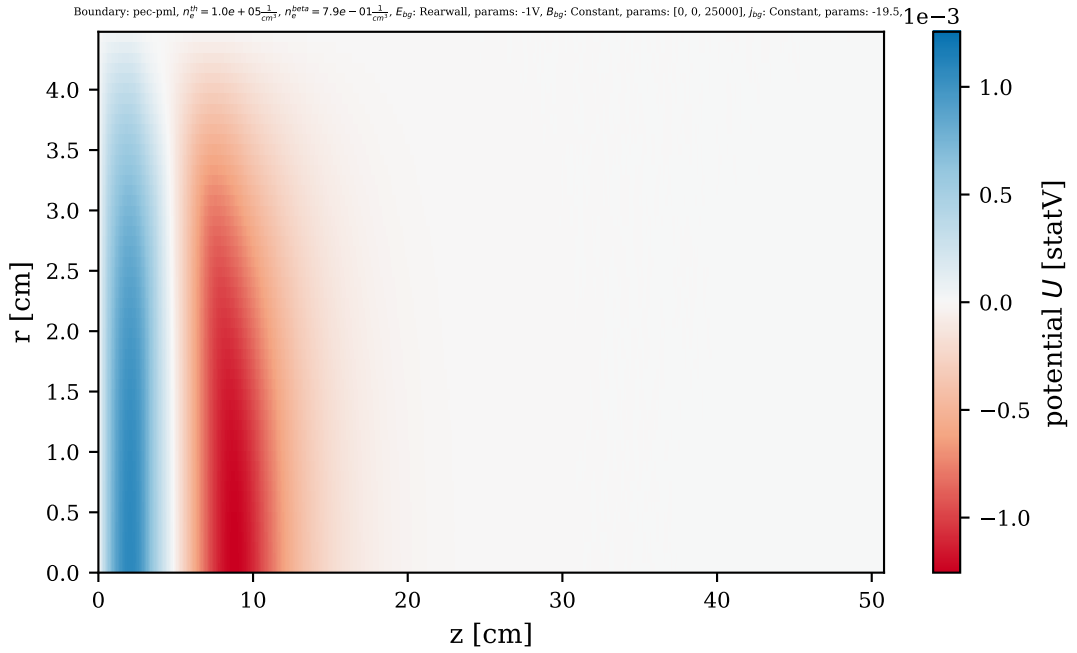

Figure 6.14.: Potential map

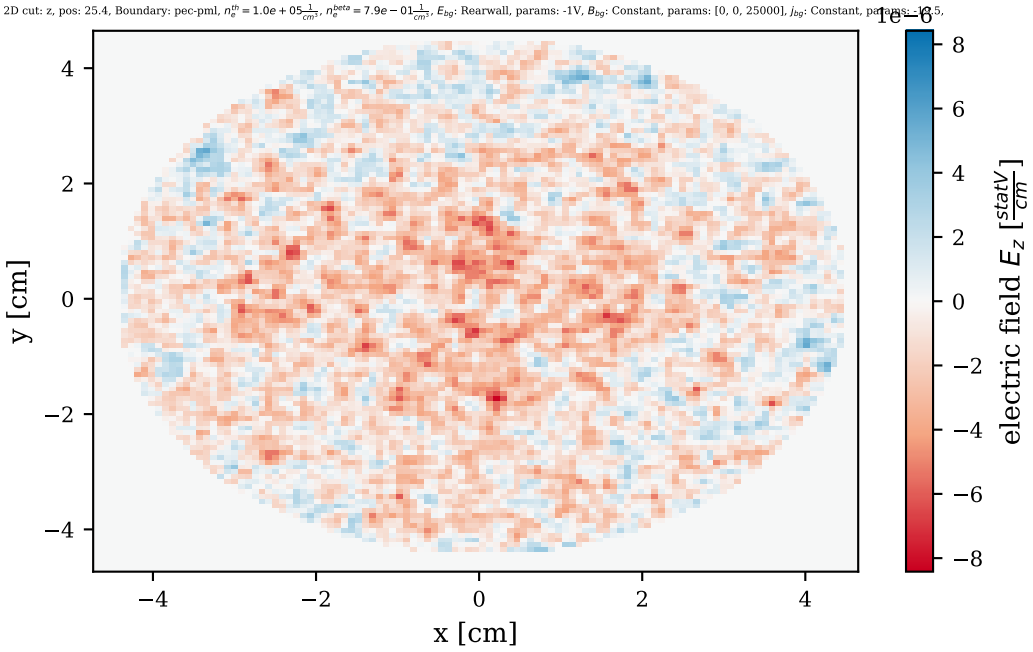

Figure 6.15.: Electric field in z direction

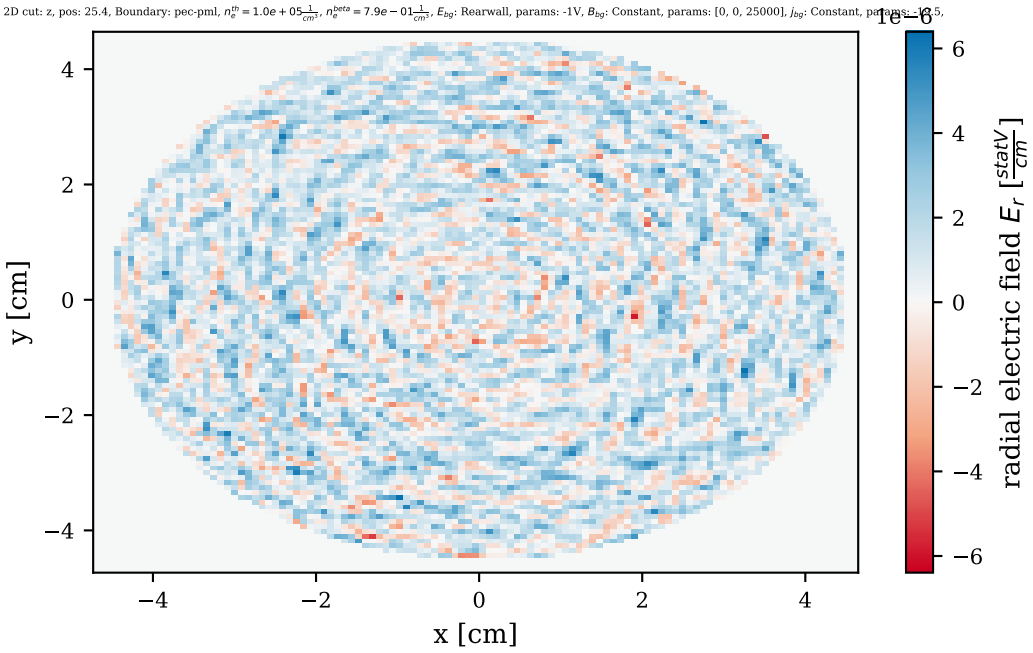

Figure 6.16.: Electric field in r direction

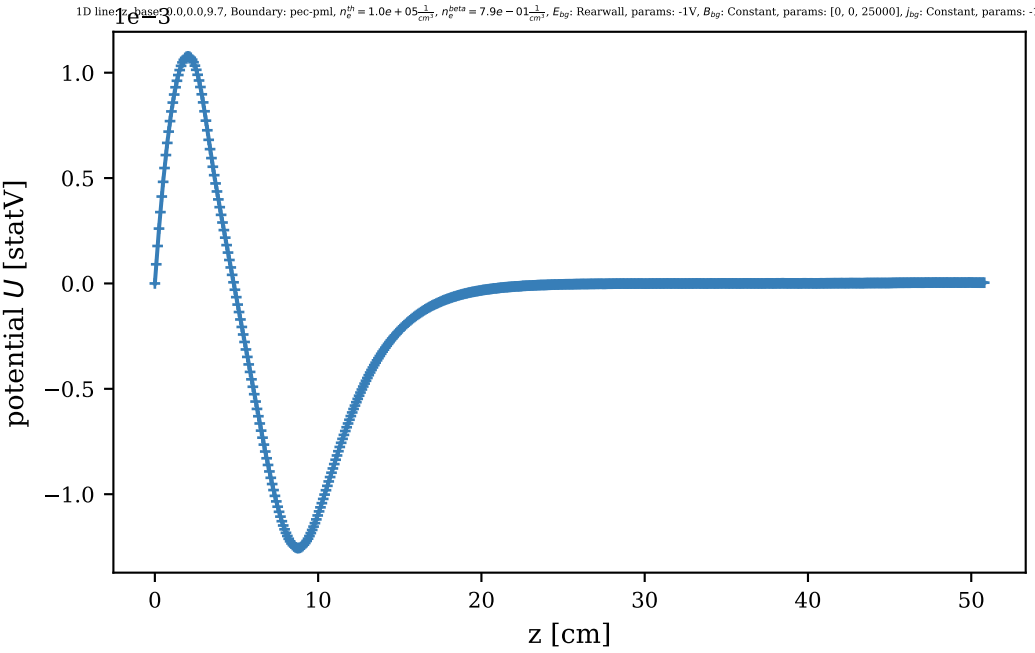

Figure 6.17.: Potential distribution in z direction

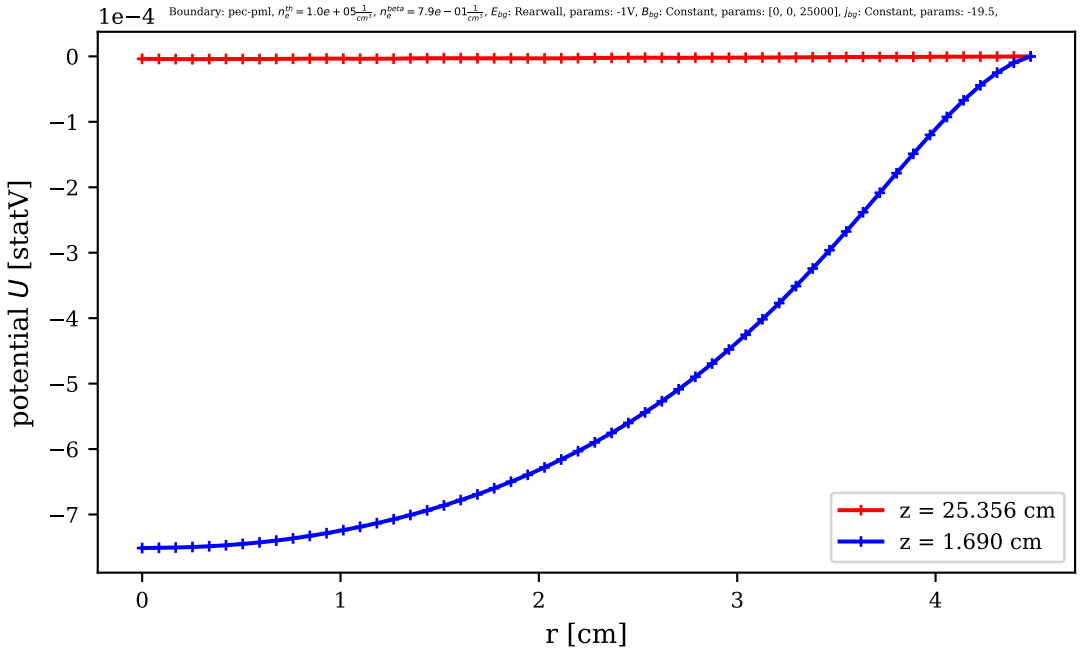

Figure 6.18.: Potential distribution in r direction

6.4. Conclusion

Appendix

A. First Appendix Section

Wonderful Appendix!

chapter 1, interactions: left out T-. Full plasma description needs this. They are generated by electron attachement, dissociatiove electron attachement, or beta decay. see janev

[Influence of electromagentic waves for Ebg. No investigation found so far] **ToDo**

Lorem ipsum dolor sit amet, consectetuer adipiscing elit. Ut purus elit, vestibulum ut, placerat ac, adipiscing vitae, felis. Curabitur dictum gravida mauris. Nam arcu libero, nonummy eget, consectetuer id, vulputate a, magna. Donec vehicula augue eu neque. Pellentesque habitant morbi tristique senectus et netus et malesuada fames ac turpis egestas. Mauris ut leo. Cras viverra metus rhoncus sem. Nulla et lectus vestibulum urna fringilla ultrices. Phasellus eu tellus sit amet tortor gravida placerat. Integer sapien est, iaculis in, pretium quis, viverra ac, nunc. Praesent eget sem vel leo ultrices bibendum. Aenean faucibus. Morbi dolor nulla, malesuada eu, pulvinar at, mollis ac, nulla. Curabitur auctor semper nulla. Donec varius orci eget risus. Duis nibh mi, congue eu, accumsan eleifend, sagittis quis, diam. Duis eget orci sit amet orci dignissim rutrum.

Nam dui ligula, fringilla a, euismod sodales, sollicitudin vel, wisi. Morbi auctor lorem non justo. Nam lacus libero, pretium at, lobortis vitae, ultricies et, tellus. Donec aliquet, tortor sed accumsan bibendum, erat ligula aliquet magna, vitae ornare odio metus a mi. Morbi ac orci et nisl hendrerit mollis. Suspendisse ut massa. Cras nec ante. Pellentesque a nulla. Cum sociis natoque penatibus et magnis dis parturient montes, nascetur ridiculus mus. Aliquam tincidunt urna. Nulla ullamcorper vestibulum turpis. Pellentesque cursus luctus mauris.

Nulla malesuada porttitor diam. Donec felis erat, congue non, volutpat at, tincidunt tristique, libero. Vivamus viverra fermentum felis. Donec nonummy pellentesque ante. Phasellus adipiscing semper elit. Proin fermentum massa ac quam. Sed diam turpis, molestie vitae, placerat a, molestie nec, leo. Maecenas lacinia. Nam ipsum ligula, eleifend at, accumsan nec, suscipit a, ipsum. Morbi blandit ligula feugiat magna. Nunc eleifend consequat lorem. Sed lacinia nulla vitae enim. Pellentesque tincidunt purus vel magna. Integer non enim. Praesent euismod nunc eu purus. Donec bibendum quam in tellus. Nullam cursus pulvinar lectus. Donec et mi. Nam vulputate metus eu enim. Vestibulum pellentesque felis eu massa.

Quisque ullamcorper placerat ipsum. Cras nibh. Morbi vel justo vitae lacus tincidunt ultrices. Lorem ipsum dolor sit amet, consectetuer adipiscing elit. In hac habitasse platea dictumst. Integer tempus convallis augue. Etiam facilisis. Nunc elementum fermentum wisi. Aenean placerat. Ut imperdiet, enim sed gravida sollicitudin, felis odio placerat quam, ac pulvinar elit purus eget enim. Nunc vitae tortor. Proin tempus nibh sit amet nisl. Vivamus quis tortor vitae risus porta vehicula.

Fusce mauris. Vestibulum luctus nibh at lectus. Sed bibendum, nulla a faucibus semper, leo velit ultricies tellus, ac venenatis arcu wisi vel nisl. Vestibulum diam. Aliquam pellentesque, augue quis sagittis posuere, turpis lacus congue quam, in hendrerit risus eros eget felis. Maecenas eget erat in sapien mattis porttitor. Vestibulum porttitor. Nulla facilisi. Sed a turpis eu lacus commodo facilisis. Morbi fringilla, wisi in dignissim interdum, justo lectus sagittis dui, et vehicula libero dui cursus dui. Mauris tempor ligula sed lacus. Duis cursus enim ut augue. Cras ac magna. Cras nulla. Nulla egestas. Curabitur a leo. Quisque egestas wisi eget nunc. Nam feugiat lacus vel est. Curabitur consectetuer.

Bibliography

[1] N. Aghanim et al. "Planck 2018 results". In: *Astronomy & Astrophysics* 641 (2020), A6. ISSN: 0004-6361. DOI: 10.1051/0004-6361/201833910.

[2] B. Aharmim et al. "Combined analysis of all three phases of solar neutrino data from the Sudbury Neutrino Observatory". In: *Physical Review C* 88 (2 2013), p. 025501. DOI: 10.1103/PhysRevC.88.025501.

[3] M. Aker et al. *Analysis methods for the first KATRIN neutrino-mass measurement*. URL: http://arxiv.org/pdf/2101.05253v2.

[4] M. Aker et al. "Improved Upper Limit on the Neutrino Mass from a Direct Kinematic Method by KATRIN". In: *Physical review letters* 123.22 (2019), p. 221802. DOI: 10.1103/PhysRevLett.123.221802.

[5] M. Aker et al. *The Design, Construction, and Commissioning of the KATRIN Experiment*. URL: http://arxiv.org/pdf/2103.04755v1.

[6] K. Altenmüller et al. "High-resolution spectroscopy of gaseous 83m Kr conversion electrons with the KATRIN experiment". In: *Journal of Physics G: Nuclear and Particle Physics* 47.6 (2020), p. 065002. ISSN: 0954-3899. DOI: 10.1088/1361-6471/ab8480.

[7] J.F. Amsbaugh et al. "Focal-plane detector system for the KATRIN experiment". In: *Nuclear Instruments and Methods in Physics Research Section A: Accelerators, Spectrometers, Detectors and Associated Equipment* 778 (2015), pp. 40–60. DOI: 10.1016/j.nima.2014.12.116.

[8] M. Arenz et al. "The KATRIN Superconducting Magnets: Overview and First Performance Results". In: *Journal of Instrumentation* 13.08 (2018), T08005. DOI: 10.1088/1748-0221/13/08/T08005. URL: http://iopscience.iop.org/1748-0221/13/08/T08005/.

[9] M. Arenz et al. "The KATRIN superconducting magnets: overview and first performance results". In: *Journal of Instrumentation* 13.08 (2018), T08005–T08005. DOI: 10.1088/1748-0221/13/08/T08005.

[10] V. N. Aseev et al. "Energy loss of 18 keV electrons in gaseous T_2 and quench condensed D_2 films". In: *The European Physical Journal D* 10 (1 2000), pp. 39–52. DOI: 10.1007/s100530050525.

[11] V. N. Aseev et al. "Upper limit on the electron antineutrino mass from the Troitsk experiment". In: *Physical Review D* 84 (11 2011), p. 112003. DOI: 10.1103/PhysRevD.84.112003.

[12] Martin Babutzka. "Design and development for the Rearsection of the KATRIN experiment". PhD thesis. Karlsruher Institut für Technologie (KIT), 2014. DOI: 10.5445/IR/1000045598. URL: http://nbn-resolving.org/urn:nbn:de:swb:90-455986.

[13] Ferdinand Cap. *Lehrbuch der Plasmaphysik und Magnetohydrodynamik*. Wien: Springer-Verlag, 1994. ISBN: 3211825703.

[14] Richard Dendy. *Plasma physics: An introductory course*. Repr. Cambridge: Cambridge Univ. Press, 1996. ISBN: 0521433096.

[15] M. Eugene Rudd. "User-friendly model for the energy distribution of electrons from proton or electron collisions". In: *International Journal of Radiation Applications and Instrumentation. Part D. Nuclear Tracks and Radiation Measurements* 16.2-3 (1989), pp. 213–218. ISSN: 13590189. DOI: 10.1016/1359-0189(89)90052-6.

[16] E. Fermi. "Versuch einer Theorie der ?-Strahlen. I". In: *Zeitschrift fr Physik* 88.3-4 (1934), pp. 161–177. ISSN: 1434-6001. DOI: 10.1007/BF01351864.

[17] Fabian Ruben Friedel. *Ion and plasma systematics during the first KATRIN neutrino mass measurements*. 2020. DOI: 10.5445/IR/1000126837.

[18] Alexander Fulst. "A Novel Quasi-Differential Method for MAC-E Filters and Determination and Control of the Electric Potentials of the KATRIN Experiment with a Stabilized Condensed Krypton Source and a UV Illumination System". PhD thesis. Westfälische Wilhelms-Universität Münster, 2020.

[19] Daniel Furse et al. "Kassiopeia: a modern, extensible C++ particle tracking package". In: *New Journal of Physics* 19.5 (2017), p. 053012. DOI: 10.1088/1367-2630/aa6950.

[20] Daniel Furse et al. "Kassiopeia: a modern, extensible C++ particle tracking package". In: *New Journal of Physics* 19.5 (2017), p. 053012. DOI: 10.1088/1367-2630/aa6950. URL: http://stacks.iop.org/1367-2630/19/i=5/a=053012.

[21] A. Gando et al. "Search for Majorana Neutrinos Near the Inverted Mass Hierarchy Region with KamLAND-Zen". In: *Physical review letters* 117.8 (2016), p. 082503. DOI: 10.1103/PhysRevLett.117.082503.

[22] L. Gastaldo et al. "The electron capture in 163Ho experiment – ECHo". In: *The European Physical Journal Special Topics* 226.8 (2017), pp. 1623–1694. ISSN: 1951-6355. DOI: 10.1140/epjst/e2017-70071-y.

[23] D. Gerlich. "Ion trap studies of ternary and radiative association processes". In: *Nuclear Physics Concepts in the Study of Atomic Cluster Physics*. Ed. by Rüdiger Schmidt, Hans O. Lutz, and Reiner Dreizler. Vol. 404. Lecture Notes in Physics. Berlin, Heidelberg: Springer Berlin Heidelberg, 1992, pp. 194–200. ISBN: 978-3-540-55625-1. DOI: 10.1007/3-540-55625-7{\textunderscore}21.

[24] B. Grosswendt and E. Waibel. "Transport of low energy electrons in nitrogen and air". In: *Nuclear Instruments and Methods* 155.1-2 (1978), pp. 145–156. ISSN: 0029554X. DOI: 10.1016/0029-554X(78)90198-2.

[25] Alireza Haghighat. *Monte Carlo Methods for Particle Transport*. 1st ed. Baton Rouge: Chapman and Hall/CRC, 2014. ISBN: 9781466592537.

[26] S. W. HARRISON. "Binding Energy and Geometry of the Hydrogen Clusters Hn+". In: *Nature <London> / Physical science. Physical science* 245.141 (), pp. 31–32. ISSN: 2058-1106. DOI: 10.1038/physci245031a0.

[27] Florian Heizmann. "Analysis tools and methods for tritium data taking with the KATRIN experiment". 51.03.01; LK 01. PhD thesis. Karlsruher Institut für Technologie (KIT), 2018. DOI: 10.5445/IR/1000093536. URL: https://publikationen.bibliothek.kit.edu/1000093536.

[28] Rudolf Herrmann and Uwe Preppernau. *Elektronen im Kristall*. Vienna: Springer Vienna, 1979. ISBN: 978-3-7091-8521-6. DOI: 10.1007/978-3-7091-8520-9.

[29] Ratko K. Janev, Detlev Reiter, and Ulrich Samm. *Collision processes in low-temperature hydrogen plasmas*. Jülich, 2003. URL: http://hdl.handle.net/2128/249.

[30] KATRIN collaboration. *KATRIN Design Report*. FZKA scientific report 7090. 2005. URL: http://bibliothek.fzk.de/zb/berichte/FZKA7090.pdf.

[31] R. Kersevan and J.-L. Pons. "Introduction to MOLFLOW+ : New graphical processing unit-based Monte Carlo code for simulating molecular flows and for calculating angular coefficients in the compute unified device architecture environment". In: *Journal of Vacuum Science & Technology A: Vacuum, Surfaces, and Films* 27.4 (2009), pp. 1017–1023. ISSN: 0734-2101. DOI: 10.1116/1.3153280.

[32] Patrick Kilian, Thomas Burkart, and Felix Spanier. "The Influence of the Mass Ratio on Particle Acceleration by the Filamentation Instability". In: *High Performance Computing in Science and Engineering '11*. Ed. by Wolfgang E. Nagel, Dietmar B. Kröner, and Michael M. Resch. Berlin, Heidelberg: Springer Berlin Heidelberg, 2012, pp. 5–13. ISBN: 978-3-642-23868-0. DOI: 10.1007/978-3-642-23869-7{\textunderscore}1.

[33] Kim and Rudd. "Binary-encounter-dipole model for electron-impact ionization". In: *Physical review. A, Atomic, molecular, and optical physics* 50.5 (1994), pp. 3954–3967. ISSN: 1050-2947. DOI: 10.1103/physreva.50.3954.

[34] Igor A. Kotelnikov and Alexander I. Milstein. "Electron radiative recombination with a hydrogen-like ion". In: *Physica Scripta* 94.5 (2019), p. 055403. ISSN: 0031-8949. DOI: 10.1088/1402-4896/ab060a.

[35] C. Kraus et al. "Final results from phase II of the Mainz neutrino mass search in tritium β decay". In: *The European Physical Journal C* 40.4 (2005), pp. 447–468. DOI: 10.1140/epjc/s2005-02139-7.

[36] L. Kuckert et al. "Modelling of gas dynamical properties of the KATRIN tritium source and implications for the neutrino mass measurement". In: *Vacuum* 158 (2018), pp. 195–205. DOI: 10.1016/j.vacuum.2018.09.036. URL: https://www.sciencedirect.com/science/article/pii/S0042207X18310972.

[37] Laura Kuckert. "The Windowless Gaseous Tritium Source of the KATRIN Experiment – Characterisation of Gas Dynamical and Plasma Properties". PhD thesis. Karlsruher Institut für Technologie (KIT), 2016. DOI: 10.5445/IR/1000065077. URL: http://nbn-resolving.org/urn:nbn:de:swb:90-650776.

[38] Laura Kuckert et al. "Modelling of gas dynamical properties of the Katrin tritium source and implications for the neutrino mass measurement". In: *Vacuum* 158 (2018), pp. 195–205. ISSN: 0042207X. DOI: 10.1016/j.vacuum.2018.09.036.

[39] Rita G. Lerner and George Lockwood Trigg. *Encyclopedia of physics*. 2nd ed. New York: VCH, 1991. ISBN: 0895737523.

[40] Thomas J. Loredo and Donald Q. Lamb. "Bayesian analysis of neutrinos observed from supernova SN 1987A". In: *Physical Review D* 65.6 (2002). ISSN: 1550-7998. DOI: 10.1103/PhysRevD.65.063002.

[41] L. L. Lucas and M. P. Unterweger. "Comprehensive Review and Critical Evaluation of the Half-Life of Tritium". In: *Journal of research of the National Institute of Standards and Technology* 105.4 (2000), pp. 541–549. ISSN: 1044-677X. DOI: 10.6028/jres.105.043.

[42] Moritz Benedikt Machatschek. "A Phenemological Theory of KATRIN Source Potential Systematics and its Application in Krypton-83m Calibration Measurements". PhD thesis. Karlsruher Institut für Technologie (KIT), 2021.

[43] Masayuki Nakahata. "Super-Kamiokande". In: *Nuclear Physics B - Proceedings Supplements* 87.1-3 (2000), pp. 125–134. ISSN: 09205632. DOI: 10.1016/S0920-5632(00)00652-6.

[44] Raphael Ostertag. "Investigation of Plasma Effetcs in the KATRIN Source with 83m Kr". Master thesis. Karlsruher Institut für Technologie (KIT), 2020. URL: https://www.katrin.kit.edu/publikationen/mth_ostertag.pdf.

[45] E. W. Otten and C. Weinheimer. "Neutrino mass limit from tritium β decay". In: *Reports on Progress in Physics* 71.8 (2008), p. 086201. DOI: 10.1088/0034-4885/71/8/086201.

[46] W. Paul et al. "On the dynamics of the reaction of positive hydrogen cluster ions (H5+ to H23+) with para and normal hydrogen at 10 K". In: *International Journal of Mass Spectrometry and Ion Processes* 149-150 (1995), pp. 373–387. ISSN: 01681176. DOI: 10.1016/0168-1176(95)04269-Q.

[47] Dietmar Petrascheck and Franz Schwabl. *Elektrodynamik*. Berlin, Heidelberg: Springer Berlin Heidelberg, 2019. ISBN: 978-3-662-59786-6. DOI: 10.1007/978-3-662-59787-3.

[48] J.B.C. Pettersson et al. "Dissociative recombination and excitation of D 5+ by collisions with low-energy electrons". In: *Molecular Physics* 113.15-16 (2015), pp. 2099–2104. ISSN: 0026-8976. DOI: 10.1080/00268976.2014.1003985.

[49] A. V. Phelps. "Collisions of H+, H2+, H3+, ArH+, H−, H, and H2 with Ar and of Ar+ and ArH+ with H2 for Energies from 0.1 eV to 10 keV". In: *Journal of Physical and Chemical Reference Data* 21.4 (1992), pp. 883–897. ISSN: 0047-2689. DOI: 10.1063/1.555917.

[50] Radek Plasil et al. "Stabilization of H+-H2 collision complexes between 11 and 28 K". In: *Philosophical transactions. Series A, Mathematical, physical, and engineering sciences* 370.1978 (2012), pp. 5066–5073. ISSN: 1364-503X. DOI: 10.1098/rsta.2012.0098.

[51] Eugen Raspopin. "Prilimiray title". Master thesis. Karlsruher Institut für Technologie (KIT), 2021. URL: https://www.katrin.kit.edu/publikationen/mth_ostertag.pdf.

[52] Christina Reiling. "A new Monte Carlo model of the detailed electron and ion distribution in the WGTS of KATRIN". Master thesis. Karlsruher Institut für Technologie (KIT), 2019.

[53] Francesc Salvat, Aleksander Jablonski, and Cedric J. Powell. "elsepa—Dirac partial-wave calculation of elastic scattering of electrons and positrons by atoms, positive ions and molecules". In: *Computer Physics Communications* 165.2 (2005), pp. 157–190. ISSN: 00104655. DOI: 10.1016/j.cpc.2004.09.006.

[54] Ulrich Stroth. *Plasmaphysik*. Wiesbaden: Vieweg+Teubner, 2011. ISBN: 978-3-8348-1615-3. DOI: 10.1007/978-3-8348-8326-1.

[55] TATSUO TABATA and TOSHIZO SHIRAI. "ANALYTIC CROSS SECTIONS FOR COLLISIONS OF H+, H2+, H3+, H, H2, AND H− WITH HYDROGEN MOLECULES". In: *Atomic Data and Nuclear Data Tables* 76.1 (2000), pp. 1–25. ISSN: 0092640X. DOI: 10.1006/adnd.2000.0835.

[56] H. Tawara et al. "Cross Sections and Related Data for Electron Collisions with Hydrogen Molecules and Molecular Ions". In: *Journal of Physical and Chemical Reference Data* 19.3 (1990), pp. 617–636. ISSN: 0047-2689. DOI: 10.1063/1.555856.

[57] S. Trasatti and R. Parsons. "Interphases in systems of conducting phases (Provisional)". In: *Pure and Applied Chemistry* 55.8 (1983), pp. 1251–1268. ISSN: 0033-4545. DOI: 10.1351/pac198355081251.

[58] Nancy Wandkowsky. "Study of background and transmission properties of the KATRIN spectrometers". PhD thesis. Karlsruher Institut für Technologie (KIT), 2013. DOI: 10.5445/IR/1000036631. URL: http://nbn-resolving.org/urn:nbn:de:swb:90-366316.

[59] Jung-Sik Yoon et al. "Cross Sections for Electron Collisions with Hydrogen Molecules". In: *Journal of Physical and Chemical Reference Data* 37.2 (2008), pp. 913–931. ISSN: 0047-2689. DOI: 10.1063/1.2838023.

List of Figures

2.1. Tritium beta decay spectrum. 5
2.2. KATRIN beam line and its components. 6
2.3. Windowless Gaseous Tritium Source 7
2.4. Injection Chamber 8
2.5. Differential Pumping Section. 9
2.6. Cryogenic Pumping Section. 10
2.7. MAC-E filter principle. 11
2.8. Rear wall chamber. 13
2.9. Neutral gas density. 14
2.10. Source tempererature. 16
2.11. Bulk velocity 17
2.12. Simulated bulk velocity in rear direction. 18
2.13. Simplified geometry of the KATRIN source 20
2.14. Analytical electric background field of the rear wall chamber 22
2.15. Magnetic background field 23
2.16. Selection of Electron-H_2 cross sections 25
2.17. Dissocitative recombination and dissocitatve excitation cross sections 28
2.18. Selection of H^+-H_2 cross sections 30
2.19. Selection of ${H_2}^+$-H_2 cross sections 33
2.20. Selection of ${H_3}^+$-H_2 cross sections 35
2.21. Ion cluster creation and fragmentation at 10 K 37
2.22. Comparison of measurement and scaling 38
2.23. Clustering at 80 K 40
2.24. Line width 42
2.25. Measured electric currents leaving the source 44
2.26. Pro Katrin Measurement 45

3.1. Debye Shielding 49
3.2. Classical diffusion. 53
3.3. Characteristic length scales. 55
3.4. Characteristic time scales. 59
3.5. Potential map of Drift-Diffusion Model 62
3.6. Simulation strategy 63

4.1. KARL Simulation procedure. 66
4.2. Guiding center change 70
4.3. Density distribution 73
4.4. current distribution 74
4.5. Energy density distribution 75
4.6. Density in z 75

5.1. PIC scheme 77

5.2. Yee lattice . . . 78
5.3. Boris push . . . 79
5.4. Current deposition . . . 80
5.5. Maxwell solver . . . 81
5.6. PML far field . . . 82
5.7. PML far field . . . 83
5.8. Comparison of ion current . . . 84
5.9. Cavity mode excitation . . . 86
5.10. TM mode pattern . . . 87
5.11. Cavity mode fit . . . 88
5.12. Cavity mode excitation . . . 89
5.13. Radial debye sheath . . . 90
5.14. Radial comparison . . . 91
5.15. Longitudinal comparison . . . 92

6.1. Rear section sketch . . . 95
6.2. Comparison of potential distributions . . . 96
6.3. Potential map . . . 97
6.4. Comparison of potential distributions . . . 98
6.5. Potential map . . . 99
6.6. Potential map with background field . . . 100
6.7. Variation of rearwall potential . . . 101
6.8. Comparison of potential distributions . . . 102
6.9. Central section sketch . . . 103
6.10. Comparison of potential distributions . . . 104
6.11. Potential map . . . 105
6.12. Sketch of complete source section . . . 106
6.13. Backgrounds . . . 107
6.14. Potential map . . . 108
6.15. Electric field in z direction . . . 109
6.16. Electric field in r direction . . . 110
6.17. Potential distribution in z direction . . . 111
6.18. Potential distribution in r direction . . . 112

List of Tables

2.1. Methods of neutrino mass measurements. 4
2.2. Binding energies and fragmentation rates. 39

3.1. Mean free path. 51

List of Abbreviations

STS Source and Transport Section

SDS Spectrometer and Detector Section

WGTS Windowless Gaeous Tritium Source

DPS Differential Pumping Section

CPS Cryogenic Pumping Section

MS Main Spectrometer

PS Pre-Spectrometer

RS Rear Section

egun Electron Gun

BIXS Beta-Induced X-ray Spectroscopy

KATRIN KArlsruhe TRItium Neutrino

MOLFLOW+ Molflow plus

ELSEPA Dirac partial-wave calculation of elastic scattering of electrons and positrons by atoms, positive ions and molecules

PRO KATRIN Plasma Rear wall Optimization at KATRIN

COMSOL Comsol

ACRONYM Another Code for pushing Relativistic Objects, Now with Yee lattice and Macro particles

KARL KAtrin WGTS electon and ion spectrum monte CaRLo

FBM Forward Beam Monitor

MAC-E magnetic adiabatic collimation with electrostatic retardation

kassiopeia KASSIOPEIA

kemfield KEMfield